AFRL-HE-BR-TR-2003-0119

UNITED STATES AIR FORCE RESEARCH LABORATORY

LASER RANGE SAFETY TOOL (LRST)

BRDF REFERENCE

Gregg Crockett

Logicon-RDA
2600 Yale Blvd SE
Albuquerque, NM 87106

Boeing-SVS
4411 The 25 Way NE Ste 350
Albuquerque, NM 87109

**HUMAN EFFECTIVENESS DIRECTORATE
DIRECTED ENERGY BIOEFFECTS DIVISION
OPTICAL RADIATION BRANCH
2650 LOUIS BAUER DRIVE
Brooks City-Base, TX 78235**
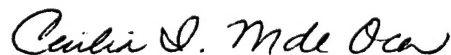
September 2003

20031017 157

NOTICES

This report is published in the interest of scientific and technical information exchange and does not constitute approval or disapproval of its ideas or findings.

This report is published as received and has not been edited by the publication staff of the Air Force Research Laboratory.

Using Government drawings, specifications, or other data included in this document for any purpose other than Government-related procurement does not in any way obligate the US Government. The fact that the Government formulated or supplied the drawings, specifications, or other data, does not license the holder or any other person or corporation, or convey any rights or permission to manufacture, use, or sell any patented invention that may relate to them.

The Office of Public Affairs has reviewed this paper, and it is releasable to the National Technical Information Service, where it will be available to the general public, including foreign nationals.

This report has been reviewed and is approved for publication.

Cecilia S. Mde Oca

CECILIA MONTES DE OCA, Capt, USAF
Contract Monitor

Miller

RICHARD L. MILLER, Ph.D.
Chief, Directed Energy Bioeffects Division

REPORT DOCUMENTATION PAGE

1. REPORT DATE (DD-MM-YYYY) 14-05-2003	**2. REPORT TYPE** Technical Report	**3. DATES COVERED** (From - To) 1998-2001

4. TITLE AND SUBTITLE

Laser Range Safety Tool (LRST), BRDF Reference Manual

5a. CONTRACT NUMBER
F04701-98D-100, CDRL A004

5b. GRANT NUMBER

5c. PROGRAM ELEMENT NUMBER

6. AUTHOR(S)
Gregg Crockett

5d. PROJECT NUMBER

5e. TASK NUMBER

5f. WORK UNIT NUMBER
2

7. PERFORMING ORGANIZATION NAME(S) AND ADDRESS(ES)

Logicon-RDA
2600 Yale Blvd SE
Albuquerque, NM 87106
(1998-2001)

Boeing-SVS
4411 The25 Way NE Suite 350
Albuquerque, NM 87109
(2001-present)

8. PERFORMING ORGANIZATION REPORT

9. SPONSORING / MONITORING AGENCY NAME(S) AND ADDRESS(ES)

Air Force Research Laboratory
Human Effectiveness Directorate, Directed Energy Bioeffects Division
Optical Radiation Branch
2650 Louis Bauer Drive
Brooks City-Base, TX 78235-5215

10. SPONSOR/MONITOR'S ACRONYM(S)
AFRL/HEDO

11. SPONSOR/MONITOR'S REPORT NUMBER(S)
AFRL-HE-BR-TR-2003-

12. DISTRIBUTION / AVAILABILITY STATEMENT
Approved for public release; distribution is unlimited.

13. SUPPLEMENTARY NOTES
Technical Monitor: Capt. Cecelia Montes De Oca (210) 536-3035

14. ABSTRACT
LRST is a software tool for calculating reflected energy hazards in the context of test range development of the Airborne Laser (ABL) system. The LRST software package consists of a suite of programs that provide facilities for describing and simulating test scenarios, including the range, the ABL aircraft laser complement, the target, and the observers. This manual provides a detailed description of the physical basis for the reflection models (BRDFs) implemented in LRST and methods for extracting Maxwell-Beard BRDFs from laboratory measurements..

15. SUBJECT TERMS
Airborne Laser, laser safety, directed energy bioeffects, laser range safety tool, LRST, Maxwell-Beard, BRDF

16. SECURITY CLASSIFICATION OF:			**17. LIMITATION OF ABSTRACT**	**18. NUMBER OF PAGES**	**19a. NAME OF RESPONSIBLE PERSON** Lt Col William P. Roach
a. REPORT Unclass	**b. ABSTRACT** Unclass	**c. THIS PAGE** Unclass	UL	71	**19b. TELEPHONE NUMBER** (include area code) (210) 536-4817

Standard Form 298 (Rev. 8-98)
Prescribed by ANSI Std. Z39.18

THIS PAGE INTENTIONALLY LEFT BLANK

Table of Contents

List of Figures

1.0   Introduction

A critical capability of the Laser Range Safety Tool (LRST) simulation is accurately modeling and predicting polarized power distributions reflecting from target missiles. At optical (visible and infrared) wavelengths, the classical radiance equations for radiometry are driven primarily by microscopic geometric effects. One normally expresses the scattering equations using the concept of the bidirectional reflectivity distribution function (BRDF) (Reference 1) which captures all the detailed scattering physics for how light interacts, whether in reflection or transmission, with a complex material surface structure. We will discuss three BRDF modeling representations used in the LRST. The first, most important, and only one that should seriously be used for accurately modeling target radiometry was developed at the Environmental Research Institute of Michigan (ERIM) by J.R. Maxwell and J. Beard (Reference 2). This will be called the Maxwell-Beard (MB) BRDF. (Two other empirical analytic BRDF models will be presented for completeness.) The Phong BRDF model (Reference 3) is a simplistic but venerable empirical approach used for years in computer graphics. Finally, the Gaussian BRDF model is a variation on several similar useful BRDF models for doing closed-form analytic analyses. These last two models are essentially two-parameter models with only very limited capability to capture otherwise complex scattering shapes.

This is not a complete list of available BRDF models currently used by the community for target signature prediction; we probably want to keep an open mind on incorporating other BRDF models in the future. These three, however, are the currently accepted standard models being used by AFRL for several simulation efforts and those simulations which they support with a material properties database. A requirement before adopting a new BRDF model will be to get acceptance by the AFRL community that controls the development of the computer-aided design (CAD) target modeling tool called the Solids Modeling Tool (SMT), and the companion material properties database called MATTER.DAT. It is important to recognize that LRST does not exist apart from an Air Force modeling tools and data intelligence infrastructure. New BRDF physics models will require writing new code for LRST, as well as for all other simulation programs that use MATTER.DAT. Also, the new material properties would need to be measured, extracted into BRDF model parameter fits, and added to MATTER.DAT as configuration-managed data items. New and different BRDF models would not impact the CAD models per se, only the materials database, because the CAD models reference the materials (and hence the BRDF models) via material code numbers.

We chose our modeling paradigm to be compatible with the AFRL Satellite Assessment Center (SatAC) modeling work for several reasons. First, SatAC offers considerable existing modeling expertise, materials database resources, capabilities, and experience; it currently builds the only nationally validated satellite CAD models accepted by the National Air Intelligence Center (NAIC). When LRST is used operationally, it too will need to import only those target models that have been validated, blessed, and configuration managed by NAIC. Second, SatAC does considerable high-energy laser (HEL) weapon vulnerability modeling using these same CAD models. Finally, this route will ultimately allow LRST to be applied to other HEL programs, such as the Space-Based Laser (SBL) or Tactical High Energy Laser (THEL) with the confidence that the target models will still be immediately compatible.

We will start with a general discussion of the BRDF and the usual approximations one makes. We derive the MB polarized BRDF equations in detail from first principles. Short equation presentations are then made for the Phong and Gaussian BRDFs. Next we discuss the algorithms to extract fitted BRDF parameters from measured laboratory BRDF data. For LRST type applications, the wavelength is very narrow band, and is centered at the laser wavelength. In fact, all target materials should be directly measured at all the relevant Airborne Laser (ABL) system wavelengths. However, other signature application codes need to model the BRDFs at many other wavelength bands, whether the BRDF data are measured or not. Therefore, we need to discuss how to interpolate/extrapolate the BRDFs to other unmeasured wavelengths. In LRST we fundamentally classify the scattered energy into two regimes, diffuse and specular. Diffuse goes into a full hemisphere, but specular goes predominantly into a restricted forward cone along the nominal specular direction. We will present algorithms that determine this effective specular lobe cone angle.

2.0   The Bidirectional Reflectivity Distribution Function (BRDF)

In the best of all situations we would have complete measurements for all possible combinations of wavelength, polarization, and incident and reflection geometry angles to accurately model the radiometric scatter for any material type and shape. Unfortunately this clearly is not possible due to the large number of variables, the relative difficulty and high cost of making precise BRDF measurements, and the unmanageable amount of digital data that would result. The BRDF is fundamentally driven by the physical state of random (isotropic or otherwise) surface roughness. This situation would therefore be further compounded by the infinite variety of material finishes possible for a single material type (e.g., aluminum milled, brushed, polished, anodized, or even painted). For semi-transmissive materials or coatings such as plastic or paint, more than one BRDF is required to complete the polarized scatter model, making things even more complicated.

While the possibilities for a physical BRDF are countless, most man-made materials manifest a BRDF functional form that is relatively simple and well behaved. The scatter usually decomposes down into two basic forms – wide-angle depolarized diffuse, and narrow-angle polarized specular. Diffuse reflections mostly depolarize the reflected light, while specular reflections tend to preserve the incident polarization. It will be shown that the Maxwell-Beard BRDF model allows us to take a minimum number of measured material optical properties in the laboratory, and accurately predict the *polarized* scatter for any combination of source-receiver geometry, using first principles and reasonable approximations where necessary. The primary advantage of this model over other BRDF models that do limited parameter fits is its ability to usually reproduce the original measured BRDF data almost exactly, especially for the monostatic direction. Because the BRDF curves are measured, the model inherently tends to be self-correcting when the actual scattering physics deviates from the assumed underlying first principle processes within the basic equations. In other words, because the MB BRDF model uses look-up tables taken from measured data, it tends to capture scattering physics not originally contained in the starting equations. As we shall see, the MB BRDF formalism starts with a reasonable and rigorous physical model, and ends up being a good parameter fit model.

We will try to follow the basic theoretical development as presented by ERIM (Reference 2) in several of their older documents (monographs). We will endeavor to follow their original notation. So far, however, we have been unable to find a complete and modern set of ERIM documentation that discusses all the algorithms we will present here. And, while ERIM (starting with the work of Torrance & Sparrow, Reference 4) clearly established the basic BRDF equations, many important algorithms needed for using this model are either not documented, or are documented only in part by various other authors. For example, the method for deriving the BRDF at a wavelength at which the BRDF parameters have not been explicitly measured, is very much open to interpretation and personal inclination (Reference 5).

No introductory BRDF discussion would be complete without the usual warnings about taking BRDF data, whether measured or simulated, too seriously. BRDF data apparently are very difficult to measure accurately, by anyone. Historically, round-robin measurement programs (in which a material sample is passed from laboratory to laboratory to have its BRDF measured) do not return consistent data. Between laboratories there are the usual differences between mechanical resolution, aperture size, stray light, detector noise levels, how the sample is held (stationary, spun), where on the sample the laser spot is placed, calibration specimens, optics, and polarization elements. Finally, there is an issue with the exact, current, real-world state of a target material surface. How old is the surface finish? Has it been changed by weather, oxidation, handling, sand-blasting, or heat? Just how valid are the accurately measured BRDFs that we use to do the simulation modeling? Do all targets of the same class really share the exact same BRDFs?

This is not to say that we know little about the target BRDFs. In general, a material's reflective property tends to become more diffuse with time. For example, it is difficult to maintain a clean shiny surface on a missile, especially if the missile is kept outside subject to weather. Therefore, if we use measured BRDF data from pristine material coupons, we are likely to overestimate the specular and underestimate the diffuse contributions. For the purposes of a safety analysis, this is probably adequate. We will make predictions closer to a hazard level in the specular directions, where it is the most important to be conservative, and slightly under-predict hazards in the less critical diffuse directions. We must be prepared for possible errors in the radiometry on the order of factors of 2 or more, due to our lack of knowledge of the exact target BRDFs.

We should always strive to use the best engineering knowledge of the scenario and BRDFs. But we also need to recognize and accept some level of uncertainty in our simulation, balancing the simulation's fidelity against what we know about the uncertainties.

2.1   First-Surface Scatter BRDF

The MB BRDF model relies entirely on in-plane measurements. That is, the receiver sensor measures the reflected intensities at various scan positions in the plane of incidence of the laser source. The plane of incidence contains the incident laser light rays and the material surface normal vector. Classically the source is polarized with the electric vector axis either parallel (i.e., P polarization) or perpendicular (i.e., S polarization) to the plane of incidence. The receiver can also resolve the scattered light into one of these two directions using a linear polarizer. Usually

four in-plane scans are made to cover each combination: S to S (SS or $\perp\perp$), S to P (SP or $\perp\|$), P to P (PP or $\|$), and P to S (PS or $\|\perp$). From these measured data, MB model parameters are extracted and put into a material properties database. Simulation programs can then access the material properties, on a material code basis, and both reconstruct the BRDF for in-plane geometries, and predict (i.e., extend) the BRDF for out-of-plane geometries.

Going back several hundred years, it was recognized that the surfaces of opaque materials reflected visible light from a large number of microscopic facets (micro-facets) inherent in randomly rough surfaces. The dominant effect is for light to specularly reflect off these little mirror facets (or sequins) in all directions, the angular spread being driven by the micro-facet tilt statistics. Since the micro-facets are very smooth at the microscopic level, the polarization then tends to follow the Fresnel laws of reflection.

In fact, the primary assumption in the Maxwell-Beard BRDF model is that within the visible and infrared wavelength regions, the micro-facet reflection process is entirely specular, geometric (i.e., minimal wave effects), and driven by Fresnel's laws at the first air-material surface interface. Light is scattered out-of-plane by micro-facets tilted out of the plane of incidence, for instance. Figure 2.1 depicts how only a relatively few (correctly tilted) micro-facets actually reflect light back to a sensor.
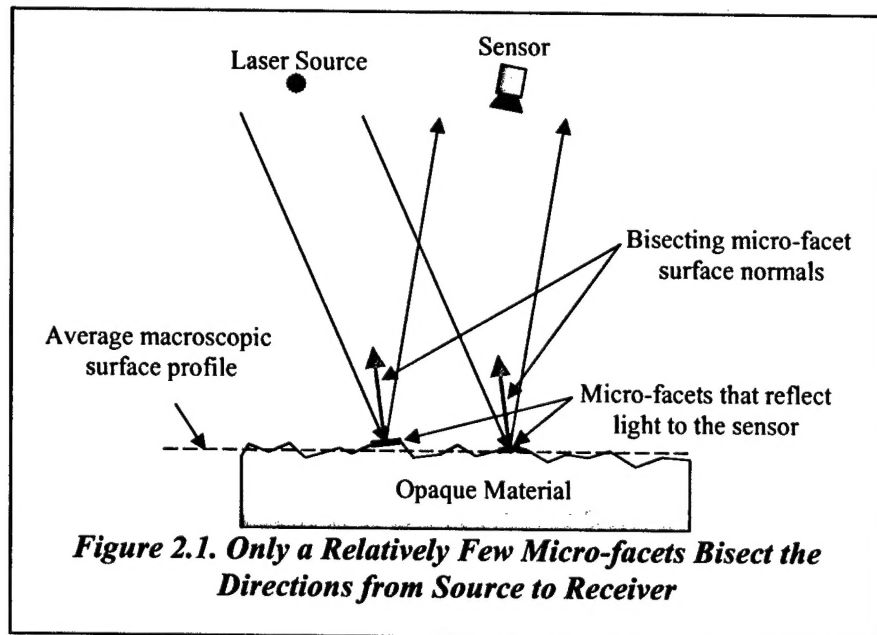
Figure 2.1. Only a Relatively Few Micro-facets Bisect the Directions from Source to Receiver

These few physical assumptions seem to be well satisfied by most man-made machined materials with a fairly smooth finish. However, extremely rough surface finishes lead to complex multiple reflections of the light within the first-surface micro-structure, and hence both depolarize the light and spread the distribution of scattered light into all directions more uniformly (i.e., diffuse scatter). Extremely rough surfaces are not well modeled by the Maxwell-Beard first-surface BRDF model except where the derived parameters are especially crafted to follow a diffuse distribution. At the other extreme, when the first-surface becomes very smooth compared to the wavelength, wave effects begin to become more important than the geometric effects. Also, the MB BRDF model cannot easily handle mirror-like surface finishes (roughness very much less than the wavelength). Only optical elements such as mirrors and lenses have both smooth surface finishes and well-controlled surface figures. Therefore, it is not likely that an exterior material for
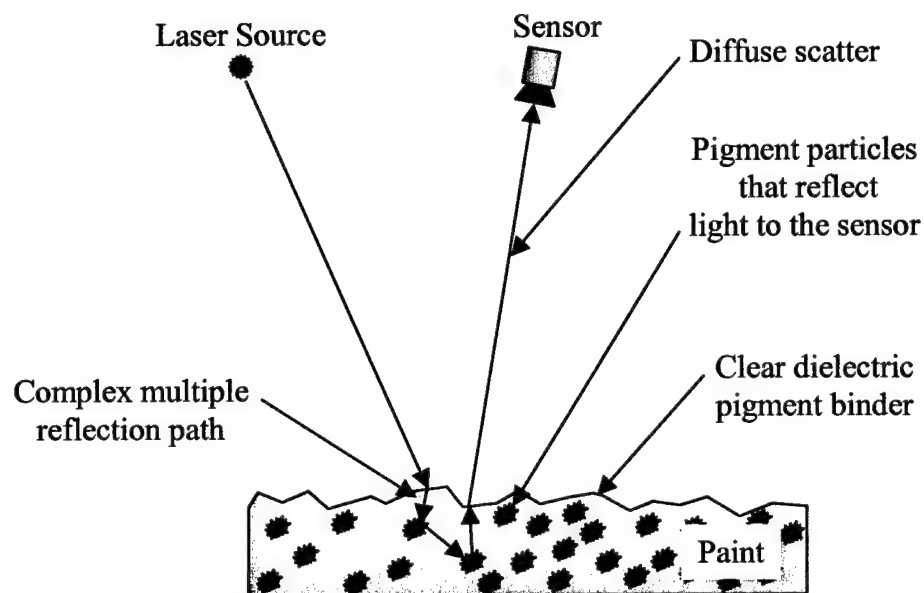
Figure 2.2. Volumetric Scatter from Pigment Particles

a missile will have a material finish that is optically shiny and which supports coherent far-field constructive interference.

If the material is a metal, then light penetrates the first-surface to a depth on the order of only a few wavelengths. The entire scattering process is contained in just the single interaction of light with the opaque first-surface micro-facets. For paints, the first-surface both reflects and transmits most of the incident light into its bulk region.

2.2   Volumetric Scatter BRDF

Dielectric materials such as paints and plastics exhibit a more complex reflection mechanism. On a microscopic level, light can penetrate and undergo very complex multiple reflections off pigment particles suspended in the clear dielectric plastic binder within a shallow volumetric region behind the first-surface. The detailed interaction process would be extremely difficult to model, even with very comprehensive measured material property information (which of course *never* seems to be available). The MB BRDF model approximately captures this complex volumetric scatter physics by using two diffuse BRDF functional forms whose parameters are derived again from the in-plane scan data.

The net scatter from dielectric materials then includes two reflections, one due to the first-surface Fresnel reflection, and a second due to multiple reflections off pigment particles in the shallow volumetric region just below the first-surface. Figure 2.2 gives a notional depiction of how just one ray of light might scatter back to the sensor.

The first-surface reflection, therefore, is again a function of the distribution of randomly tilted, specularly reflecting, dielectric micro-facets. Given the source and receiver directions, only those micro-facets whose local surface micro-facet normal bisects the incident and reflected directions

contribute to the instantaneous scatter measured at the receiver aperture. Thus, the scatter intensity is proportional to the number of correctly tilted micro-facets and the relative area they subtend.

Fresnel's equations are used to handle the polarization effects. The first-surface scatter is assumed to be always polarized because Fresnel's equations do not provide for depolarization. When the first-surface becomes very rough (e.g., has deep grooves), light incident from directions near normal tend to bounce more than once from the highly tilted micro-facets. This both depolarizes and diffusely distributes the emerging light, which contradicts the above assumption of single reflections off micro-facets that preserve polarization. Shifting this fraction of the scatter into the depolarized volumetric diffuse terms captures this effect.

Contrary to MB assumptions, in reality wave effects are always present. A certain amount of diffraction always exists and tends to spread the specular lobe slightly. While the purely geometric assumption is violated (albeit only slightly for most materials), the model inherently recovers somewhat by relying on the actual measured scan curves, wave effects included.

We can start our mathematical discussion by stating a useful definition of the BRDF when the incident light is collimated:

$$\text{BRDF} = \rho^{'}(\theta_i, \varphi_i, \theta_r, \varphi_r) = \frac{\delta L_r}{\delta E_i} = \frac{\dfrac{\delta P_r}{\delta A \cdot \cos(\theta_r) \cdot \delta\Omega_{rec}}}{\delta P_i / \delta A} \qquad (\text{sr}^{-1}) \qquad (2.1)$$

where,

δL_r	= the incremental reflected radiance from a flat surface (W/m²-sr)
δE_i	= the incremental incident irradiance (W/m²)
δP_i	= the power incident on the differential area δA
δP_r	= the power reflected into the incremental solid angle $\delta\Omega_{rec}$ from area δA (W)
θ_i	= the polar angle of the incident light (down from the local surface normal)
φ_i	= the azimuthal angle of the incident light (measured from some local in-plane axis)
θ_r	= the polar angle of the receiving aperture
φ_r	= the azimuthal angle of the receiving aperture
δA	= the differential area of the reflecting macroscopic surface (m²)
$\delta\Omega_{rec}$	= the differential solid angle subtended by the receiving aperture (sr)

We will freely interchange our notation of the BRDF with ρ′. The BRDF stated in Equation 2.1 is simply a ratio of reflected directional radiance to incident irradiance. We will want to add to our notion of the BRDF by keeping track of variables such as polarization, wavelength, material type, specular and diffuse contributions, and so forth. Notice that any dependence on the incident cone solid angle has been simplified to $\delta P_i/\delta A$. For most laser illumination scenarios, certainly for the ABL ones, the incident light is collimated to within tens of micro-radians across the whole of the target, and extremely collimated locally. The effective BRDF for light sources such

as the sun with a finite extent (i.e., a finite incident solid angle) can be constructed from the collimated BRDF if necessary.

2.3   Assumptions and Approximations

A real BRDF is typically a function of a large number of variables, too large to manage without making some assumptions. Geometric variables include the azimuth and polar angles of the incident light; the azimuth and polar angles of the reflected direction; the local surface curvature; and the specific location on a surface element. Other important variables include wavelength band (which leads to an effective reflectivity), complex indices of refraction, incident polarization state, receiver polarization sensitivity, material type or detailed microstructure, material finish state (e.g., smooth or rough), and shadow/masking effects. We typically have the capability to generate separate BRDF objects for different materials, at different wavelengths; however, directional or polarization effects are derived from the basic measured BRDF data. To keep the amount of required supporting measured data manageable, we will need to make some assumptions and reasonable approximations.

We will simplify our radiometric equations by first assuming that the geometry follows reasonably closely that encountered for the ABL scenarios of interest. We will always assume that the incident rays are parallel, with the same polarization state. This is the far-field assumption for the laser source. The difference in the incidence angles for rays at the nose or tail of a missile is tens of micro-radians, which is well below the angular spread of even a very shiny surface (e.g., specular lobe width of 0.1 degree). Likewise, we assume that the receiving aperture is at a sufficiently large distance from the scattering surfaces that all the reflected rays are essentially collimated at the receiving aperture. This has a twofold importance in our equations. First, because the receiving aperture is again assumed in the far field of the scattering target, each unit vector along the reflected direction from each small scattering incremental area on the target to the receiving aperture is parallel to the other unit vectors. Second, the dimension of the collecting aperture is assumed to be much smaller than the BRDF angular spread. This ensures that we can accurately calculate the reflected intensities at the receiver aperture using a linear approximation. We calculate the irradiance at a single point, located at the center of the receiving aperture, and linearly scale it with aperture area, without doing a detailed spatial integration over the aperture area. These two assumptions allow us to reduce the number of spatial integrals and thereby increase efficiency without losing accuracy. The motivation is to increase execution speed, and making these approximations introduces negligible error in the radiometrics (and none in the BRDF).

Next we need to assume that the BRDF is isotropic and invariant in several ways. We assume the BRDF is identical for the same material assignments for all target models. All assignments of *0001 Aluminum Alloy, 2024-T3, Polished*, for example, should render the same because the BRDF data are the same. This assumption breaks down when one considers the life history of a particular target in the real world unless it is somehow sealed off from the environment. We assume that the BRDF is invariant over the entire surface of the element it is assigned to. Variations in surface finish or color are assumed small for even large area coverage. We must assume that the micro-facet tilt distribution function is statistically isotropic in azimuth. This

removes any absolute azimuthal dependency of the BRDF. Some metal finishes, for example, tend to have striations that are machine-tool grooves. This tends to produce anisotropic BRDFs that vary with the azimuth angle that is tied to surface coordinates. The BRDFs we measure are all taken at room temperature and represent how the surface scatters light at normal temperatures. At extreme melting temperatures the BRDF is clearly going to make nonlinear changes. Usually, but not certainly, the color will turn darker and the surface will become rougher because of the degradations cause by elevated temperature. For the current version of LRST, we assume that the BRDFs are invariant with temperature. Each of these assumptions is fairly reasonable for most cases, though there are exceptions. Common techniques—such as texture mapping—do exist for handling local variations, but LRST, for now, will adhere to these isotropic assumptions and not implement more complex algorithms.

A real BRDF is usually highly complex. The possibilities for scatter are literally endless. However, we need to reduce the complexity to something manageable in code. We assume that all BRDFs are well behaved and have a few common properties. We always use measured data where it exists. There is always a certain amount of data smoothing and averaging when extracting representative optical parameters. We always assume that the BRDF is separable into two components: a polarized first-surface specular lobe that scatters light into a cone about the nominal specular direction; and a depolarized hemispheric diffuse scatter that basically follows a Lambertian distribution, coming from the volumetric region. We are basically considering just two common material types, metals and opaque paints or plastics. The out-of-plane scatter is either Lambertian, or derives from those micro-facets that are tilted out-of-plane. In either case, all scatter is mostly a direct consequence of geometric reflection and not wave effects.

We then assume that the BRDF will have approximately the same spatial distribution regardless of wavelength, as long as the wavelength is not too different from that used to measure the BRDF material properties. This allows us to interpolate a BRDF to a wavelength for which we have no measured data beyond the net directional hemispherical reflectivity (DHR). We shall borrow the BRDF spatial distribution function and renormalize to the new reflectivity. We also need to recognize that it is the complex indices of refraction that determine the hemispherical reflectivity of metals. The indices likewise determine the first-surface reflectivity of dielectrics, but they tend to be wavelength invariant, meaning that the first-surface reflectivity remains at a constant low value for large wavelength shifts. The dominant reflection effect for paints and plastics is the bulk region scatter which is assumed Lambertian (or nearly so - see the MB model below), and is controlled by the bulk reflectivity.

The BRDF is commonly measured for nominally flat surface profiles. Surface curvature radiometric effects are accounted for independently of the BRDF, by either analytically integrating around the curved part, or by evaluating the radiometrics at many locally flat differential areas (i.e., essentially numerically integrating). There is definitely a coupling between curvature and the specular reflection: a shiny cylinder reflects light into a thin bright ring around itself, whereas, a flat plate projects a small round spot. Diffuse surfaces, on the other hand, are affected less by local curvature because the fall-off occurs as only a cosine of the polar angle. We will still track the diffuse scatter for small locally flat areas.

Finally, we need to ensure that whatever the BRDF functional form, an integral of the outgoing scattered intensities over the hemisphere above the scattering surface, is equal to the measured hemispherical reflectivity. The hemispherical reflectivity is itself a function of wavelength, and is independently measured in the laboratory. We will need to address the normalization procedures for each of the BRDFs below, since this is the basis for our radiometric energy balance. The hemispherical reflectivity is related to the BRDF by

$$\text{DHR} \ (\theta_{in}, \lambda) = \frac{\sum\limits_{hemisphere} \delta P_r}{\delta P_i} = \int\limits_{hemisphere} \text{BRDF} \ \cdot \cos(\theta) \cdot d\Omega \quad (2.2)$$

and can be expressed more completely as:

$$\text{DHR} (\theta_{in}, \lambda) = \int\limits_{0}^{2\pi} \int\limits_{0}^{\pi/2} \text{BRDF}(\theta_{in}, \lambda, \theta, \varphi) \cdot \cos(\theta) \cdot \sin(\theta) \cdot d\theta \cdot d\varphi \quad (2.3)$$

where we have indicated that the hemispherical reflectivity is a function of wavelength and the incident angle of the light. We use the notation $\text{DHR}(\theta_{in}, \lambda)$, which stands for directional hemispherical reflectivity. This quantity is a function of wavelength, but it also changes with the angle of incidence for all materials. We will consider $\text{DHR}(\theta_{in} = 0, \lambda)$ for normal incidence.

3.0 Derivation of the Maxwell-Beard ρ' BRDF formulation

Consider an illumination-reflection-sensor geometry like that shown in Figure 3.1. The laser is assumed to present a uniform monochromatic collimated irradiance over the test sample surface; the sample is nominally flat and isotropic; and the sensor is located in the far field. The sensor has a small receiving aperture that subtends a relatively small but non-zero collecting solid angle $\delta\Omega_r$.
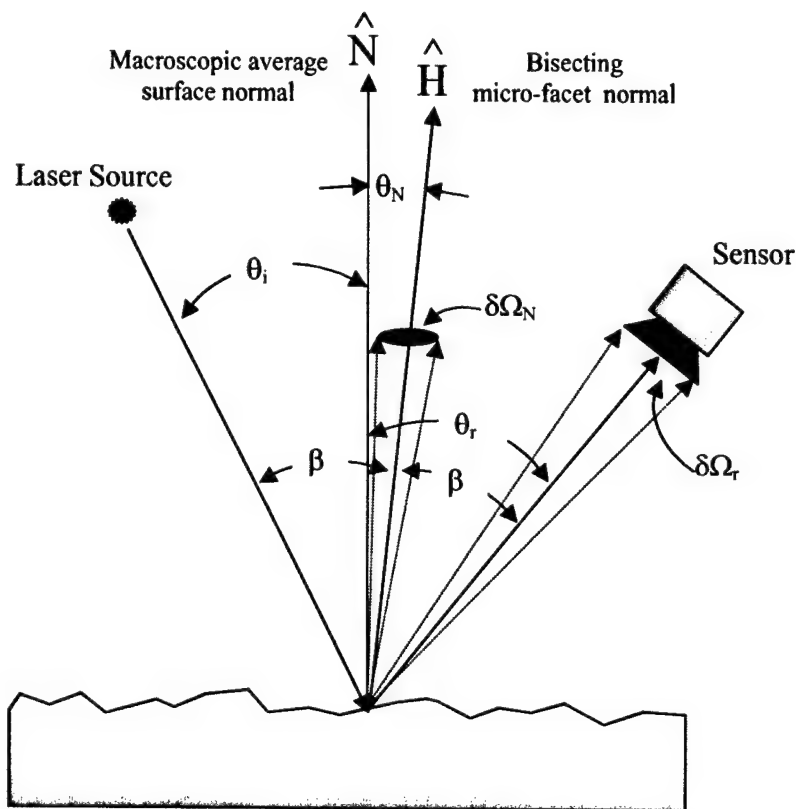
Figure 3.1. Basic Geometry and Notation for the BRDF Model Equations

3.1 The Polarized Specular BRDF

Let $\Xi(\theta_N, \varphi) \cdot d\Omega_N$ represent a distribution function which gives the relative fraction of the material surface area whose micro-facets are tilted relative to the macroscopic average surface normal, along a direction (θ_N, φ), where these are the usual polar angles, and all within a small solid-angle cone $\delta\Omega_N$. By our isotropic roughness assumption we realize in effect that $\Xi(\theta_N, \varphi) = \Xi(\theta_N)$.

All micro-facet surface normals that fall within a small solid angle $\delta\Omega_N$ centered about the bisecting direction $\hat{H}$, between light source and receiver, will scatter light (geometrically) into the receiver aperture solid angle such that (cf. Figure 3.1):

$$\delta\Omega_r = 4 \cdot \cos(\beta) \cdot \delta\Omega_N \qquad \text{(sr)} \qquad (3.1)$$

While Equation 3.1 might not be obvious at first glance, it is a consequence of the optical gains for differential tilts of the micro-facet mirrors. We have shown (Reference 6) that a mirror that moves an angle $\delta\theta_{mirror}$ in-plane of source and receiver causes a change in the reflected ray line of sight (LOS) of $\delta\theta_{LOS} = 2 \cdot \delta\theta_{mirror}$, exactly. A mirror that moves an angle $\delta\theta_{mirror}$ cross-plane of source and receiver causes a change in the reflected ray LOS of $\delta\theta_{LOS} = 2 \cdot \cos(\beta) \cdot \delta\theta_{mirror}$, where β is the angle between the incident (or reflected) LOS and the bisecting micro-facet normal $\hat{H}$, and where small angular changes are assumed valid. A product of these two terms leads directly to Equation 3.1 above.

For a given unit surface area with light incident upon it, the micro-facets whose normals are tilted at an angle θ_N with respect to the average macroscopic surface normal will reflect light into the receiver aperture solid angle. Typically, only a small fraction of the total surface area has micro-facets that satisfy this condition. For now, assume that all such micro-facets are neither shadowed nor masked. For a small surface area element δA, the net amount of that surface area that has micro-facets tilted toward the receiver (i.e., along θ_N, δ) is defined as:

$$A(\theta_N, \varphi) = \Xi(\theta_N, \varphi) \cdot \delta A \cdot \delta\Omega_N \quad (\text{m}^2) \qquad (3.2)$$

The net power incident on these micro-facets is simply:

$$P_{facets} = \frac{\delta P_i}{\delta A \cdot \cos(\theta_i)} \cdot A(\theta_N, \varphi) \cdot \cos(\beta) \qquad \text{(watts)} \qquad (3.3)$$

where we recognize $\dfrac{\delta P_i}{\delta A \cdot \cos(\theta_i)}$ as the irradiance perpendicular to the beam, and where $A(\theta_N, \varphi) \cdot \cos(\beta)$ is the projected area of the participating micro-facets.

3.2   The Fresnel Reflection Function

We assume that the fundamental mechanism for reflection at the first air-material surface, and therefore for all polarization effects, is driven by Fresnel's equations. Consider the situation of external reflection where light is incident from the exterior of a target surface and where the incident medium is either air or vacuum (i.e., $n = 1.0$), and the second medium is either a dielectric or a metal. When the angle of incidence for light flux is θ_i, the refraction/reflection angle is θ_r and the complex index of refraction is N, then Snell's law predicts the angle of refraction/reflection to be:

$$\frac{\sin(\theta_i)}{\sin(\theta_r)} = N = n - i\kappa \tag{3.4}$$

N is independent of the angle of incidence, and given in the usual optics form $N = n - i\kappa$, where κ is always positive. The pair of complex indices of refraction (n, κ) must reside in the first quadrant as long as the incident medium has an index of refraction lower than that of the bulk material. Thin layers are not considered here, so the index of refraction applies to the bulk of the material and does not depend on its thickness. Index pairs in the second and third quadrants (i.e., where n is negative) should not be allowed, since light would then be incident at a surface where the material is in an excited state and hence the reflectance would be greater than 1. Typically, clear dielectrics exhibit an absorption index κ equal to or nearly equal to zero. Metals, on the other hand, have a nonzero κ and are opaque (absorbing). In the infrared, some dielectrics can also become absorbing, and therefore would probably not show the usual diffuse bulk region scatter.

The reflectance functions for a smooth dielectric (or for a small differential area of dielectric on the microscopic level) with a monochromatic beam incident at an oblique angle β is designated by $R_{XX}(\beta)$, where we shall use the notation R_{SS} for the reflectivity when the incident and reflected electric field vectors are *perpendicular* to the plane of incidence, and R_{PP} for the reflectivity when the incident and reflected electric field vectors are *parallel* to the plane of incidence. The rigorous formulas for the reflected flux are:

$$R_{SS}(\beta) = \frac{(a - \cos(\beta))^2 + b^2}{(a + \cos(\beta))^2 + b^2} \tag{3.5}$$

$$R_{PP}(\beta) = R_{SS} \cdot \frac{(a - \sin(\beta) \cdot \tan(\beta))^2 + b^2}{(a + \sin(\beta) \cdot \tan(\beta))^2 + b^2} \tag{3.6}$$

where the a and b intermediate terms above are derived from:

$$x = n^2 - \kappa^2 - \sin^2(\beta) \tag{3.7}$$

$$y = \sqrt{x^2 + 4 \cdot n^2 \cdot \kappa^2} \qquad (3.8)$$

$$a^2 = \frac{x + y}{2} \qquad (3.9)$$

$$b^2 = \frac{y - x}{2} \qquad (3.10)$$

Notice, in theory, there is no cross-coupling between the two orthogonal linear polarization states:

$$R_{SP}(\beta) = R_{PS}(\beta) = 0 \qquad (3.11)$$

Later we discuss mechanisms for depolarization where there will exist cross-coupled states. Figures 3.2 through 3.5 present some typical Fresnel curves calculated using the above equations. The calculated curves compare exactly to those published by Holl (Reference 7).
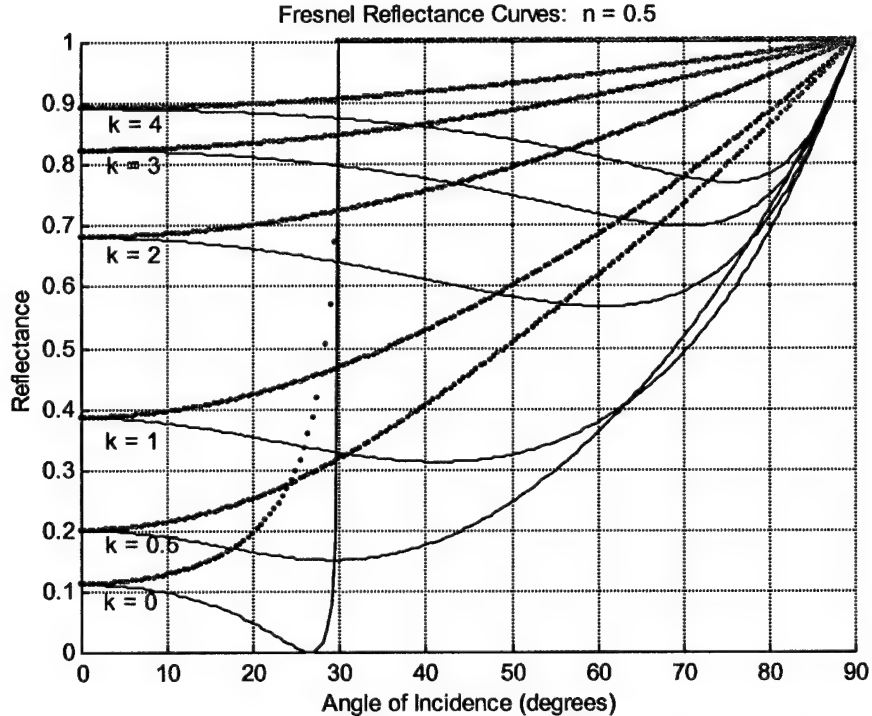
Figure 3.2. Parametric Fresnel Reflectance Curves for Various Combinations of n = 0.5: and κ = 0, 0.5, 1, 2, 3, 4; R_SS is the dotted upper curve, R_PP is the solid lower curve.
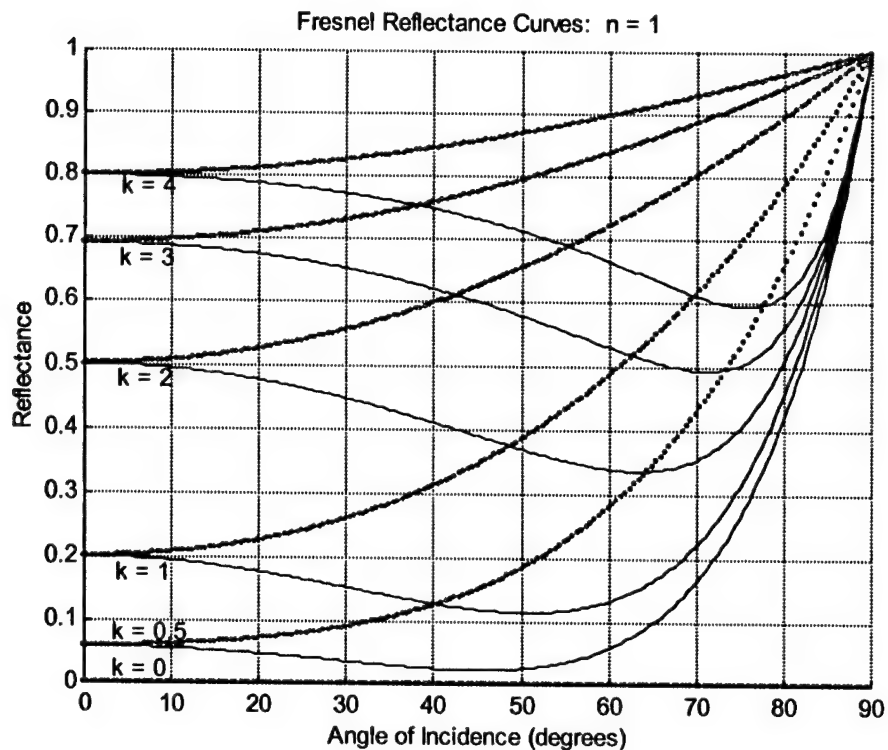
Figure 3.3. Fresnel curves for n = 1.5 *and* κ *= 0, 0.5, 1, 2, 3, 4*
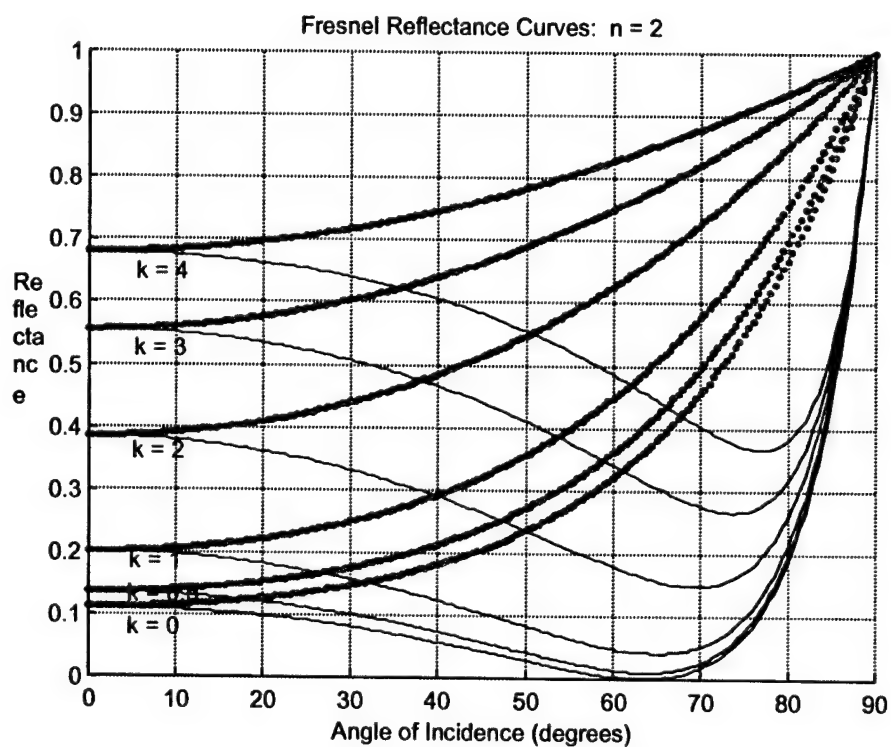
Figure 3.4. Fresnel curves for n = 2.0 *and* κ *= 0, 0.5, 1, 2, 3, 4*

The effective Fresnel reflectivity for unpolarized natural light, or circularly polarized light, is the arithmetic mean of the two reflectivities:

$$R_{unpolar} = \frac{R_{SS} + R_{PP}}{2} \tag{3.12}$$

For angles where R_{SS} is greater than R_{PP}, unpolarized incident light gets slightly polarized. The degree of this polarization, P, is defined as:

$$P = \frac{R_{SS} - R_{PP}}{R_{SS} + R_{PP}} \tag{3.13}$$

While the equations for the Fresnel reflectivities above are simple enough to calculate numerically, there are some interesting aspects worth discussing.

At normal incidence, the S and P reflectivities should be the same:

$$R_{PP}(0) = R_{SS}(0) = \frac{(n-1)^2 + \kappa^2}{(n+1)^2 + \kappa^2} \tag{3.14}$$

The normal incidence reflectivity is a function of the two indices. It is useful to solve for either n or κ, given the normal incidence reflectivity $R(0)$ and the other index. For instance, the complex index κ is:

$$\kappa = +\sqrt{\frac{R(0) \cdot (n+1)^2 - (n-1)^2}{1 - R(0)}} \tag{3.15}$$

where we take only the positive root. Likewise we can solve for the real index n by:

$$n = \frac{1 + R(0)}{1 - R(0)} \pm \sqrt{\left(\frac{1 + R(0)}{1 - R(0)}\right)^2 - (\kappa^2 + 1)} \tag{3.16}$$

where either root is valid, but the smaller is probably the useful one.

Upon reflection, each component of the electric field undergoes a phase retardation given by:

$$\tan(\delta\varphi_P) = \frac{2 \cdot \cos(\beta) \cdot \left[(n^2 - \kappa^2) \cdot b - 2 \cdot n \cdot \kappa \cdot a\right]}{\left[(n^2 + \kappa^2)^2 \cdot \cos^2(\beta) - (a^2 + b^2)\right]} \tag{3.17}$$

$$\tan(\delta\varphi_S) = \frac{2 \cdot \cos(\beta) \cdot b}{\cos^2(\beta) - (a^2 + b^2)} \tag{3.18}$$

The *relative* phase retardation between the P and S directions upon reflection is given by:

$$\Delta\varphi_{PS} = \delta\varphi_P - \delta\varphi_S = \tan^{-1}\left[\frac{\tan(\delta\varphi_P) - \tan(\delta\varphi_S)}{1 + \tan(\delta\varphi_P)\cdot\tan(\delta\varphi_S)}\right] \tag{3.19}$$

$$\Delta\varphi_{PS} = \tan^{-1}\left[\frac{2\cdot b\cdot\sin(\beta)\cdot\tan(\beta)}{\sin^2(\beta)\cdot\tan^2(\beta) - (a^2 + b^2)}\right] \tag{3.20}$$

To get a feel for typical Fresnel equations we will plot a few quantities. Figure 3.6 shows a set of typical Fresnel curves, including the relative phase shift, where $n = 2.01$ and $\kappa = 2.05$.

The phase shift curve starts at 180 degrees and goes to zero at grazing incidence. The Brewster angle is where R_{PP} has a minimum (about 70 degrees here).
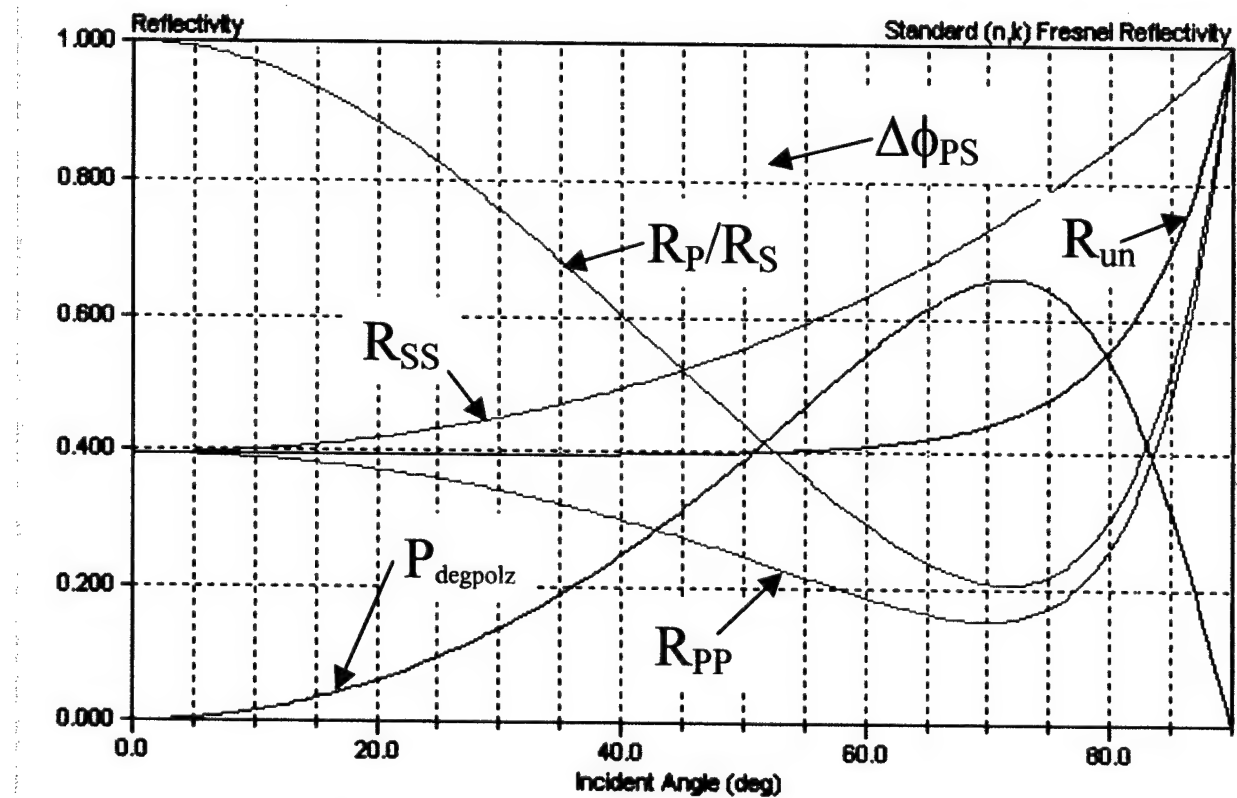
Figure 3.5. Typical Fresnel Curves R_{SS} *(green),* R_{PP} *(red),* $R_{unpolar}$ *(black); the relative phase shift* $\Delta\varphi_{PS}$ *is shown dropping from* π *to 0 (yellow-phase angle not labeled); the degree of polarization is shown at the bottom (magenta); the ratio of* R_P/R_S *is shown starting from the upper left (purple)* $(n = 2.01, \kappa = 2.05)$.

In Figure 3.7, a set of isoreflectance curves is drawn as a function of the two components of the refractive index. The red dot represents the index for the material displayed in Figure 3.9.
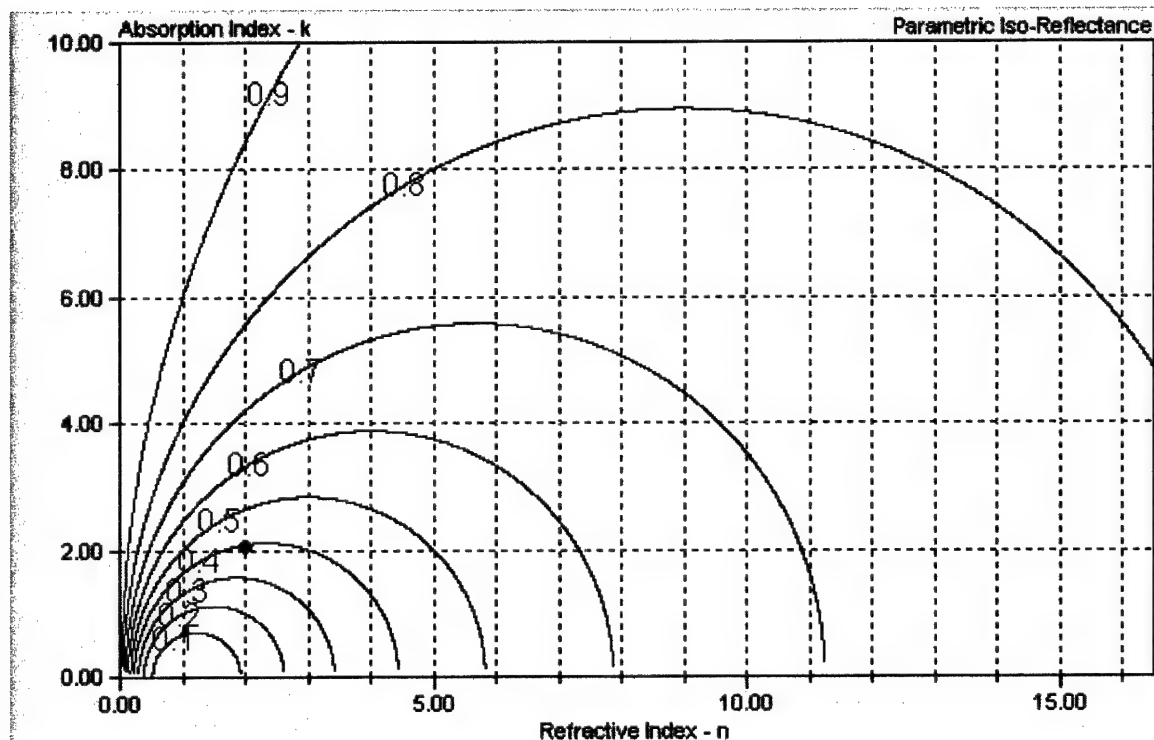
Figure 3.6. Isoreflectance Curves for Varying Normal Incidence Reflectivity

The curves are circles of constant normal incidence reflectivity (given by Equation 3.14). Usually the real component of the refractive index is reported as a relatively small value (less than 3). This means that the complex index component κ changes rapidly with increasing normal incidence reflectivity for a constant real index.
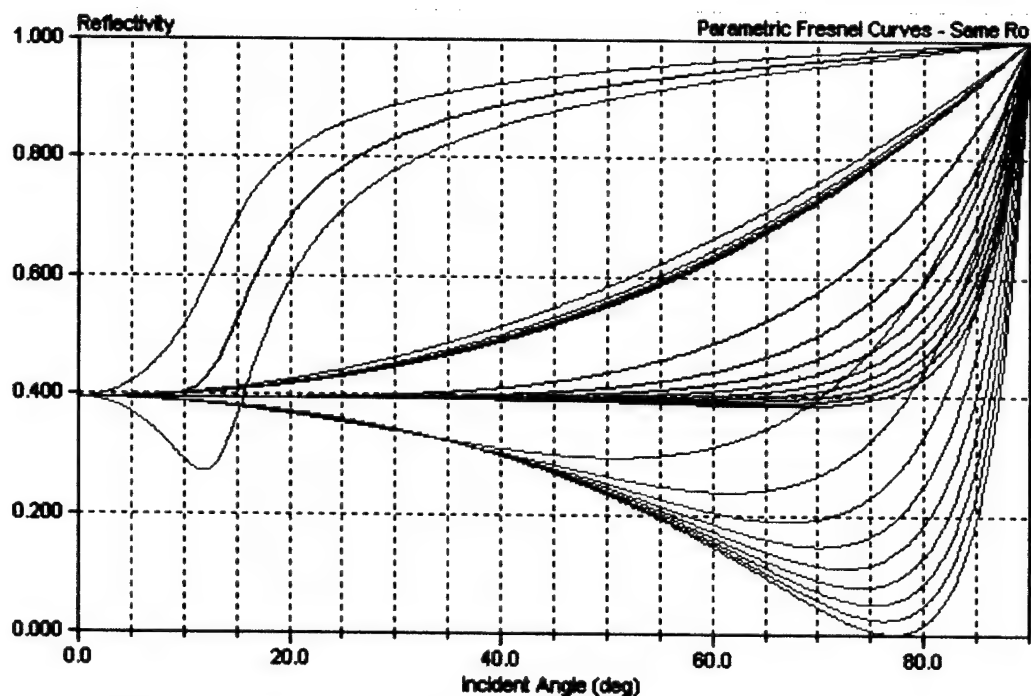
Figure 3.7. Parametric Families of Fresnel Curves for Varying **n, k,** *with Constant Normal Incidence Reflectivity (Ro = 40%); the effect of larger index* **n** *is to push the Brewster angle to the right and depress the* **R_PP** *reflectance.*

Figure 3.8 shows a family of Fresnel curves in which n and κ were again varied such that the normal incidence reflectance $R(0)$ remains constant (i.e., follow the 40% isoreflectance curve in Figure 3.7). Notice how the Brewster angle quickly changes from small values when the real part of the index is small, to large angles as n increases. For example, when n is about 0.3, the Brewster angle is about 30 degrees, whereas when n is about 1.0, the Brewster angle is almost 60 degrees.
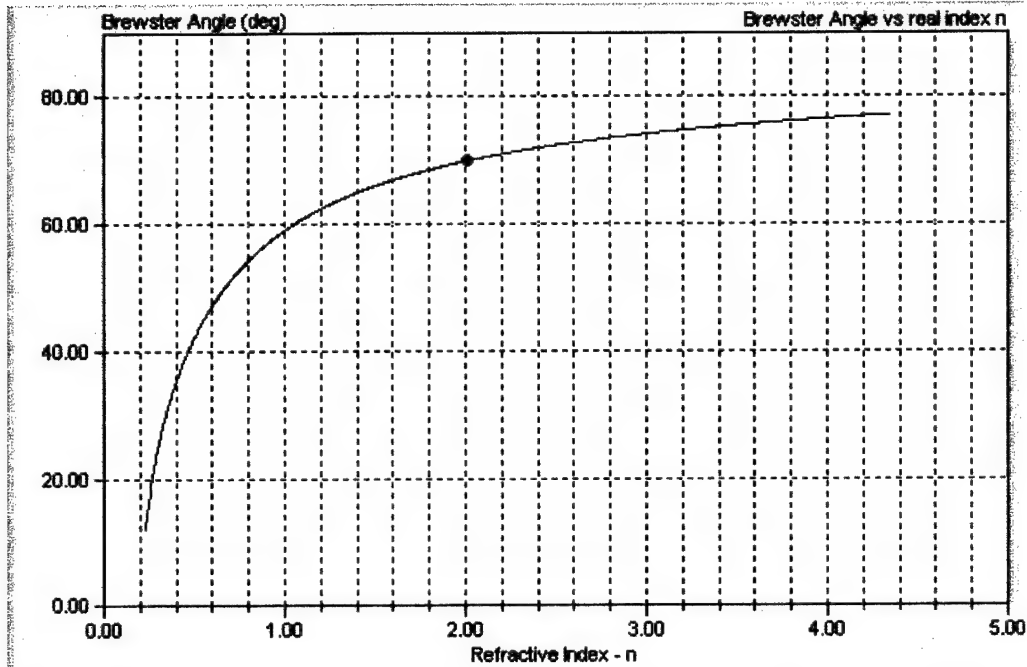
Figure 3.8. Variation of the Brewster Angle VSO Real Index* n *(Ro=40%)

Figure 3.9 directly shows the variation of the Brewster angle when *n* (and *k*) are changed to keep the normal incidence reflectivity constant (Ro = 40%). Again, notice how the Brewster angle does not change much for values of *n* above about 1.0. Said differently, the Brewster angle seems to be a strong function of the real index when *n* is less than 1.0. Thus, while there are many index pairs that satisfy the normal incidence reflectivity, different pairs produce different Brewster angles and different R_S and R_P curves, the most pronounced variation being in the R_P curves (cf. Figures 3.8 and 3.9).

3.3 The First-Surface BRDF as a Function of the Tilt Distribution Function

Solving Equation 3.1 for $\delta\Omega_N$ and substituting it into Equation 3.2 gives the net surface area that bounces light into the receiver aperture geometrically:

$$A(\theta_N, \varphi) = \Xi(\theta_N, \varphi) \cdot \delta A \cdot \frac{\delta\Omega_r}{4 \cdot \cos(\beta)} \ (\text{m}^2) \qquad (3.21)$$

Substituting this area into Equation 3.3 gives the amount of incident power at the micro-facets:

$$\delta P_{facets} = \frac{\delta P_i}{\cos(\theta_i)} \cdot \Xi(\theta_N, \varphi) \cdot \frac{\delta\Omega_r}{4} \quad (\text{watts}) \qquad (3.22)$$

The amount of power that is reflected depends on the incident polarization state. Knowing the Fresnel reflectance R_{xx} (where X can be S or P), we can determine the amount of power collected by the receiver aperture:

$$\delta P_r = \delta P_{facets} \cdot R_{XX} = \frac{\delta P_i}{\cos(\theta_i)} \cdot \Xi(\theta_N, \varphi) \cdot \frac{\delta \Omega_r}{4} \cdot R_{XX} \quad \text{(watts)} \quad (3.23)$$

Finally, rearranging Equation 3.23 to look like the right-hand side of Equation 2.1 for the BRDF, we get:

$$\rho'(\theta_i, \theta_r, \beta, \theta_N) = R_{XX}(n, \kappa, \beta) \cdot \frac{\Xi(\theta_N)}{4 \cdot \cos(\theta_i) \cdot \cos(\theta_r)} \quad (\text{sr}^{-1}) \quad (3.24)$$

where θ_i is the incident angle of the light with the average macroscopic surface normal, θ_r is the angle the receiver LOS makes with the surface normal, β is the angle between the bi-section unit vector $\hat{H}$ and either the incident or reflected LOS unit vectors, and θ_N is the angle $\hat{H}$ makes with the surface normal. The bi-section unit vector $\hat{H}$ is the same as the micro-facet local normal:

$$\hat{H} = \frac{\hat{V}_i + \hat{V}_r}{\left| \hat{V}_i + \hat{V}_r \right|} \quad (3.25)$$

where $\hat{V}_i$ is the unit vector LOS to the laser source, and $\hat{V}_r$ is the unit vector LOS to the receiver aperture. The angle θ_N is easily derived from the geometry:

$$\theta_N = \cos^{-1}(\hat{H} \circ \hat{N}) \quad (3.26)$$

where $\hat{N}$ is the macroscopic surface normal. The angle β is also easily derived from the geometry:

$$\beta = \cos^{-1}(\hat{H} \circ \hat{V}_i) = \cos^{-1}(\hat{H} \circ \hat{V}_r) \quad (3.27)$$

To work the fully polarized reflection, Equation 3.24 is needed twice, once for each incident electric field component (i.e., R_{SS} and R_{PP}). For the LRST application, we assume for now that the incident laser beam polarization state is circularly polarized. The first-surface Fresnel reflectance then would be the mean of the S and P, and hence $R_{XX} = R_{unpolar} = \frac{R_{SS} + R_{PP}}{2}$ (Equation 3.12).

Equation 3.24 seems easy enough to use in a rendering algorithm. Only three quantities need to be measured: the two indices of refraction (n, κ), and the tilt distribution function $\Xi(\theta_N)$. In the laboratory we can only infer $\Xi(\theta_N)$ by making in-plane monostatic (sometimes called a zero bistatic, or quasi-monostatic) BRDF scans. In the monostatic measurement configuration, the

incident and reflected angles are equal to each other and to θ_N. Equation 3.24 can then be inverted to give:

$$\Xi(\theta_N) = \rho'_{mono}(\theta_N) \cdot \frac{4 \cdot \cos^2(\theta_N)}{R(\beta = 0)} \quad (sr^{-1}) \tag{3.28}$$

where $\rho'_{mono}(\theta_N)$ represents the measured monostatic BRDF data. The Fresnel reflectivity in the denominator is for normal incidence, and hence is independent of polarization state. Typically in the rendering algorithm, $\Xi(\theta_N)$ is simply a look-up table of values derived from measured zero bistatic BRDF scans.

This discussion applies when the first-surface of the material is relatively smooth such that only a single light ray bounce is valid (which is usually the case for many materials). If, however, the first-surface is very rough such that multiple bounces occur, or the material is a semi-transparent dielectric paint, then a depolarized reflection process occurs too. In this case Equation 3.28 does not correctly give the tilt distribution function $\Xi(\theta_N)$. In Section 5 we will address in detail how to properly extract the tilt distribution function from the measured data.

Notice that $\Xi(\theta_N)$ is a purely *geometric* tilt distribution function. For surfaces that are reasonably smooth, we should be able to integrate over all the micro-facet areas, as projected down to the flat material surface plane, and get unity:

$$\iint_{hemisphere} \Xi(\theta) \cdot \cos(\theta) \cdot d\Omega = 2\pi \cdot \int_0^{\pi/2} \Xi(\theta) \cdot \cos(\theta) \cdot \sin(\theta) \cdot d\theta \approx 1 \tag{3.29}$$

Of course, as the surface becomes rougher, then this normalization might begin to break down because $\Xi(\theta_N)$ can probably no longer be properly measured due to shadow/masking effects. Extremely rough surface finishes, for which the surface is not a simple set of tilted facets, should certainly not follow the normalization of Equation 3.29. However, this is generally acceptable as long as the normalization of Equation 2.3 is satisfied. In general, and except for extremely rough surfaces, Equation 3.29 should hold up.

As we will present later in Section 5, we do not actually derive the tilt distribution function $\Xi(\theta_N)$ directly. Instead, because we do not explicitly know the indices of refraction, we must solve for the product of $\Xi(\theta_N)$ and the normal incidence Fresnel reflectance:

$$\Xi(\theta_N) \cdot R(0) = 4 \cdot \rho'_{mono}(\theta_N) \cdot \cos^2(\theta_N) \quad (sr^{-1}) \tag{3.30}$$

If we substitute Equation 3.30 into Equation 3.29, we get:

$$R(0) \approx 2\pi \cdot \int_0^{\pi/2} 4 \cdot \rho'_{mono}(\theta_N) \cdot \cos^3(\theta) \cdot \sin(\theta) \cdot d\theta \tag{3.31}$$

Here again, this is only as good as the normalization in Equation 3.29.

Before we leave this discussion, we need to finalize our functional form for the specular BRDF. We will need to modify the form of Equation 3.24 to include the normal incidence Fresnel reflectance into the tilt distribution function as:

$$\rho' = \frac{R_{XX}(n_1, \kappa_1, \beta)}{R(n_1, \kappa_1, \beta = 0)} \cdot \left[\frac{R(n_2, \kappa_2, \beta = 0) \cdot \Xi(\theta_N)}{4} \right] \cdot \frac{1}{\cos(\theta_i) \cdot \cos(\theta_r)} \quad (\text{sr}^{-1}) \qquad (3.32)$$

While one expects the normal incidence reflectance $R(0)$ to be the same in the numerator and denominator, this is not a requirement. We emphasized this by the subscripts in Equation 3.32 for the complex indices. The effective reflectivity in the BRDF is contained in the middle term, commonly called the bi_factor. In the materials database file (i.e., MATTER.DAT), the tabulated data has the keyword *BISTATIC*. It is the tabulated tilt distribution function essentially scaled by a reflectivity constant. The indices for the Fresnel reflectance in the bi_factor will never need to be directly known.

The leading Fresnel polarized reflectance function is now a *normalized* function. Figure 3.10
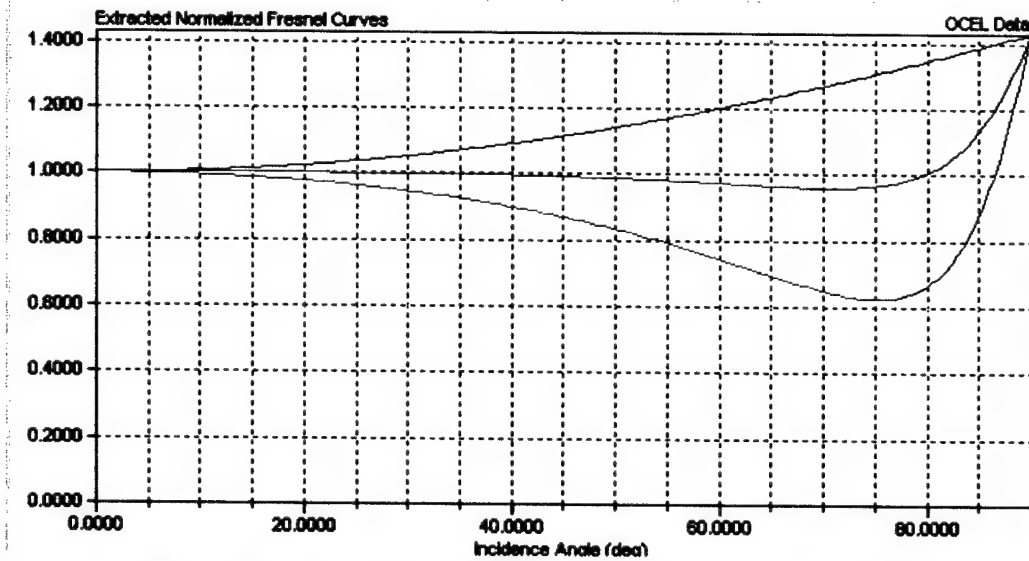
Figure 3.9. Normalized Fresnel Curves for n=1.5 and κ=3.7

shows typical normalized Fresnel curves. The important things to understand are these. Out to significant angles (80 degrees in this example), there is very little polarization effect between the two reflected states. All the interesting action occurs at the larger angles. The relative depth of the Brewster dip (i.e., the degree of polarization) and the ratio of the normal incidence to the grazing incidence reflectance are the most important features. Metals should generally have minimal reflectance ratios, while dielectrics should be much greater. We saw in Figures 3.8 and 3.9 that for typical values of the indices of refraction, these features really change very little. This is to our benefit, since extracting accurate values for the indices is difficult. So errors in our estimates will minimal effect on the final BRDF.

3.4 Shadow-Masking Artifacts

When, for rough surfaces, either the incident light LOS or the viewer LOS gets nearer to the grazing angles (i.e., closer to the material surface), the tilt distribution function $\Xi(\theta_N)$ may no longer fairly represent the true tilt distribution. Figure 3.11 demonstrates the effects of shadowing and masking for a greatly magnified surface.

On the left of Figure 3.11 the incident light casts a shadow on both of the facets that form the groove. This is effectively an area no longer exposed to the incident beam. For more normal incidence conditions these same facets would be illuminated. Thus, the $\Xi(\theta_N)$ distribution has

Shadowed regions   Masked regions
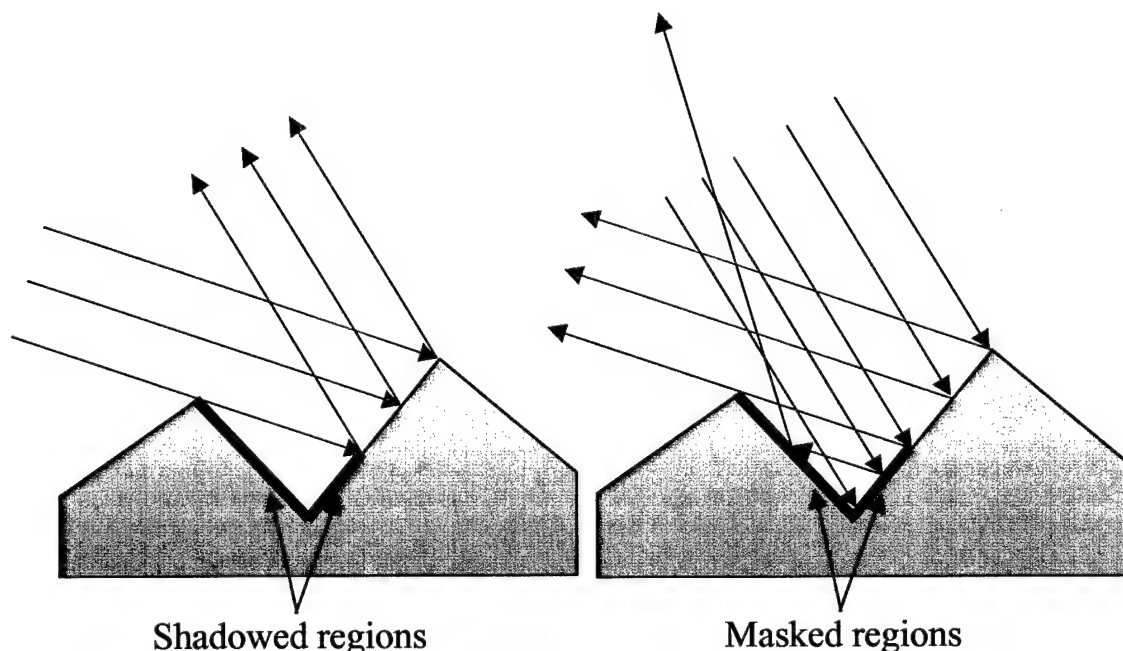
Figure 3.10. Shadow/Masking Examples for Highly Magnified Micro-facets

changed. The opposite can be true, as shown on the right of Figure 3.11. Here some of the reflected light is masked by the adjacent facet and redirected somewhere else. Again, the $\Xi(\theta_N)$ distribution has changed. The shadow/masking effect is two fold. First, the effective area for reflection is reduced as facets get shadowed or masked from the beam; this reduces the intensity of the scattered BRDF. Second, more diffuse scatter might occur.

The exact nature of the shadow/masking effects depend on the roughness statistics. ERIM added an empirical correction factor to the first-surface BRDF to try to account for the shadow/masking effects in the form (the more complicated form stated for completeness here):

$$S_o = \frac{1 + \dfrac{\theta_N}{\Omega} \cdot e^{-(2\beta / \tau)}}{1 + \dfrac{\theta_N}{\Omega}} \cdot \frac{1}{1 + \dfrac{\phi_n}{\Omega} \cdot \dfrac{\theta_i}{\Omega}} \qquad (3.33)$$

where Ω and τ are measured constants, that are functions of the surface roughness, θ_N is the usual angle the bi-section vector makes with the surface normal, β is the angle between the incident light and the bi-section vector, θ_i is the light incident angle, and ϕ_n is a derived geometrical angle. Estimating the angle ϕ_n starts by defining the direction of the specular ray $\hat{S}_{spec}$:

$$\hat{S}_{spec} = \hat{S}_i - 2(\hat{S}_i \circ \hat{N})\hat{N} \qquad (3.34)$$

Then by defining a new perpendicular direction $\hat{P}$:

$$\hat{P} = \hat{S}_{spec} \times \hat{H} \qquad (3.35)$$

where $\hat{H}$ is the bi-section vector. Form the final vector of the triad, $\hat{Q}$:

$$\hat{Q} = \hat{P} \times \hat{S}_{spec} \qquad (3.36)$$

Now, take the dot product of the observer LOS ray, $\hat{V}_r$, with this last vector:

$$\begin{aligned} \phi_n &= \frac{\pi}{2} - \cos^{-1}(-\hat{V}_r \cdot \hat{Q}) & \hat{V}_r \cdot \hat{Q} < 0 \\ \phi_n &= 0 & \hat{V}_r \cdot \hat{Q} \geq 0 \end{aligned} \qquad (3.37)$$

This seems too complicated for the minimal value returned by the calculations. We will omit the second ratio in Equation 3.33 and use just the following for the shadow/masking factor:

$$S_o = \frac{1 + \dfrac{\theta_N}{\Omega} \cdot e^{-2\beta / \tau}}{1 + \dfrac{\theta_N}{\Omega}} \qquad (3.38)$$
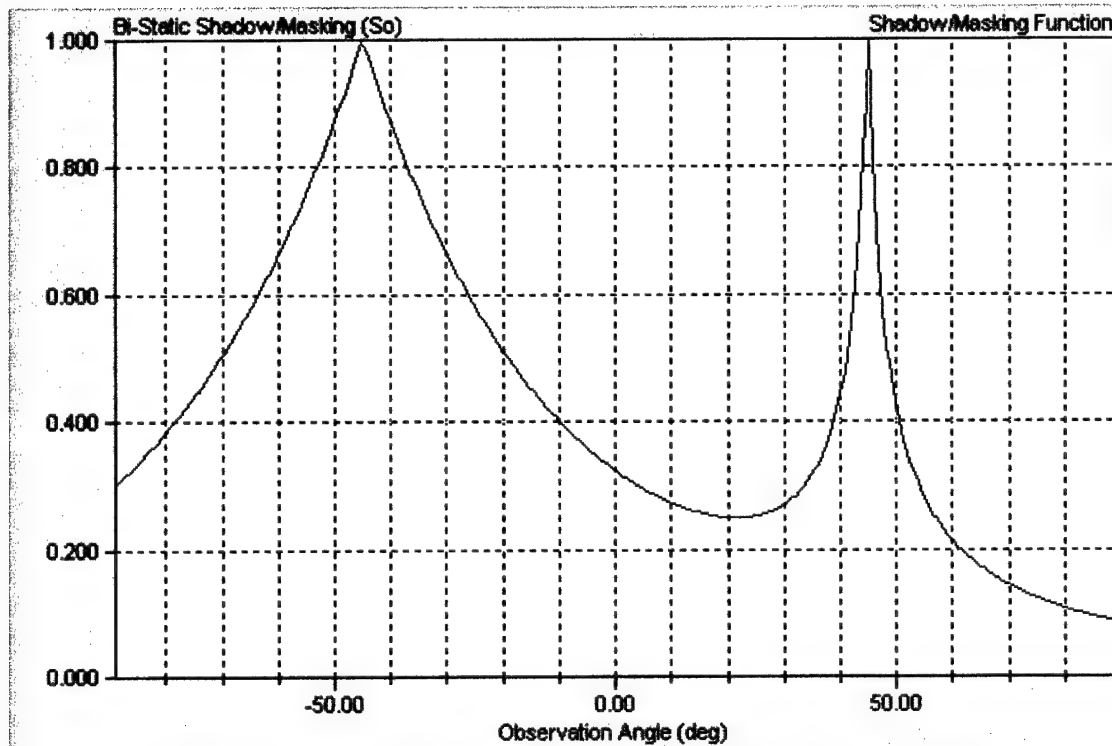
Figure 3.11. S_o *Curve for* $\Omega = 1.56$ *Degrees and* $\tau = 35$ *Degrees*

When Ω is large (i.e., $\Omega \gg \theta_N$), the two $\dfrac{\theta_N}{\Omega}$ terms vanish and S_o goes to unity, and hence no attenuation to the BRDF. If θ_N is zero, then again the $\dfrac{\theta_N}{\Omega}$ terms vanish and S_o goes to unity. If $\beta = 0$ (i.e., monostatic illumination), or τ is large compared to β, then the numerator and denominator in Equation 3.38 are equal, and again S_o goes to unity. Only when the two (Ω, τ) parameters are relatively small, the illumination is bistatic, and the observer is not along the specular direction, will S_o not be equal to unity, and the BRDF is then attenuated. Figure 3.12 plots the in-plane S_o curve for a bistatic BRDF at 45 degrees ($\Omega = 1.56$ degrees and $\tau = 35$ degrees).

Notice that the function peaks to 1 at both the forward specular direction (i.e., +45 degrees) and at the retro-reflection direction (i.e., the monostatic direction at –45 degrees). Clearly the shadow/masking function tends to depress the BRDF values at the skirts only. When the bistatic angles are small (i.e., near normal incidence), this double peak does couple into the otherwise monotonic BRDF.

Equation 3.32 is now modified to include the shadow/masking effects:

$$\rho'_{XX}(\theta_i, \theta_r, \beta, \theta_N) = \frac{R_{XX}(\beta)}{R(0)} \cdot \frac{bi\_factor(\theta_N)}{\cos(\theta_i) \cdot \cos(\theta_r)} \cdot S_o(\theta_N, \beta) \qquad (\text{sr}^{-1}) \qquad (3.39)$$

This is the complete polarized first-surface BRDF. The choice of the Fresnel reflectance depends on the incident and sensed polarization state.

3.5 The Unpolarized Diffuse BRDF

Light that is diffusely scattered at either the first-surface or from within the volumetric region of the material must be modeled as a second and separate depolarized BRDF. Many materials exhibit a diffuse scatter that follows the classical Lambert's law, where the apparent reflected radiance is equal in all directions, and the scatter follows a cosine law. The BRDF is therefore not a function of angle in this case:

$$\rho'_{Lambertian}(\lambda) = R_{diffuse}(\lambda) \cdot \frac{1}{\pi} = R_x(\lambda) \qquad (sr^{-1}) \qquad (3.40)$$

where $R_{diffuse}$ is some effective diffuse reflectivity for the material. The inverse π comes from the normalization given in Equation 2.3:

$$R_{diffuse}(\lambda) = 2\pi \cdot \int_0^{\pi/2} R_x(\lambda) \cdot \cos(\theta) \cdot \sin(\theta) \cdot d\theta = \pi \cdot R_x(\lambda) \qquad (3.41)$$

A Lambertian diffuse scatter can come from either the first-surface (i.e., a very rough finish), or the volumetric pigment particles in paint. While $R_{diffuse}$ is probably physically intuitive, we will refer to the Lambertian diffuse reflectivity as R_x, since this is a parameter found in the material properties database files.

Sometimes the diffuse scatter displays a slight non-Lambertian variation with the angle of incidence or observation. This arises from different rays penetrating more or less into the pigmented volumetric region of a paint (or plastic).

Consider light penetrating a semi-transmissive material layer where light energy is scattered out of the incoming ray linearly with distance. As the ray travels deeper and deeper, its intensity falls off as an exponential function. Figure 3.13 shows the basic scatter geometry for a material that partially transmits and scatters light. The derivation of the diffuse BRDF follows standard single scattering concepts. Assume that a slab of material of thickness dz scatters light with a phase function $\sigma(\beta)$, with units of inverse length. The angle β is taken relative to the incident shot-line of the laser light, and the phase function is assumed azimuthally symmetric. If the phase function is spherically symmetric (i.e., scatters uniformly into 4π), then the phase function would be:

$$\sigma(\beta) = \frac{\sigma_o}{4\pi} \qquad (1/m\text{-}sr) \qquad (3.42)$$

where σ_o would be the fraction of incident light scattered (power removed from the incident beam) per unit length into all directions, i.e., the total scattering cross-section. If the irradiance at the front surface is I_o, then, after traveling a distance of w, the residual intensity is:

$$I(w) = I_o \cdot e^{-\sigma_{total} \cdot w} \qquad \text{(watts/m}^2) \qquad (3.43)$$

This holds whether the light is traveling into or out of the material volume. The loss of light is
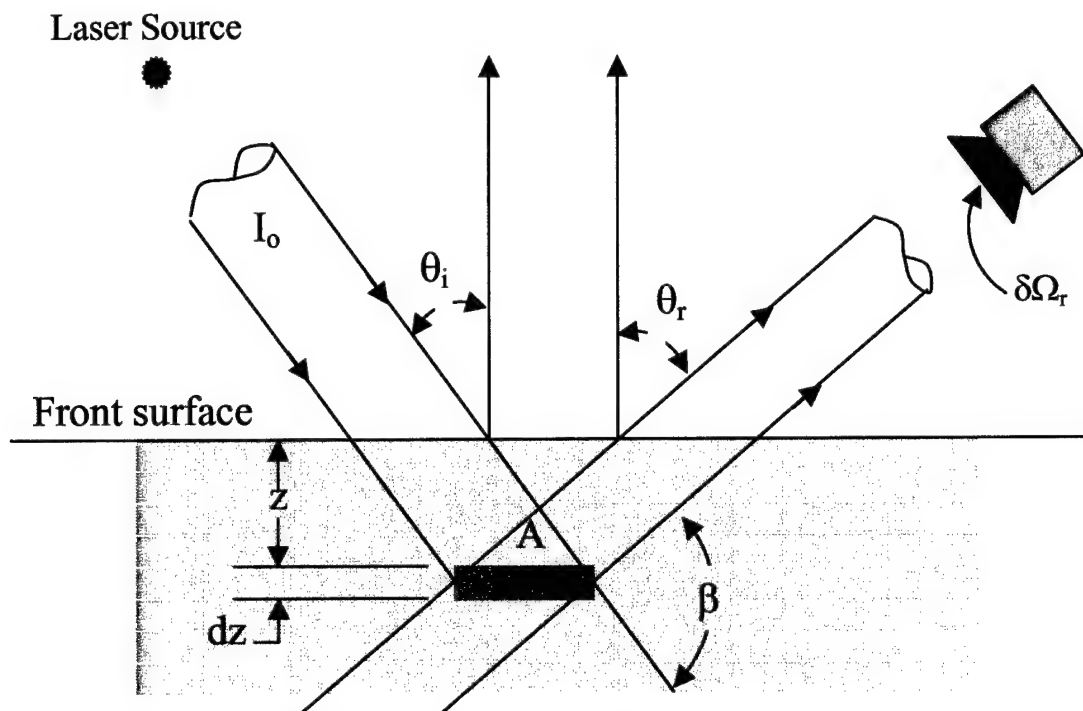
Figure 3.12. Volumetric Reflection Geometry

from both scattering and absorption, thus, σ_t is the total cross-section

$$\sigma_{total} = \sigma_{scattering} + \sigma_{absorption} \qquad \text{(1/m)} \qquad (3.44)$$

We can work backwards from the sensor point of view. The sensor sees light being scattered from many differential slabs of dz vertical thickness, each buried at a different depth z. Assume the radiance of the slab shown in Figure 3.13 is $J(z)$:

$$dP_r = J(z) \cdot A \cdot \cos(\theta_r) \cdot \delta\Omega_r \cdot e^{-\sigma_{total} \cdot z / \cos(\theta_r)} \qquad (3.45)$$

The irradiance at the same slab is:

$$I(z) = I_o \cdot e^{-\sigma_{total} \cdot z / \cos(\theta_i)} \qquad (3.46)$$

The power scattered out of the beam, going across the slab at depth z into the direction of the receiver is:

$$dP_\Omega(\beta) = I(z) \cdot A \cdot \cos(\theta_i) \cdot \sigma(\beta) \cdot \frac{dz}{\cos(\theta_i)} \cdot \delta\Omega_r \qquad (3.47)$$

The apparent radiance of the slab in the absence of the intervening material would be:

$$J(z) = \frac{dP_\Omega}{A \cdot \cos(\theta_r) \cdot \delta\Omega_r} = I(z) \cdot \sigma(\beta) \cdot \frac{dz}{\cos(\theta_r)} \qquad (3.48)$$

Now, putting equations 3.45, 3.46, and 3.48 together to get the power at the receiver aperture:

$$dP_r = I_0 \cdot e^{-\sigma_{total} \cdot z / \cos(\theta_i)} \cdot \sigma(\beta) \cdot \frac{dz}{\cos(\theta_r)} \cdot A \cdot \cos(\theta_r) \cdot \delta\Omega_r \cdot e^{-\sigma_{total} \cdot z / \cos(\theta_r)} \qquad (3.49)$$

The total power at the receiver aperture then is the integral over the depth z:

$$P_r = I_0 \cdot \sigma(\beta) \cdot A \cdot \frac{\cos(\theta_r)}{\cos(\theta_i)} \cdot \delta\Omega_r \int_0^\infty e^{-\sigma_{total} \cdot z \cdot \frac{\cos(\theta_i) + \cos(\theta_r)}{\cos(\theta_i) \cdot \cos(\theta_r)}} \cdot dz \qquad (3.50)$$

Evaluating the integral, we get:

$$P_r = I_0 \cdot \frac{\sigma(\beta)}{\sigma_{total}} \cdot A \cdot \delta\Omega_r \cdot \frac{\cos(\theta_i) \cdot \cos(\theta_r)}{\cos(\theta_i) + \cos(\theta_r)} \qquad (3.51)$$

Casting this into Equation 2.1 for the BRDF:

$$\rho'(\theta_i, \theta_r, \beta) = \frac{f(\beta)}{\cos(\theta_i) + \cos(\theta_r)} \qquad (\text{sr}^{-1}) \qquad (3.52)$$

where $f(\beta)$ is some function of the phase angle β. This is only an approximate treatment, since multiple scattering has not been accounted for at all. We also assume that the pigment is opaque enough to attenuate the beam within a very short distance of the surface, such that the integral to infinity is justified for even thin paint layers.

For practical usage we really do not want to model much more than a possible spherically uniform phase function. The common notation for the angularly-dependent diffuse BRDF is:

$$\rho'_{non-lambertian}(\theta_i, \theta_r) = 2 \frac{R_{hov}}{\cos(\theta_i) + \cos(\theta_r)} \qquad (\text{sr}^{-1}) \qquad (3.53)$$

where a single constant R_{hov} (sometimes notated R_v) is used to scale the strength of this diffuse functional term. As we will see when extracting the diffuse BRDF parameters, the coefficient R_{hov} is fit to the measured BRDF data. Even for metals, where there is no volumetric region to justify the above development of this functional form, we will use this non-Lambertian diffuse function.

The total diffuse depolarized BRDF scatter is given by:

$$\rho' \ (\theta_i, \theta_r, \beta, \theta_N)_{diffuse} = R_x + 2\frac{R_{hov}}{\cos(\theta_i) + \cos(\theta_r)} \quad (\text{sr}^{-1}) \tag{3.54}$$

A factor of 1/2 will be needed to account for only half the power going into one linear polarization state, if the receiver has such a polarizer. There are other effects that have been absorbed into these terms. For instance, the fact that a typical air-dielectric Fresnel interface reflects about 4% has implicitly been absorbed into the R_x and R_{hov} coefficients.

3.6 Summary of Maxwell-Beard BRDF Equations

At this point we need to summarize the BRDF equations in their final form. We took time to develop the underlying physics and mathematics of the equations to help the user better understand how the functional forms arise. The net BRDF will always be a simple sum of the polarized specular and depolarized diffuse BRDF terms. The reflected intensities depend on the incident polarization state and the receiver polarization sensitivity. The six obvious cases are:

Incident P:Receiver P

$$\rho = \frac{R_{PP}(\beta)}{R(0)} \cdot \frac{bi\_factor(\theta_N)}{\cos(\theta_i) \cdot \cos(\theta_r)} \cdot S_o(\theta_N, \beta) + \frac{1}{2}\left[R_x + 2\frac{R_{hov}}{\cos(\theta_i) + \cos(\theta_r)}\right] \quad (\text{sr}^{-1}) \tag{3.55}$$

Incident P:Receiver S

$$\rho' = \frac{1}{2}\left[R_x + 2\frac{R_{hov}}{\cos(\theta_i) + \cos(\theta_r)}\right] \quad (\text{sr}^{-1}) \tag{3.56}$$

Incident P:Receiver none

$$\rho' = \frac{R_{PP}(\beta)}{R(0)} \cdot \frac{bi\_factor(\theta_N)}{\cos(\theta_i) \cdot \cos(\theta_r)} \cdot S_o(\theta_N, \beta) + \left[R_x + 2\frac{R_{hov}}{\cos(\theta_i) + \cos(\theta_r)}\right] \quad (\text{sr}^{-1}) \tag{3.57}$$

Incident S:Receiver S

$$\rho' = \frac{R_{SS}(\beta)}{R(0)} \cdot \frac{bi\_factor(\theta_N)}{\cos(\theta_i) \cdot \cos(\theta_r)} \cdot S_o(\theta_N, \beta) + \frac{1}{2}\left[R_x + 2\frac{R_{hov}}{\cos(\theta_i) + \cos(\theta_r)}\right] \quad (\text{sr}^{-1}) \tag{3.58}$$

Incident S:Receiver P

$$\rho' = \frac{1}{2}\left[R_x + 2\frac{R_{hov}}{\cos(\theta_i) + \cos(\theta_r)}\right] \quad (\text{sr}^{-1}) \tag{3.59}$$

Incident S:Receiver none

$$\rho' = \frac{R_{SS}(\beta)}{R(0)} \cdot \frac{bi\_factor(\theta_N)}{\cos(\theta_i) \cdot \cos(\theta_r)} \cdot S_o(\theta_N, \beta) + \left[R_x + 2\frac{R_{hov}}{\cos(\theta_i) + \cos(\theta_r)}\right] \quad (\text{sr}^{-1}) \tag{3.60}$$

and when the incident polarization is either unpolarized or circular, and receiver none:

$$\rho' = \frac{R_{un}(\beta)}{R(0)} \cdot \frac{bi\_factor(\theta_N)}{\cos(\theta_i) \cdot \cos(\theta_r)} \cdot S_o(\theta_N, \beta) + \left[R_x + 2 \frac{R_{hov}}{\cos(\theta_i) + \cos(\theta_r)} \right] \quad (\text{sr}^{-1}) \quad (3.61)$$

where the unpolarized mean Fresnel reflectance (Equation 3.12) is used in the specular BRDF.

This is clearly not a full treatment of the polarization problem. In the LRST application, the receiver will most likely have no polarization selectivity. Whether the receiver is a biological eye or an electro-optical imaging sensor, both polarization components will be received. The incident polarization state will more than likely be elliptically polarized. For reflection geometries where the included angle between source and observer is less than 45 degrees, the polarization effects are minimal. For the more grazing geometries, the S reflectance will be higher than the P, and the partition of energy into each of these directions might be more important to consider. At the extreme grazing geometries, both reflectances go up dramatically, and again the polarization preference is less critical.

The issue then is whether to worry about polarization effects for those reflection angles for which the degree of polarization is greatest. If the laser polarization is either depolarized or circularly polarized, then using the mean unpolarized Fresnel reflectance is accurate. If the laser polarization is elliptical, then using the mean unpolarized Fresnel reflectance is probably still adequate. If the laser polarization is strictly linear, then there could potentially be a significant reflectance difference for some materials; the error occurs for mid-angles (e.g., 45–85 degrees), and is the difference between the unpolarized mean Fresnel curve and the S and P curves (cf. Figure 3.6). For a linear polarized axis at 45 degrees to the surface normal, the equations are implemented in the code will predict values that are low for the S reflection, and high for the P reflection. The materials that have significant first-surface specular reflections are metals. The interesting thing is that most reflective metals have Fresnel curves that do not separate very much because the S and P reflectances are already fairly high. The approximation in using the unpolarized mean Fresnel reflectance for all cases should be a good compromise.

There are three approaches to capturing the polarization effects. First, we could model the polarization effects in detail. This would involve accurately modeling the incident polarization state of the laser (which would be determined by ABL performance tests, for example). Either a Stokes vector or a coherency matrix would represent this state. Next, at each reflection location on the target surface, we would need to rotate the frame of the incident polarization state vector into the local frame of the S and P directions. This then gives us the partition of power in the two orthogonal polarization states *(S* and *P)* such that we can separately weight the respective polarized BRDF from Equations 3.57 and 3.60. The downside to this approach is the rather expensive computational cost of always solving for the S and weighting.

The second approach involves no additional computation, and is really the most conservative. We can always use just the S reflectance curve (i.e., use Equation 3.60) and accept the error for always overestimating the P reflectance.

The third approach also involves virtually no additional computational cost and should give higher-fidelity results. Use the unpolarized or mean Fresnel reflectance value instead of the S

reflectance. On average this should balance the errors in overestimating the P and under-estimating the S reflectances. This is the approach currently used in LRST.

4.0 SIMPLE TWO-PARAMETER BRDF MODELS

In addition to the ERIM BRDF model, we currently use two other simplified models that are procedural and require only two parameters to completely specify the bistatic BRDF functional form. Having a suitable zero-order BRDF model is important for several reasons. We are often faced with having no measured BRDF data for some materials; this is especially true for foreign technology items. Sometimes we want to do parametric studies to assess the effect of a BRDF on a particular signature. It is useful to have a BRDF functional form that lends itself to analytic manipulation.

The first model is a modified Phong BRDF model (Reference 3) commonly found in the computer graphics literature. Phong basically models the specular effects by a simple cosine raised to some power, which is computationally cheap because the cosine is readily available from routine dot products. The modification we made was to bend this model to look very much like the Maxwell-Beard model, in which the cosine factor substitutes for the bi_factor. We ensure that the BRDF complies with the standard hemispherical reflectivity normalization requirement.

4.1 The Phong BRDF Model

The Phong model is a simple two-parameter empirical model that attempts to describe the BRDF as having a diffuse (i.e., an asymptotic Lambertian) component, and a shiny component around the specular reflection direction.

The specular contribution to the BRDF is responsible for giving smooth surfaces their shiny look. The primary difference between BRDF models usually centers on the detailed functional form for the specular component. The Phong model attempts to model the specular falloff by a cosine raised to some power. The larger the exponent, the more specular the BRDF appears.

The Phong formulation starts by constructing a bisection vector $\hat{H}$ between the incident light direction and the observer direction (cf. Equation 3.25); then the angle between $\hat{H}$ and the surface normal is θ_N, the angle used as the argument of the cosine. The Phong BRDF assumes that the bi_factor (i.e., the tilt distribution function) is this cosine power function:

$$\rho'_{XX}(\theta_i,\theta_r,\beta,\theta_N)_{specular} = \frac{R_{XX}(n,\kappa,\beta)}{R(0)} \cdot M \cdot \cos^n(\theta_N) \cdot \frac{1}{\cos(\theta_i) \cdot \cos(\theta_r)} \cdot S_o \qquad (\text{sr}^{-1}) \qquad (4.1)$$

where M is a normalization constant (it conserves the total specular reflectivity), and $M \cdot \cos^n(\theta_N)$ is the effective tilt distribution function. The leading function is the normalized Fresnel reflectivity. The trailing function S_o is the shadow/masking term that is everywhere defaulted to 1. We do not implement S_o because the change in results by including it would be well within the current error range of the bi_factor.

For small values of n, the specular nature of the BRDF is not very pronounced. Figure 4.1 plots a few examples of the specular BRDF function for varying values of n when the light is incident vertically.

The upturn of the BRDF at large angles is typical of BRDF models, and results from the $\cos(\theta_r)$ in the denominator. This is especially true when the bi_factor predominantly scatters into large angles (i.e., small values of n). The physical quantity of interest, however, is "intensity," not the BRDF. The BRDF turn-up is always balanced by a cosine in the numerator that prevents unbounded intensities at grazing angles.

As an approximation, the specular value drops to half the peak when the angle is

$$\theta_{HWHM} = 2 \cdot \cos^{-1}\left[10^{\frac{-0.30103}{n}}\right]$$

(rad)
(4.2)

For example, let us take $n = 100$. The half intensity – half angular width would be 13.47 degrees, which agrees with Figure 4.1.
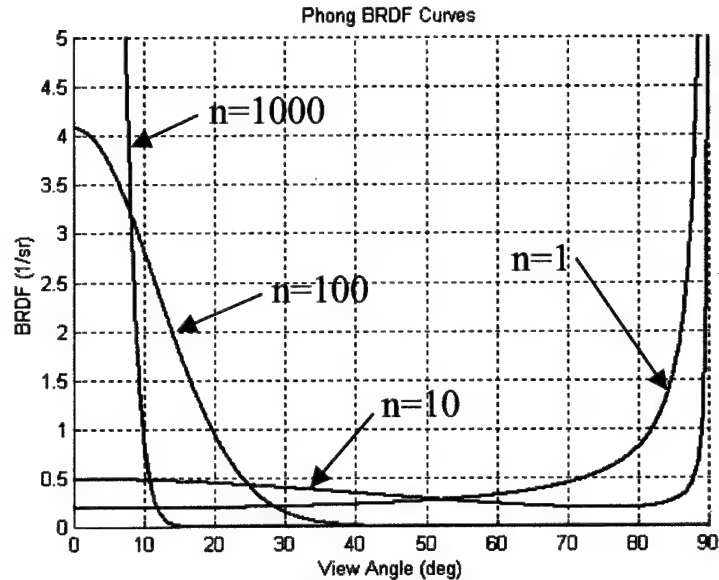
Figure 4.1. Phong Specular BRDF for: n=1000,100,10, and 1, Assuming Unity Reflectivity

The Phong model also supports a diffuse BRDF component, which is *always* Lambertian:

$$\rho'_{Lambertian} = R_x \qquad (\text{sr}^{-1}) \qquad (4.3)$$

The diffuse BRDF parameter R_x is not directly supplied by the materials database - rather, only the relative fraction of first-surface diffuse scatter is specified. The volumetric diffuse (if the material is a paint) is inferred later in Section 6 during the normalization.

4.2   The Gaussian BRDF model

The Gaussian BRDF is probably the most suitable, best-behaved functional form we have for comparing numerical predictions with analytic formulas. It normalizes very well at all angles of incidence (as long as the surface is relatively shiny). However, notwithstanding its convenient analytical properties, we should expect only qualitative agreement of this model with nature.

The Gaussian formulation also starts by constructing a bisection vector $\hat{H}$ between the incident light direction and the observer direction. The angle between $\hat{H}$ and the surface normal is θ_N, the angle used in the exponential argument. The specular BRDF is now given by:

$$\rho'_{XX}(\theta_i, \theta_r, \beta, \theta_N,)_{specular} = \frac{R_{XX}(n, \kappa, \beta)}{R(0)} \cdot \frac{M \cdot e^{-2 \cdot \theta_N^2 / \sigma^2}}{2 \cdot \pi \cdot \sigma^2} \cdot \frac{1}{\cos(\theta_i) \cdot \cos(\theta_r)} \cdot S_o \qquad (sr^{-1}) \qquad (4.4)$$

where M is a normalization constant, and $\dfrac{M \cdot e^{-2 \cdot \theta_N^2 / \sigma^2}}{2 \cdot \pi \cdot \sigma^2}$ is the effective tilt distribution function.
The leading function is the normalized Fresnel reflectivity. The trailing function S_o is the shadow/masking term that is defaulted to 1 everywhere. The argument to the exponential contains σ, which controls the angular width of the specular lobe, and is specified in units of radians.

Figure 4.2 shows examples of the Gaussian BRDF shape. The BRDF falls to $e^{-2} = 13.5\%$ of the peak when $2\sigma = 2\theta_N = \theta_{e-2}$. For example, the second curve with $\sigma = 10°$ reaches the e^{-2} point at exactly 20 degrees.

The Gaussian model must support a diffuse BRDF component, which is again *always* Lambertian:

$$\rho'_{Lambertian} = R_x \qquad (sr^{-1}) \qquad (4.5)$$

The diffuse BRDF parameter R_x is not directly supplied by the materials database; rather, only the relative fraction of first-surface diffuse scatter is specified. The volumetric diffuse parameter (if the material is a paint) is inferred later during the normalization.
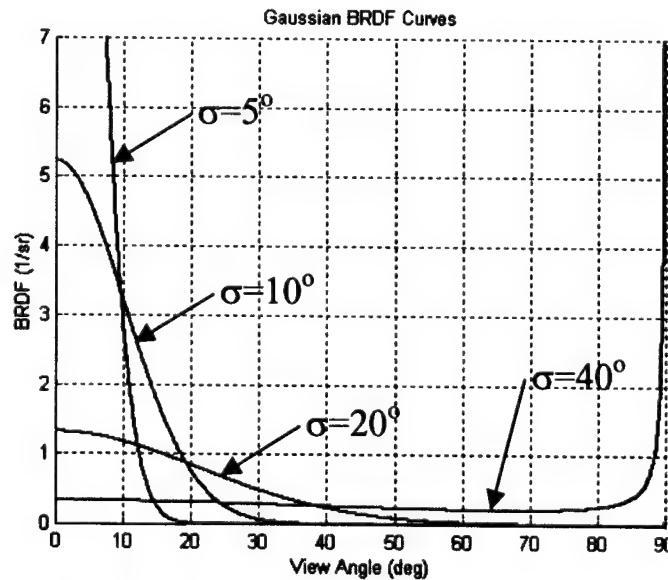

Figure 4.2. Gaussian BRDF Curves for 5-, 10-, 20-, and 40-degree σ Parameters

5.0   Maxwell-Beard BRDF Parameter Extraction Algorithms

In this section we cover the necessary algorithms to extract the Maxwell-Beard BRDF parameter set from measured Optical Component Evaluation Laboratory (OCEL) BRDF data. To characterize the BRDF of a material, there is one fundamental set and two optional sets of measurements one needs to make in the laboratory. From these one constructs parametric fits of the measured data to extract the optical material properties used in the BRDF simulation models.

The first (mandatory) set of critical measurements involves making four classic in-plane BRDF mono-static (MSA) scans. A linearly polarized laser illuminates the material surface, with its optical axis along either the S or the P direction. A receiving sensor, with a linear polarizer aligned with either the S or the P direction, detects the scattered radiation. For this measurement, one tries to collocate the laser and sensor along the same optical LOS and scan them in the plane of incidence over a full 180 degrees (grazing incidence to normal, and then back to grazing incidence). The four useful mono-static measurement combinations of source/receiver polarization are $BRDF_{ss}$, $BRDF_{sp}$, $BRDF_{pp}$, and $BRDF_{ps}$, as a function of incidence angle (angles are always measured down from the surface normal). Actually, the second two scans are slightly redundant with the first two. In principle one could do the extraction with two crossed scans, but it is better to make all four and average the scans to reduce the effects of measurement noise and material anisotropy. One cannot collocate the laser source and sensor exactly along the same LOS because of their physical size without resorting to additional expensive optical hardware to beam split and mitigate stray light. In practice, therefore, there is always a small bistatic angle between the two optical lines of sight. We call these scans *zero-bistatic* or *quasi-monostatic*. Figure 5.1 demonstrates the geometrical layout used for the measurements. This set of measurements will be used to extract the surface roughness tilt distribution, the diffuse reflection parameters, and the initial estimates of the complex indices of refraction.
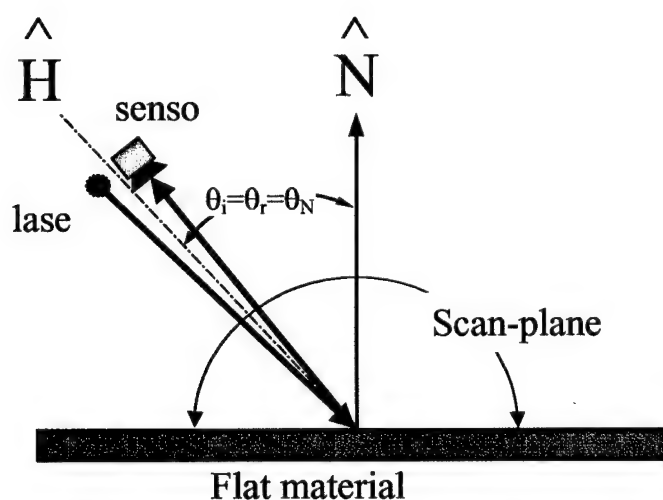

Figure 5.1. In-plane, Zero-bistatic Scan Geometry

The second BRDF measurement is a scissor-type bistatic intensity (RVI) scan in the plane of incidence. The laser is scanned backward with an angle $-\theta$, while the receiver is scanned forward at an angle $+\theta$ pointing along the specular direction. In principle, the sensor measures the peak specular intensity as a function of the angle θ. The intent here is to map out the effective Fresnel reflectance. In particular we are interested in the Brewster angle and depth of modulation for the P reflectance relative to the normal incidence value. We therefore measure $BRDF_{PP}(\theta)$. By doing a least-squares fit we can extract a complex index pair (n, κ) that approximately models these features.

The third measurement takes in-plane bistatic scans (BSA) at various incidence angles. These are used to infer the shadow/masking parameters by doing a least-squares fit to the BRDF at angles away from the specular direction. These scans are also important for comparing the simulated BRDF against measured bistatic data.

The fourth critical measurement directly captures the full hemispherical reflectivity, taken as a function of wavelength if possible. This measurement is independent of all the BRDF measurements. The extracted the BRDF parameters, taken in-plane, could be integrated over a hemisphere to get the directional hemispherical reflectivity (DHR), but only indirectly. The issue with using this technique to *measure* the DHR is that most of the out-of-plane scattered energy is never directly measured. A direct measure of the hemispherical reflectivity using an integrating sphere represents a much more accurate accounting for the total scattered energy. Usually, both methods agree fairly closely, but the direct measurement should be done. For optimum fidelity, a hemispherical reflectivity scan should also be made as a function of wavelength. This color curve is absolutely necessary for signature simulations to extend the BRDF to other wavelengths or wavelength bands. The tilt distribution, or surface roughness, is a geometrical property of surfaces and generally does not change much with wavelength. The BRDF scattering angular distribution tends to be wavelength-independent (out to longer IR wavelengths). The net energy reflected, however, is very wavelength-dependent, and this last measurement establishes the fundamental radiometric energy balance. If one knows the net hemispherical reflectivity as a function of all wavelengths, then one can in principle borrow and renormalize BRDF data measured at a nearby wavelength. In Section 6 we will cover this renormalization process.

In general, we want to populate the MATTER.DAT database with the reflectivity as a function of wavelength (i.e., colors) from the UV to the LWIR. For most of the materials in the current database this has been done. We depend on these color curves exclusively to set the radiometric energy balance for whatever wavelength is being simulated. Thus, if we are simulating multiple laser wavelengths, then we need the measured DHR for each.

Consider the zero-bistatic scan data. From the first-surface we get polarized retro-reflected energy from all the micro-facets that are tilted back at the laser's incident angle. The reflected energy is driven by the normal incidence Fresnel reflectance, and the fractional reflecting micro-facet area, given by the tilt distribution function. There is the potential for a second depolarized reflection via multiple micro-facet bounces if the surface is very rough, as shown in Figure 5.2. The depolarization occurs because the multiple-bounce path is different for each microscopic

light ray. The scatter also tends to go into wide angles. Usually the amount of diffuse depolarized scatter from the first-surface is minimal, perhaps just a few percent of the total.
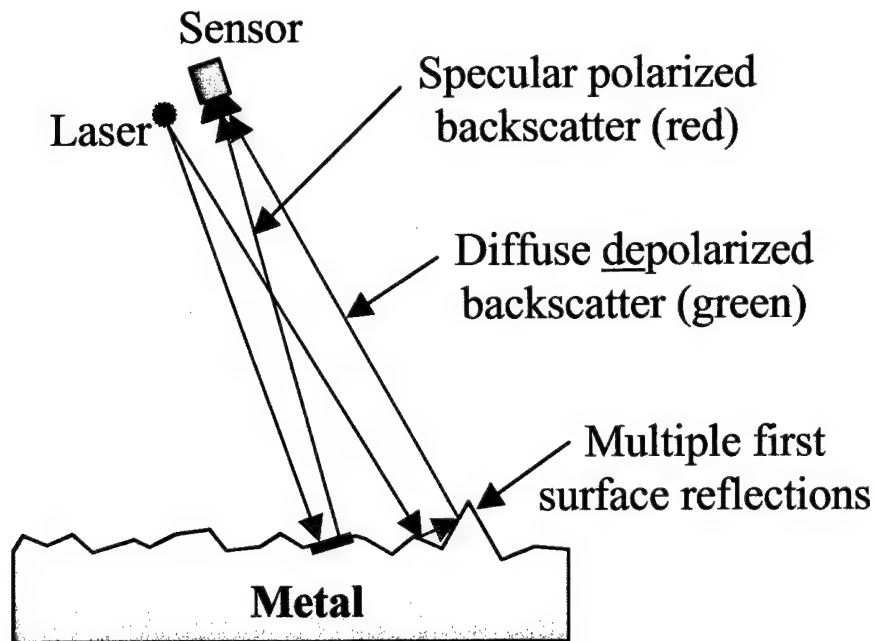
Figure 5.2. Polarized and Depolarized Reflections for the First-surface Reflection for a Very Rough Surface

For dielectric materials, the reflection process includes a volumetric contribution from the pigment particles, if the wavelength is such that the dielectric binder will transmit light into the volumetric region (this is why paints work). Figure 5.3 shows the added scatter from the volumetric region. This contribution is usually the major reflection contributor because the first-surface Fresnel reflection is typically only 4% to10%.
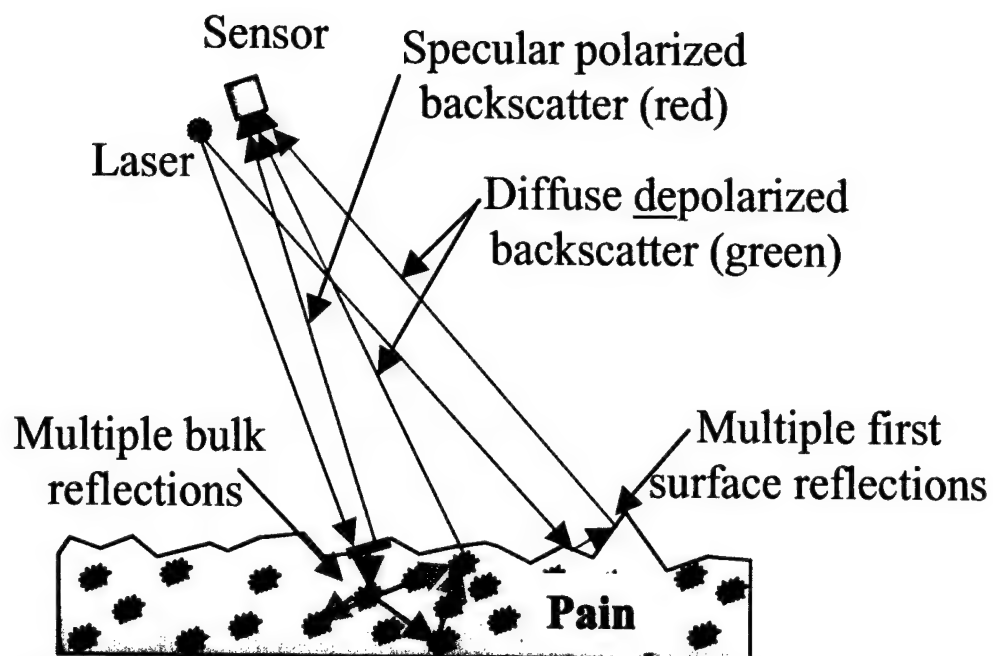
Figure 5.3. Polarized and Depolarized Reflections for a Dielectric Material

There are five quantities given in Table 5.1 that must be inferred from measured data to support the Maxwell-Beard BRDF model.

Table 5.1. Parameters Requiring Extraction for the Maxwell-Beard BRDF Model

Parameter	Extraction Method	Comments
bi_factor(θ_N)	Zero-bistatic scan BRDF less the depolarized diffuse component.	$R(0)$ is measured indirectly and is part of the bi_factor.
R_x	Least-squares fit to depolarized BRDF.	Lambertian uniform fit - must avoid polarized leakage in cross-scan data.
R_{hov}	Least-squares fit to depolarized BRDF.	Non-Lambertian angular dependent fit.
N	Method 1: Integrate the mono-static BRDF data via Equation 3.31, assign one index and solve for the other. Method 2: Use bistatic scissor-scan set and least-squares fit to intensity values. n and κ are fit simultaneously.	The first method relies on Equation 3.29 being valid. The second method requires more measured data and becomes difficult for rough surfaces or surfaces with significant diffuse components of the BRDF.
κ	Same as for $.n$	Same as for n.
τ	Least-squares fit made against bistatic scans at varying incidence angles. Both τ and Ω are fit simultaneously.	Fit only applies to measured BRDF fits at off-specular angles.
Ω	Same as for τ.	Same as for τ.
DHR	Not extracted.	Directly measured using integrating hemisphere.

5.1 Extracting the Bi_factor (Scaled Tilt Distribution) Function

Let us return to Equation 3.55 for the total BRDF scatter when the source and receiver are approximately collocated and we are measuring P to P:

$$\rho'_{PP}(\theta_N)_{mono-static} = \frac{R(0) \cdot \Xi(\theta_N)}{4 \cdot \cos(\theta_N) \cdot \cos(\theta_N)} + \frac{1}{2}\left[R_x + \frac{R_{hov}}{\cos(\theta_N)}\right] \qquad (\text{sr}^{-1}) \qquad (5.1)$$

Because the scatter is in the retro-reflection direction, the leading normalized Fresnel, as well as the trailing shadow/masking values, are both unity. The measured cross-polarized BRDF is:

$$\rho'_{PS}(\theta_N)_{mono-static} = \frac{1}{2}\left[R_x + \frac{R_{hov}}{\cos(\theta_N)} \right] \qquad (\text{sr}^{-1}) \qquad (5.2)$$

Notice that there are no polarization-dependent terms in either equation above. Therefore, the equations would have been the same for the S to S, and S to P polarizations.

Before proceeding, we want to average the data sets to reduce measurement noise in the following way. We average the values at the negative angle with those for the positive angle:

$$\overline{\rho'_{XX}(\theta_N)}_{mono-static} = \frac{\rho'_{XX}(-\theta_N)_{mono-static} + \rho'_{XX}(\theta_N)_{mono-static}}{2} \qquad (\text{sr}^{-1}) \qquad (5.3)$$

Next, we can begin to solve for the bi_factor by taking the difference of Equations 5.1 and 5.2 to get the specular polarized component alone (recall that the depolarized diffuse contributions for P to P and P to S are equal):

$$\Delta\rho'_{specular}(\theta_N) = \rho'_{PP}(\theta_N) - \rho'_{PS}(\theta_N) = \frac{R(0)\cdot\Xi(\theta_N)}{4\cdot\cos(\theta_N)\cdot\cos(\theta_N)} \qquad (\text{sr}^{-1}) \qquad (5.4)$$

We again want to average the two sets of scans, and make sure no differences go negative:

$$\overline{\Delta\rho'_{specular}(\theta_N)} = \frac{1}{2}\cdot\left\{ [\max[0, \rho'_{PP} - \rho'_{PS}] + \max[0, \rho'_{SS} - \rho'_{SP}] \right\} \qquad (\text{sr}^{-1}) \qquad (5.5)$$

If θ_{last} is the last valid measurement angle (less than 90 degrees), then beyond this angle the BRDF is continued by rolling off the last valid measured BRDF as a cosine squared (or some higher power):

$$\rho'_{XX}(\theta > \theta_{last}) = \rho'_{XX}(\theta_{last})\cdot\left[\frac{\cos(\theta)}{\cos(\theta_{last})} \right]^2 \qquad (\text{sr}^{-1}) \qquad (5.6)$$

Solving Equation 5.4 for the bi_factor(θ_N):

$$\text{bi\_factor}(\theta_N) = \overline{\Delta\rho'_{specular}}(\theta_N)\cdot\cos^2(\theta_N) = \frac{R(0)\cdot\Xi(\theta_N)}{4} \qquad (\text{sr}^{-1}) \qquad (5.7)$$

The bi_factor is a tabulated function that is the product of the normal incidence Fresnel reflectivity and the tilt distribution function.

Figure 5.4 shows examples of measured zero bistatic BRDF data for a fairly shiny metal. The diffuse cross-scans both show about a 6% contamination of the depolarized scatter in the center. This is caused by the strong specular cross-polarized peak leaking through the sensor's linear polarizer. When we attempt to extract the diffuse parameters we will need to ignore this erroneous data. The raw data quits around 80 degrees.
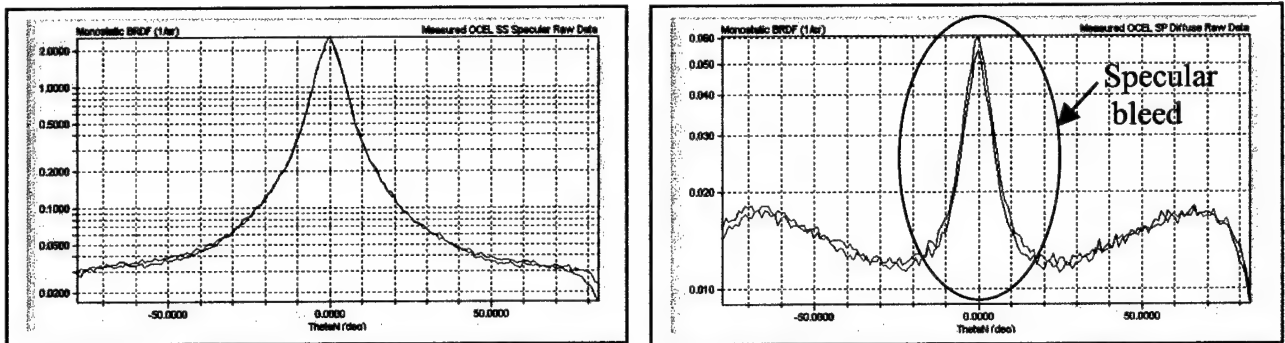
***Figure 5.4. Sample Measured Zero Bistatic BRDF Data; at left are the specular PP and SS
scans; at right are the diffuse PS and SP scans.***

Using Equations 5.3, 5.5, and 5.7, we plot the specular mono-static BRDF curve with the
measured data in Figure 5.5. The agreement is quite good, though neither the indices of refraction
nor the shadow/masking parameters were properly extracted at this point. Most of the critical
BRDF properties *have* been extracted by this point.
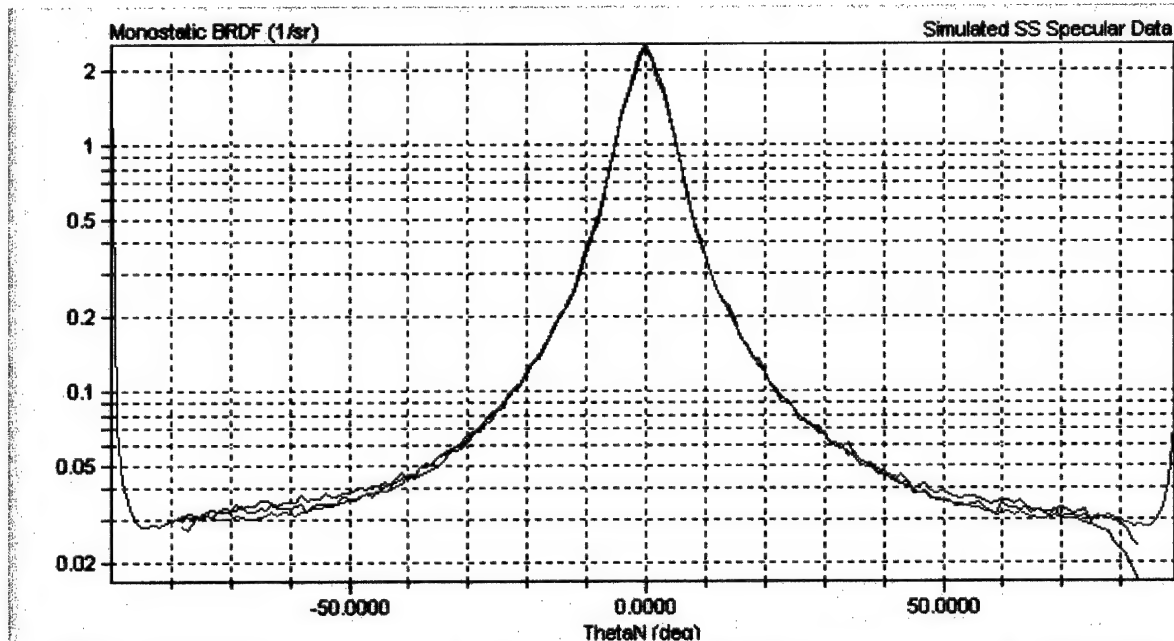
Figure 5.5. Simulated (Red) and Measured (Blue) Specular Monostatic BRDF Curves

There is one pathological bi_factor extraction problem we need to deal with. When the first-
surface is extremely shiny, the specular lobe width can become less than the angular width of the
BRDF sensor aperture (e.g., less than about a degree for OCEL data).

For example, when there is a single large measured zero bistatic BRDF point at zero degrees and
all other points are near zero, we must do a little reconstructive surgery. The issue is that the
receiving aperture is no longer a point sample, but integrates the scattered intensity profile,
capturing perhaps all the energy. The measurement is no longer a BRDF. The problem is that we
have no knowledge of the actual BRDF profile—none whatsoever. There are an infinite number of

possible profiles for angles less than the second measured point that could give the same measurement. Some will have higher peak values than others. The approach we took was to construct a Gaussian-shaped BRDF profile that matches the measured peak (low as it might be) and the next measured BRDF value. The width of the Gaussian was chosen to generate the peak BRDF at zero degrees. From zero to the next measured bi_factor, the new bi_factor profile follows:

$$\text{bi\_factor}(\theta_N) = \frac{e^{-2 \cdot \theta_N^2 / \sigma^2}}{2 \cdot \pi \cdot \sigma^2} + \text{bi\_factor}(\theta_{next}) \qquad (\text{sr}^{-1}) \quad (5.8)$$

where σ is given by:

$$\sigma = \frac{1}{\sqrt{2 \cdot \pi \cdot \rho'_{peak}(\theta_N = 0)}} \qquad (\text{sr}^{-1}) \quad (5.9)$$

The primary reason to interpolate to a new bi_factor profile is to ensure a reasonable normalization. In fact, one of the consequences of the poor measurement resolution is a normalization that is well above unity.

At the other extreme, when the surface finish is very rough, the bi_factor is probably very small and therefore inconsequential.

If the surface is reasonably smooth, then we can solve reliably for the normal incidence Fresnel reflectivity R(0) by integrating the specular zero bistatic BRDF (cf. Equation 3.31):

$$R(0) = 2\pi \cdot \int_0^{\pi/2} 4 \cdot \overline{\Delta\rho'_{specular}}(\theta_N) \cdot \cos^3(\theta) \cdot \sin(\theta) \cdot d\theta \qquad (5.10)$$

For metals, R(0) should be reasonably close to the actual hemispherical reflectivity, even for somewhat rough surfaces. For clear dielectrics, R(0) should be somewhere between about 4% and 10% or the nominal Fresnel reflectance for the dielectric. We never need to know R(0) explicitly to successfully use the Maxwell-Beard BRDF model–all we need is the bi_factor. So Equation 5.8 does not need to be valid. It is more of intellectual interest right now.

Earlier, we made the claim that for somewhat shiny metals the hemispherical reflectivity, DHR(0), is closely related to the normal incidence Fresnel reflectivity R(0), and therefore to the complex indices of refraction. Physically this is so because for even polarized incident light, the Fresnel curves remain reasonably flat to angles greater than 45 degrees, which means that when light reflects off the micro-facets it loses about the same amount of energy regardless of reflection direction. Thus, each little light ray effectively sees the same loss as it goes somewhere back into the incident hemisphere. To show this, let us start with Equation 2.3 for the hemispherical reflectivity,

$$\text{DHR}(\theta_i = 0) = \int_0^{2\pi} \int_0^{\pi/2} \frac{R_{PP}(\beta)}{R(0)} \cdot \frac{\text{bi\_factor}(\theta_N)}{\cos(\theta_i) \cdot \cos(\theta_r)} \cdot S_o \cdot \cos(\theta) \cdot \sin(\theta) \cdot d\theta \cdot d\varphi \qquad (5.11)$$

where we have dismissed the diffuse term because it is not part of the specular hemispherical reflectivity, and is usually small for first-surface effects anyway. We will assume that the laser is incident along the normal such that θ_i is zero. We will also assume unpolarized incident light. This geometry immediately means $\beta = \theta_N$, and $\theta_N = \theta/2$ for the integration. Next we substitute the bi_factor equivalent terms using Equation 5.7 above, drop the S_o shadow masking term because it is usually very near 1 for moderately shiny surfaces, and cancel the cosine terms:

$$\text{DHR}(\theta_i = 0) = \int_0^{2\pi} \int_0^{\pi/2} \frac{R_{un}(\beta)}{R(0)} \cdot \frac{R(0) \cdot \Xi(\theta_N)}{4} \cdot \sin(\theta) \cdot d\theta \cdot d\varphi \qquad (5.12)$$

Using consistent variables, this gives us:

$$\text{DHR}(\theta_i = 0) = \frac{R(0)}{4} \int_0^{2\pi} \int_0^{\pi/2} \frac{R_{un}(\theta/2)}{R(0)} \cdot \Xi(\theta/2) \cdot \sin(\theta) \cdot d\theta \cdot d\varphi \qquad (5.13)$$

If we do a substitution of variables $\theta = 2 \cdot \alpha$, $d\theta = 2 \cdot d\alpha$, and recognize $\sin(2\alpha) = 2\sin(\alpha) \cdot \cos(\alpha)$:

$$\text{DHR}(\theta_i = 0) = R(0) \cdot \int_0^{2\pi} d\varphi \int_0^{\pi/4} \frac{R_{un}(\alpha)}{R(0)} \cdot \Xi(\alpha) \cdot \cos(\alpha) \cdot \sin(\alpha) \cdot d\alpha \qquad (5.14)$$

Except for the limits of integration and the Fresnel ratio, the double integral will evaluate approximately to unity according to Equation 3.29. As another small approximation, we will drop the normalized Fresnel ratio since it is nearly 1 for angles less than 45 degrees (see Figures 3.8 and 3.10), which are the alpha limits of integration. If the surface is shiny enough, then the tilt distribution will have a vanishing contribution for angles above 45 degrees anyway. Thus, with little error, given a moderately shiny surface, we can extend the limits of integration to 90 degrees and arrive at the good approximation DHR(0) ~ R(0) for the first-surface scatter. Equation 5.14 should reinforce the idea that any micro-facets tilted at angles greater than 45 degrees (the limits of integration) reflect light rays down into the surface grooves, causing multiple reflections and hence wide-angle depolarized diffuse scatter. In the limit of a very shiny surface, then clearly the Fresnel law demands DHR(0) = R(0). Thus, the indices do determine the DHR. For non-normal incidence the integral of Equation 5.14 is not so symmetrical. However, it should be clear that out to fairly large angles the same arguments hold, and that DHR(0) ~ R(0). In the limit of very shiny surfaces, the reflectance should follow Fresnel's law.

5.2   Extracting the Depolarized Diffuse Parameters

The total unpolarized diffuse scatter for both polarization states is given by Equation 3.54:

$$\rho'(\theta_i, \theta_r)_{diffuse} = R_x + 2\frac{R_{hov}}{\cos(\theta_i) + \cos(\theta_r)} \quad (\text{sr}^{-1}) \qquad (5.15)$$

There are two constant parameters to extract, R_x and R_{hov}. Each parameter has about the same influence on the final BRDF value. The second non-Lambertian term turns up at large angles, as an inverse cosine.

The measured total diffuse BRDF is twice either $BRDF_{SP}$, or $BRDF_{PS}$. We want to add, and thereby average, the two cross-polarized scans to get the total unpolarized diffuse BRDF:

$$\rho'(\theta_i, \theta_r)_{diffuse} = BRDF_{SP}(\theta) + BRDF_{PS}(\theta) \qquad (\text{sr}^{-1}) \qquad (5.16)$$

The measured *zero bistatic* scan data has $\theta_I = \theta_r$. Combining the last two equations:

$$BRDF_{SP}(\theta) + BRDF_{PS}(\theta) \approx R_x + \frac{R_{hov}}{\cos(\theta)} \qquad (\text{sr}^{-1}) \qquad (5.17)$$

To estimate the two constant parameters R_x and R_{hov}, we will do a least-squares fit to the measured cross-polarized BRDF data. This follows a simple minimization process frequently seen for regression analysis. For each measured diffuse BRDF point, we calculate the squared error between the estimated and the measured values:

$$\sum_{1}^{N} \left\{ [BRDF_{SP}(\theta) + BRDF_{PS}(\theta)] - \left[R_x + \frac{R_{hov}}{\cos(\theta)} \right] \right\}^2 = \varepsilon^2 \qquad (\text{sr}^{-1}) \qquad (5.18)$$

where there are N measured BRDF points. Clearly we want to find the minimum squared error ε^2 as a function of the two estimated parameters R_x and R_{hov}. Therefore, take two derivatives of Equation 5.18 by the two parameters, and set each equation to zero (minimum squared error):

$$\frac{d}{dR_x} \sum_{1}^{N} \left\{ \left[BRDF_{SP}(\theta) + BRDF_{PS}(\theta) \right] - [R_x + \frac{R_{hov}}{\cos(\theta)}] \right\}^2 = 0 \qquad (5.19)$$

$$\frac{d}{dR_{hov}} \sum_{1}^{N} \left\{ \left[BRDF_{SP}(\theta) + BRDF_{PS}(\theta) \right] - [R_x + \frac{R_{hov}}{\cos(\theta)}] \right\}^2 = 0 \qquad (5.20)$$

Let us substitute ρ for the total diffuse reflectance (i.e., $\rho(\theta) = BRDF_{SP}(\theta) + BRDF_{PS}(\theta)$), take the derivatives, and rearrange to get two linear equations in two unknowns:

$$\sum_{1}^{N} \rho(\theta) = N \cdot R_x + \sum_{1}^{N} \frac{1}{\cos(\theta)} \cdot R_{hov} \qquad (5.21)$$

$$\sum_{1}^{N} \frac{\rho(\theta)}{\cos(\theta)} = \sum_{1}^{N} \frac{1}{\cos(\theta)} \cdot R_x + \sum_{1}^{N} \frac{1}{\cos^2(\theta)} \cdot R_{hov} \qquad (5.22)$$

We solve for R_x in Equation 5.21, substitute it into Equation 5.22, and solve for R_{hov}:

$$R_{hov} = \frac{1}{N \cdot \left(\sum_{1}^{N} \frac{1}{\cos^2(\theta)} - \sum_{1}^{N} \frac{1}{\cos(\theta)} \right)^2} \cdot \left[N \cdot \sum_{1}^{N} \frac{\rho(\theta)}{\cos(\theta)} - \sum_{1}^{N} \frac{1}{\cos(\theta)} \cdot \sum_{1}^{N} \rho(\theta) \right] \qquad (5.23)$$

We next solve for R_x in the same manner, or simply do the summations in Equation 5.21 using the estimated value for R_{hov}, and solve for R_x:

$$R_x = \frac{\sum_1^N \rho - R_{hov} \sum_1^N \frac{1}{\cos(\theta)}}{N} \tag{5.24}$$

In the event R_{hov} that goes negative (which is reasonable mathematically), we need to clamp R_{hov} to zero to avoid unphysical behavior. If this occurs, then R_x calculated according to Equation 5.24 is just the simple mean of the data points, which is the best estimate in the least-squares sense. Again, we are doing parameter fits to measured data. We do not necessarily know exactly where the diffuse scatter originates in the material, but that is OK for modeling the diffuse BRDF.

Equation 5.15 models a Lambertian and a particular kind of non-Lambertian diffuse BRDF functional form (see Section 3). Therefore, unlike the specular BRDF model, if we difference a measured and modeled diffuse BRDF we are very likely to see a residual difference. This is a consequence of unmodeled physics in our Equation 5.15. For example, consider the diffuse measured BRDF curve in right-hand Figure 5.4. The shape of that BRDF curve does not follow either the Lambertian (i.e., flat), or non-Lambertian (inverse cosine) functional forms. This same figure also points out an important extraction consideration – if the specular BRDF is large, then even a small leakage through the linear polarizer will contaminate the cross-polarized scans. This contamination is clearly seen in this figure. When doing the least-squares fit in Equations 5.21 to 5.24, we must be careful to exclude this data because it will distort the answer toward higher values.

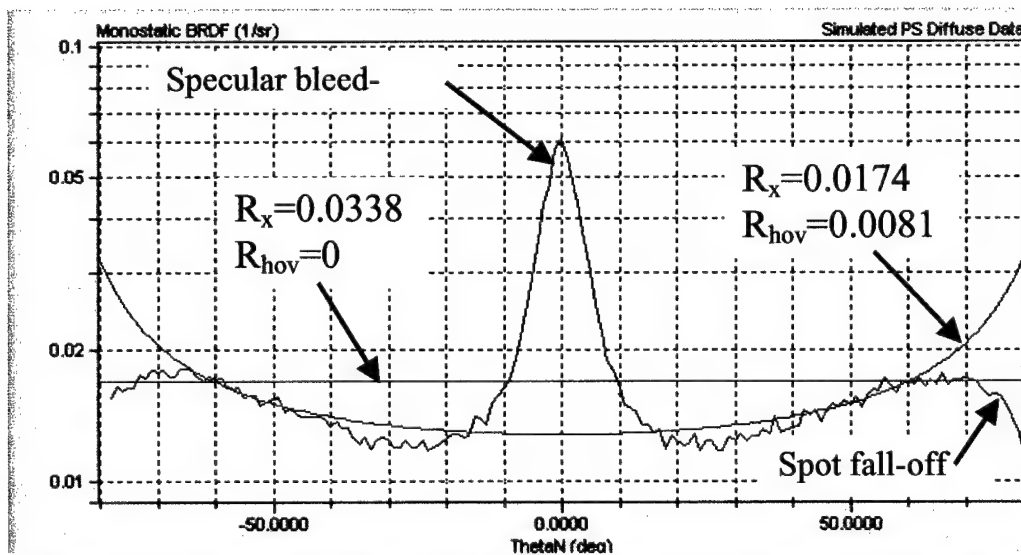Consider the two extracted parameter pairs shown in Figure 5.6.

Figure 5.6. Measured Diffuse BRDF (Blue) with Two Parameter Extraction Curves Over Plotted (Red)

The upper flat red line was least-squares fitted to all the measured data (i.e., from 0 to 85 degrees). Clearly this line (and R_x) is too high. The lower red curve was fitted to only those data points between 20 and 70 degrees. The fit for the second is much better. The measured data falls off past 70 degrees, probably because the laser spot is beginning to fall off the sample surface.

5.3 Extracting the Complex Indices of Refraction from Measured Data

The zero bistatic measurements cannot address the complex indices of refraction (n, κ) directly. In this section we will estimate the indices either by using some reasonable approximations, or by doing a least-squares fit to scissor-type bistatic intensity scan data.

The indices are responsible for capturing the complete polarization effects. Exact values for the indices are critical to doing very detailed and precise polarization rendering. Thus, the best objective would be to somehow extract the *exact* indices. However, we really do not need to know them exactly to reasonably approximate BRDF radiometric modeling. According to Equation 5.7, the bi_factor already contains the vital normal incidence Fresnel reflectance $R(0)$, which comes from the zero bistatic scans. And, according to Equations 3.55 through 3.61, we really only need indices that give a Fresnel *ratio* (i.e., the normalized Fresnel curve) that best captures the polarized behavior at the larger angles.

There are only two critical polarization features in the normalized Fresnel curve to consider. The most important is the rise from unity at normal incidence to a value of $1/R(0)$ at 90 degrees. This is the feature whose accuracy is most critical, because it affects the grazing incidence reflectivity (in some cases, a lot). Unfortunately, this rise in reflectivity is difficult to measure accurately, and measuring the normal incidence Fresnel reflectance directly can also be difficult.

The second feature is the Brewster angle, i.e., the dip in the P to P reflectance. This is probably a little easier to measure because it usually occurs at reasonable angles. We know that the normal incidence reflectance $R(0)$ is a function of both n and κ. In Equations 3.15 and 3.16, we showed how to solve for either index given the other. If we vary the real index between its lower and upper values, for a given $R(0)$ for example, we can solve parametrically for the complex index κ. Then for each index pair (always giving the same $R(0)$), we can always find the Brewster angle, which is unique.

The easiest approach to estimating the indices is to use our best estimate of the normal incidence reflectance $R(0)$ (from Equation 5.10 for example), make a couple of reasonable physical approximations, and analytically solve. This should be a reasonable approach that yields results far better than our second approach, which does a detailed least-squares fit. If we had no additional measured bistatic reflectance data, we could still consult published handbooks for typical indices for common materials to get a good ballpark estimate for the indices, and perhaps refine this with the extracted $R(0)$ value.

Thus, we essentially have two constraints on the Fresnel function and two variables. We should strive to adequately determine the $R(0)$, build a table of index pairs that generate this value, and then search the table for a Brewster angle that closely matches to one measured. Now, along with the Brewster angle comes the relative dip in the P polarization reflectance. It is of secondary importance if the modeled Brewster dip is different from the measured value. The probable reason for this inconsistency is measurement error.

If the material is a dielectric (e.g., paint or plastic) for which we are sure the dielectric binder is reasonably clear at the desired laser wavelength, then we first set κ to zero (it is usually very close to zero for transmissive dielectrics), and solve for n using Equation 3.16 given a reasonable value (say, 4% to 10%) for the normal incidence Fresnel reflectivity $R(0)$. Typical values of a real index range from about 1.2 to 6 for optical glasses, usually not going above 2.0. There should be little error because we already know κ fairly well. The modeled Brewster angle should occur at about the correct angle. The Brewster dip goes to zero at the Brewster angle. The rise in reflectivity at grazing angles should also be reasonably accurate. In the complete absence of any data, a good choice for the real index n is 1.5 (which means $R(0)$ is about 4%).

At longer infrared wavelengths, the dielectric (e.g., plastic binder in paints) can begin to become opaque and hide the material volumetric region (pigment). In this case the first-surface reflection would dominate, κ would no longer be zero, and one would want to treat the material more like a metal with little diffuse contribution.

On the other hand, if the material is a metal, then we would set the real index n equal to something between 1.0 and 2.0, and solve for κ, using Equation 3.15 and a reasonable value for $R(0)$. The value we assume for $R(0)$ can either be the one generated from the integration in Equation 5.10, or come from a separate knowledge of the DHR(0). Remember that the critical feature we need to correctly capture is the grazing incidence rise. The reflectance for a metal is driven entirely by its Fresnel reflectance, which is usually rather high. Thus, if we know the hemispherical reflectance, then we would assign this to $R(0)$ and probably be very close to reality. Looking back at Figure 3.8, the Brewster angle (and relative droop in the reflectivity curve at the Brewster angle) increases only slightly with increasing real index n for the same normal incidence reflectivity, when n is above unity. So our assumptions for the indices incur minimal error in the BRDF model. In either case, the error is especially small when we consider the fact that we will be using the unpolarized *mean* of the S and P curves, which manifests polarized behavior only at large angles.

If we have measured scissor-type bistatic intensity scan data, then we can attempt to do a least-squares fit to the measured data, and treat n and κ as free parameters. The measured data are treated as relative intensities taken along the nominal specular direction in the plane of incidence. Assume the sensor aperture is much smaller than the BRDF specular lobe, and measurement geometry is bistatic as shown in Figure 3.1 with $\theta_i = \theta_r$. The measured power at the sensor would be:

$$P_{rec} = I_o \cdot \cos(\theta_i) \cdot \rho' \cdot \cos(\theta_r) \cdot A \cdot \delta\Omega_{rec} \qquad (w) \qquad (5.25)$$

We will define here a point reflectance that is the ratio of the received power to the incident power:

$$R_{XX} = \frac{P_{rec}}{P_{in}} = \frac{I_o \cdot \cos(\theta_i) \cdot \rho'_{XX} \cdot \cos(\theta_r) \cdot A \cdot \delta\Omega_{rec}}{I_o \cdot \cos(\theta_i) \cdot A} = \rho'_{XX} \cdot \cos(\theta_r) \cdot \delta\Omega_{rec} \qquad (5.26)$$

where the *XX* is the polarized state notation. Notice that this quantity is a function of the receiver solid angle! We know the BRDF from Equation 3.55, so the point reflectance is:

$$R_{XX}(\theta) = \left\{ N_{XX}(\theta) \cdot \frac{bi\_factor(0)}{\cos^2(\theta)} + \frac{1}{2}\left[R_x + \frac{R_{hov}}{\cos(\theta)} \right] \right\} \cdot \cos(\theta) \cdot \delta\Omega_{rec} \qquad (5.27)$$

where we dropped the shadow/masking term because it is unity, made the incident and reflected angles the same, and set the argument to the bi_factor to zero because we are sensing along the specular direction. We used the notation that N_{xx} is the normalized Fresnel ratio. Notice also that the point reflectance is a function of the incident/received polarization state. We can immediately solve for the receiver solid angle given a normal incidence point reflectance value $R_{xx}(0)$:

$$\delta\Omega_{rec} = \frac{R_{XX}(0)}{bi\_factor(0) + \frac{1}{2}\left[R_x + R_{hov} \right]} \qquad (sr^{-1}) \qquad (5.28)$$

where we simplified the cosine terms to unity at normal incidence and recognized the Fresnel ratio as unity also. Next we solve for the Fresnel ratio knowing $\delta\Omega_{rec}$:

$$N_{XX}(\theta) = \frac{\cos^2(\theta)}{bi\_factor(0)} \cdot \left\{ \frac{R_{XX}(\theta)}{\cos(\theta) \cdot \delta\Omega_{rec}} - \frac{1}{2}\left[R_x + \frac{R_{hov}}{\cos(\theta)} \right] \right\} \qquad (5.29)$$

Factoring slightly:

$$N_{XX}(\theta) = \frac{\cos(\theta)}{bi\_factor(0) \cdot \delta\Omega_{rec}} \cdot \left\{ R_{XX}(\theta) - \frac{1}{2}\left[R_x + \frac{R_{hov}}{\cos(\theta)} \right] \cdot \cos(\theta) \cdot \delta\Omega_{rec} \right\} \qquad (5.30)$$

which can be simplified to:

$$N_{XX}(\theta) = k \cdot \left\{ R_{XX}(\theta) - R_{diffuse} \right\} \cdot \cos(\theta) \qquad (5.31)$$

where $R_{diffuse}$ is the diffuse contribution at the receiver, and k is a proportionality constant. Thus, we remove the diffuse depolarized reflectance contribution from the measurement, and scale with a cosine factor. The constant k is not important, since we will normalize this curve anyway.

Now we need to consider another possibility before continuing on to the least-squares fit. What if the receiver aperture is greater than the reflected spot size? Then the power captured by the receiver must be an integral over the area of the aperture. This changes Equation 5.26 to:

$$R(\theta) = \frac{P_{rec}(\theta)}{P_{in}} = \int \rho'(\theta) \cdot \cos(\theta_r) \cdot \delta\Omega_{rec} = F_{XX}(\theta) \qquad (5.32)$$

where $F_{xx}(\theta)$ is the Fresnel reflectance. This result applies when the surface is extremely shiny. If the reflected power contains a significant diffuse contribution, and the specular spot is much less than the aperture diameter, we can alter Equation 5.31 to:

$$N_{XX}(\theta) = \left\{ R_{XX}(\theta) - R_{diffuse} \right\} = \left\{ R_{XX}(\theta) - \frac{1}{2}\left[R_x + \frac{R_{hov}}{\cos(\theta)} \right] \cdot \cos(\theta) \cdot \delta\Omega_{rec} \right\} \qquad (5.33)$$

where the receiver solid angle will probably need to be estimated from knowledge of the measurement apparatus. Note also that in Equations 5.31 and 5.33 we never allow N_{xx} to go less than zero.

Now that we have an approximate representation of the Fresnel effects in $N_{xx}(\theta)$, we can search for an index pair that will reproduce this curve. Our approach is to do a least-squares fit of a normalized Fresnel curve to N_{xx}. One method is to do two linear minimizations separately. One can search over k looking for a minimum squared error between the N_{xx} and the normalized Fresnel curve, while always forcing n to give the same Brewster angle. Another method is to use a basic simplex optimization algorithm and let it systematically search for the best index pair to fit the N_{xx} curve.

While the normalized Fresnel curve is a unique function of the two indices, small measurement errors can lead to unexpected results in the index pairs. A little thought and care should be used in accepting the results. One should limit the angular range in the data that is used in the least-squares fit. In the final step, one should reject unreasonable index pairs and probably use the approximate method outlined above.

On the practical side, notice that doing a fit to measured data for angles less than about 45 degrees is useless, because there are no manifest polarization features here. The normalized Fresnel curves can be nearly flat at unity out to angles beyond this. Virtually *any* pair of indices will produce working normalized Fresnel curves for small angles. The downside of using data for angles less than about 45 degrees is that measurement errors tend to drive the resulting index pair to unreasonably large values.

In principle, the angles near grazing incidence give a reflectance ratio always greater than 1 and equal to the inverse of the normal incidence reflectance. We should probably strive to properly address the normal incidence Fresnel reflectance. If we do an adequate fit to the rise in the data at the grazing angles, then we are assured that our choice for the indices will produce the correct normal incidence reflectance. Frequently the data are bad at these angles because the laser spot starts falling off the material sample, giving erroneous values for the reflectance. So, unfortunately, we must reject this data from the fit.
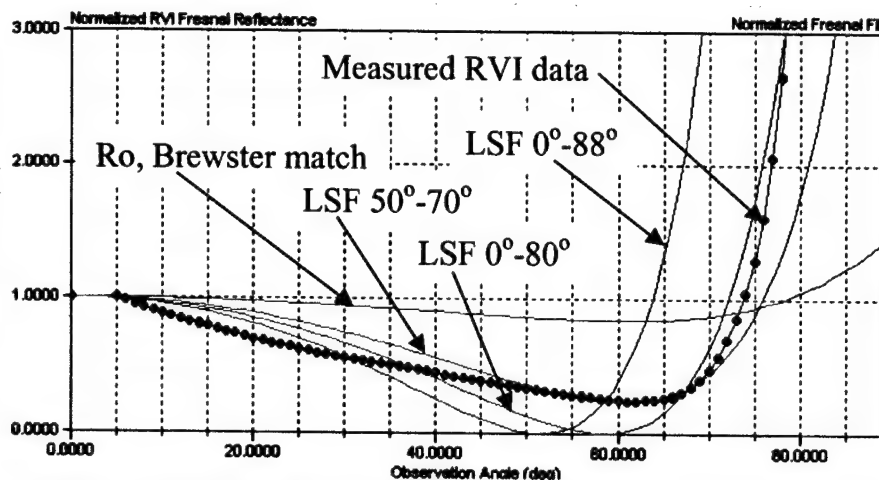
Figure 5.7. RVI Least-squares Fit for n, k *Indices. Measured Data are Red, Fitted Data Green*

Consider the same material data used above for the bi_factor and diffuse parameter extractions. In Figure 5.7 we show several least-squares fits to the RVI scan data.

The top green curve comes from matching the indices to the estimated normal incidence reflectance $R(0)$ and to the Brewster angle at about 61 degrees. This is probably the most reasonable, since the material is aluminum. Among the three least-squares fitted curves, the one that uses the data from 50 to 70 degrees is the best. The grazing incidence growth in the reflectance is about 70, which is a bit extreme. The depth of the curve at the Brewster angle is also unreasonable for a metal. The measured data is very troublesome for angles less than 40 degrees because it is too low (regardless of the indices). This is probably a good case where one would frankly reject the fitting approach and use the solution method outlined above (as was done for the top green curve).

If we decide to use indices that give a normal incidence reflectance $R(0)$ very much different from the true value, they will lead to erroneous hemispherical reflectance values at grazing angles. One often finds extracted values for a metal that generate a very low R(0), which in turn leads to a very large rise in the reflectance at large angles, which then drives the hemispherical reflectance above unity! This is clearly unphysical and should be avoided.

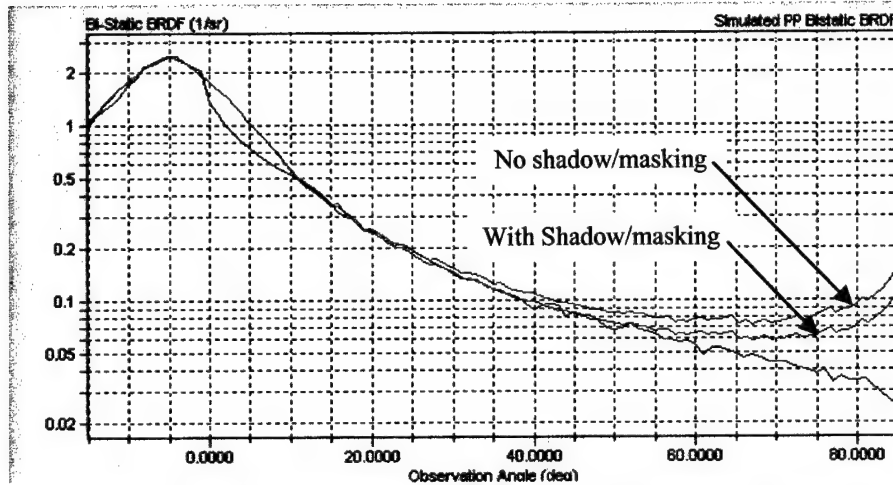## 5.4 Extracting the Shadow/Masking Parameters from Measured Data

Figure 5.8. Shadow/Masking Effects for Moderately Shiny Aluminum
(Red = Simulated, Blue = Measured)

The shadow/masking parameters have the effect of knocking down the bistatic BRDF for angles away from the specular. Therefore we use bistatic scans and do least-squares fits to search for the τ and Ω parameters that will best match the measured bistatic data. Figure 5.8 shows an example for the moderately shiny aluminum used above.

The blue curve is the measured bistatic BRDF. The upper red curve is the simulated BRDF without any shadow/masking effect. The lower red curve shows how the shadow/masking function S_o begins to fit the data better at the larger angles.

Figure 5.9 shows an example for a very shiny aluminum. The incident angle is 30 degrees. The blue line is the measured bistatic BRDF. The top red curve is the optimal $\tau = 0.57$ and $\Omega = 85.0$ parameter fit for this material. Two other curves for different Ω values are shown for comparison. The green curves are the generated shadow/masking functions S_o. This material is so smooth that there are virtually no manifest shadow/masking effects.

Estimating the shadow/masking parameters (τ, Ω) again involves doing a least-squares optimized fit using a simplex algorithm. The measured bistatic BRDF curve is simply differenced against the
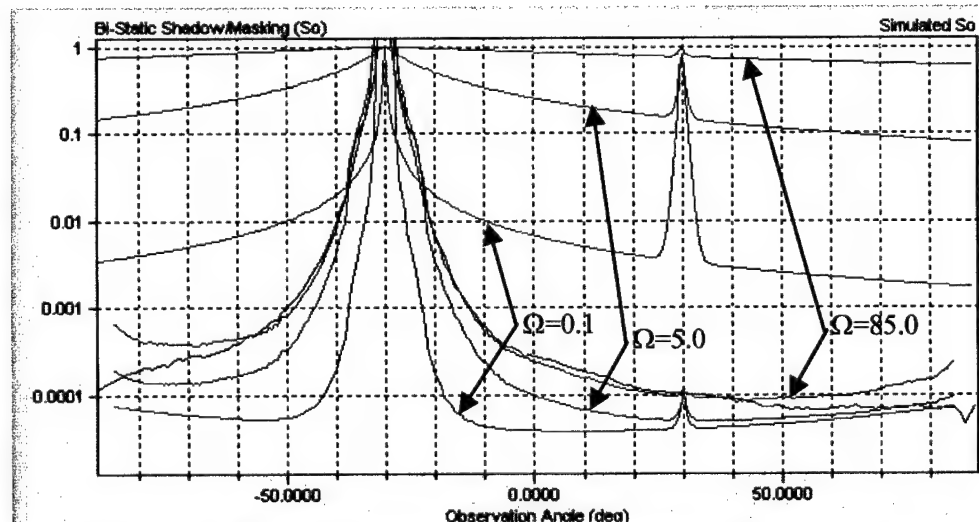

Figure 5.9. Shadow/Masking τ and Ω Parameter Fitting to Shiny Aluminum.

simulated BRDF to generate a squared error, which is then minimized as a function of (τ, Ω). Since the shadow/masking function S_o has very little effect near the specular direction, those data points should be eliminated from the fit. Likewise, points at large angles tend to be driven by diffuse effects which should also be ignored. In the example given in Figure 5.9, the fit was done between −10 and +60 degrees.

The measured bistatic BRDF should probably have its cross-polarized diffuse component removed before doing the least-squares fit, because the diffuse part is not affected by the S_o function. However, this data is not available so we must include the diffuse part of the simulated BRDF.

Including the shadow/masking effects is really a second-order improvement to the BRDF model, at best. Without S_o the specular polarized BRDF, at worst, could be incorrectly modeled a little high at angles far from the specular direction, hence where intensities are down already and of secondary importance. When in doubt, one can assign large values to the two parameters (e.g., 1000), to effectively inhibit their influence on the BRDF. This always produces a BRDF higher than that which would have been calculated with smaller parameters, and this would always be more conservative.

More disturbing, for some materials, is a trend in the measured bistatic BRDF data in which the peak drops as the incident angle increases. It should generally increase as an inverse cosine squared, and slightly fall off with the Fresnel Brewster dip (these are P to P polarized scans). Figure 5.10 shows this behavior, both measured and modeled. The red curves are the modeled BRDFs, which indeed show an increase in the peak as the angle increases. The blue curves are the measured BRDFs. Instead of climbing, they consistently fall in BRDF value (not intensity!). It is not clear whether this is just bad measured data, or whether other BRDF physics is at work here. For other materials, we do see the correct behavior.

One might be tempted to conclude that this behavior is due to shadow/masking at the larger angles, thereby dropping the BRDF. But this seems unlikely because the material was polished to an RMS roughness of

Figure 5.10. Measured and Modeled Bistatic BRDF for Increasing Angle of Incidence

800 nm ($\lambda/1.25$). The micro-facet tilts seems mostly to be less than 15 degrees, so it seems difficult to believe there would be much shadowing or masking. Even if there were, the functional form of the shadow/masking function S_o will not attenuate the peak BRDF anyway.
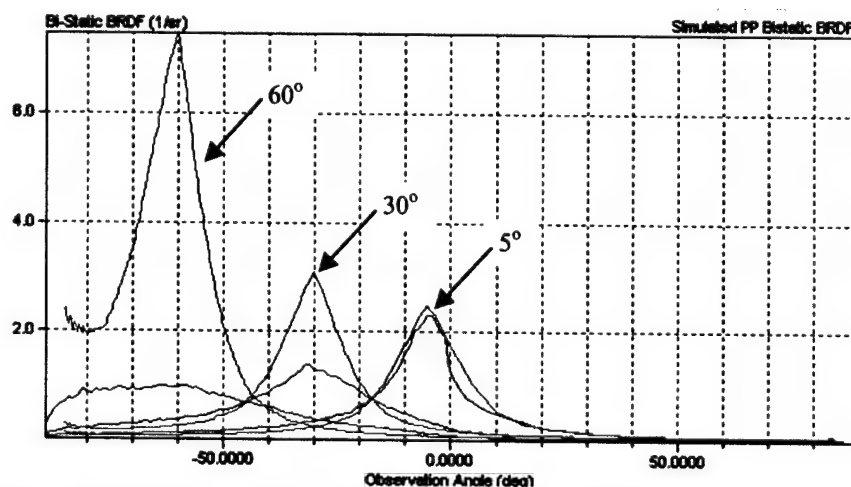
5.5   General Comments about Extracting Parameters

In this section, we have presented a number of analytical and other approaches to extract the Maxwell-Beard BRDF parameters. The most significant are the zero bistatic data, from which we extract the bi_factor and the diffuse parameters. This is mandatory. Extracting the complex indices and the shadow/masking parameters takes a lot of work and returns very little in terms of increased fidelity. One can do a good job of extracting useful parameters from just the zero bistatic measured scans and a little reasoning.

Depending on the application of the data, the required accuracy for the complex indices can vary. For LRST we need not extract them to a high degree of accuracy. We can afford some variation without compromising the radiometric results too much, because we are using an unpolarized and *normalized* Fresnel function. For other applications, such as signature rendering, we would be more concerned about the accuracy of the refractive indices.

The process of extracting the data is sequential and iterative in nature. The bi_factor is easy and automatic, with no user intervention. The diffuse parameters are easy, but require the user to possibly exclude some data due to cross-polarized leakage. Extracting the indices is the most difficult extraction task. There are two completely different methods for extracting the refractive indices. The user can do them manually, or try to do a least-squares fit of a normalized Fresnel curve to measured bistatic intensity data. We really think the best approach to estimating indices is to manually match the normal incidence reflectance and the Brewster angle. If the user thinks there are shadow/masking artifacts in the measured bistatic BRDF data, then one can do a least-squares fit to estimate the parameters.

The user must always be aware that all BRDF measurements are fraught with noise, errors, measurement artifacts, and run-to-run inconsistencies. We have addressed a few of these problems above, but others will probably plague all attempts to extract data. This brings us full circle to not taking BRDF data too seriously. There are a lot of minor compromises that have to be made. BRDFs are complicated and vary widely between materials. Not all material BRDFs can be completely modeled by the Maxwell-Beard BRDF model. However, most of the important ones we will likely encounter in the context of LRST can be.

6.0　Shifting Wavelength and Renormalizing the BRDF

The Maxwell-Beard BRDF is typically measured at only a few wavelengths because of cost or equipment considerations. The radiometric simulation codes, however, need to make radiometric predictions for any wavelength within the stated limits of the simulation application, which usually ranges from the UV to the LWIR. We will therefore need a methodology for synthesizing a reasonable approximation to each material BRDF, as it is called out in the target model, at wavelengths where data was not directly measured. This will require making some physical assumptions and relying on the fact that the optical properties of most common materials behave reasonably well and that color and geometric spread are usually decoupled.

While we cannot always measure BRDFs at all wavelengths, we can easily measure the hemispherical reflectivity for each material at closely separated wavelengths over a very wide spectral bandwidth. This color curve is used to tie to reality the BRDF we synthesize at any wavelength within this band. Whatever BRDF interpolation scheme we decide on will certainly introduce some deviation between model and reality. At a minimum we can at least guarantee that the energy balance is preserved. In fact, even at the measurement wavelengths for the BRDFs, we will still renormalize the BRDF to this color curve for consistency.

The synthesis process is done in two steps. First we derive BRDF model parameters through interpolations; second, we renormalize the BRDF to the color curve. In some cases, the interpolation step is quite similar to the renormalization. When we have BRDF measurements that bracket the desired wavelength, we will *interpolate* the respective BRDF parameters and *renormalize* the BRDF to match the measured total hemispherical reflectivity. If the desired wavelength is outside the measured BRDF set, we will use the nearest single BRDF measurement and just renormalize the hemispherical reflectivity. We will not extrapolate BRDF parameters.

6.1　Interpolating the BRDF Parameters

The Maxwell-Beard BRDF model is based on the theoretical assumption that the first-surface scatter is driven primarily by a purely geometric micro-facet specular-ray reflection process, and the polarization is driven by the normalized Fresnel equations for these facets. This assumption works well when the RMS surface roughness is on the order of a wavelength or larger, where diffraction effects are less important. For most target object materials the surface roughness is usually much greater than 1μm RMS, which means the model will work well out into the MWIR and perhaps at longer wavelengths. Surfaces smoother than the wavelength are locally approaching optical-quality polish, diffraction does become important, and the BRDF specular spread does tend to couple with wavelength. Glass would be a common example for which the typical surface roughness is much less than the wavelength, even in the visible region. Many materials appear quite smooth in the LWIR region because of the longer wavelength, while having a broad BRDF in the visible.

The Maxwell-Beard BRDF model puts its wavelength-dependent reflectance into the bi_factor, which is the product of the tilt distribution function and the normal incidence reflectance

(Equation 5.7). The bi_factor measured for short wavelengths (e.g., near-IR or visible wavelengths) has basically the same shape but is scaled linearly with changing reflectivity, by wavelength. At the longer wavelengths where diffraction and wave effects become important, the bi_factor no longer represents purely geometrical scatter by tilted micro-facets. Here the bi_factor begins to represent both an *effective* facet distribution and a reflectance. This is why a single BRDF measurement at a single wavelength is not sufficient if one expects to model radiometric quantities at both the shorter and the longer wavelengths.

There are at least three approaches to approximating a BRDF at a wavelength between two bracketing wavelengths where data are measured. The simplest is just to take the measured data as is, at the closest wavelength, and just rescale the hemispherical integral to match the measured directional hemispherical reflectivity (DRH) at the new desired wavelength:

$$\text{BRDF}(\lambda_{desired}) = \text{DHR}(\theta_{in} = 0, \lambda_{desired}) \cdot \left[\frac{\text{BRDF}(\lambda_{closest})}{\int \text{BRDF} \cdot \cos(\theta) \cdot d\Omega} \right] \tag{6.1}$$

Note that the quantity in brackets is a unity reflectivity BRDF function. The denominator is the DHR for that BRDF, at that wavelength, for normally incident light.

The shortcoming of this approach is that the BRDF character will discontinuously jump as the wavelength passes midway between measured data sets. Worse yet, it also suffers by ignoring the detailed mechanisms by which the changes in reflectivity arise. For example, if the material is a dielectric, then as one changes wavelength, the dominant effect is how the paint pigment changes reflectivity. The first-surface scatter does not change color, because the clear binder refractive indices do not really change much with wavelength. Such a simple rescaling changes both effects equally, which is an approximation we can improve upon.

The second approach is to linearly interpolate between bracketing BRDFs, and rescale to the new DHR. Thus:

$$\text{BRDF}(\lambda_{desired}) = \text{DHR}(\lambda_{desired}) \cdot \left[(1.0 - Q) \cdot \frac{\text{BRDF}_1(\lambda_1)}{\int \text{BRDF}_1 \cdot \cos(\theta) \cdot d\Omega} + Q \cdot \frac{\text{BRDF}_2(\lambda_2)}{\int \text{BRDF}_2 \cdot \cos(\theta) \cdot d\Omega} \right] \tag{6.2}$$

where the BRDFs at each bracketing wavelength are both linearly weighted and re-normalized to unity reflectivity. Q is the linear weighting factor going from the shorter wavelength λ_1 to the longer wavelength λ_2:

$$Q = \frac{\lambda_{desired} - \lambda_1}{\lambda_2 - \lambda_1} \tag{6.3}$$

This approach improves upon the discontinuous behavior. The shape of the BRDF will change continuously between wavelengths. It again suffers from not properly adjusting the detailed effects at the intermediate wavelengths. This is not a bad approach, and is the one used for non-conventional exploitation factors (NEF) modeling (Reference 5). It does require calculating two BRDFs, which is a bit inefficient.

A third approach is to interpolate each of the respective BRDF parameters (in some logical way), synthesize a single new material, and then renormalize to the respective DHR. Our desire is to avoid any discontinuous behavior, and to preserve the underlying detailed physical changes occurring as the wavelength changes between the bracketing measured BRDF wavelengths. Each parameter will be interpolated to avoid the discontinuous jumps. We will also need to pay attention to the material type to differentiate how we renormalize and balance the effects.

For the Maxwell-Beard BRDF, we start the parameter interpolations for the bi_factor look-up table. The first assumption is that the tilt distribution function changes smoothly and linearly from one wavelength to the next. For the shorter wavelengths, it should change very little. The bi_factor, however, includes the normal incidence Fresnel reflectance, which is also changing with wavelength. So, we first try to estimate $R(0)$ by integrating the bi_factor:

$$4 \cdot \int bi\_factor(\theta_N) \cdot \cos(\theta) \cdot d\Omega = R(0) \cdot \int \Xi(\theta_N) \cdot \cos(\theta) \cdot d\Omega \approx R(0) \qquad (\text{sr}^{-1}) \quad (6.4)$$

and then minimize its influence by weighting the interpolation factors as:

$$\Xi(\theta_N, \lambda_{desired}) = \frac{(1.0 - Q)}{R_1(0)} \cdot bi\_factor\,(\theta_N, \lambda_1) + \frac{Q}{R_2(0)} \cdot bi\_factor\,(\theta_N, \lambda_2) \quad (6.5)$$

The interpolated $R(0)$ is:

$$R(0, \lambda_{desired}) = (1.0 - Q) \cdot R_1(0) + Q \cdot R_2(0) \quad (6.6)$$

Finally, the new interpolated bi_factor is the product of the new tilt function and the new $R(0)$:

$$bi\_factor\,(\theta_N, \lambda_{desired}) = R(0, \lambda_{desired}) \cdot \Xi(\theta_N, \lambda_{desired}) \quad (6.7)$$

This should capture the changes in the shape of the *effective* tilt distribution function. If the material is a dielectric, then the interpolated bi_factor probably should not be altered further. The normal incidence Fresnel reflectivity is already contained in the bi_factor, and it typically changes little with wavelength. If the material is a metal, then we will rescale the bi_factor later during the renormalization as required. Does the angular spread in the BRDF vary linearly with increasing wavelength as the interpolation implies? The answer is probably No. But this approximation is probably better than making no effort to account for the narrowing of the BRDF as the wavelength gets longer. If more accuracy is required, then more BRDF data need to be taken at intervening wavelengths.

The diffuse parameters R_x and R_{lov} change with wavelength differently than the specular parameters. If the material is a metal, then we linearly interpolate them as we did in Equation 6.6 for $R(0)$. If the material is paint, then they probably change according to pigment interactions independent of any first-surface effects. We linearly interpolate the diffuse parameters in either case:

$$R_x(\lambda_{desired}) = (1.0 - Q) \cdot R_x(\lambda_1) + Q \cdot R_x(\lambda_2) \quad (6.8)$$

$$R_{hov}(\lambda_{desired}) = (1.0 - Q) \cdot R_{hov}(\lambda_1) + Q \cdot R_{hov}(\lambda_2) \qquad (6.9)$$

These parameters were extracted as a pair using a least-squares fit, and should probably always be treated as a pair when doing any linear rescaling.

The shadow/masking parameters (τ, Ω) have a second order influence on the BRDF away from the specular direction. They are extracted using a least-squares fit and should probably be interpolated the same way the bi_factor is:

$$\tau(\lambda_{desired}) = (1.0 - Q) \cdot \tau(\lambda_1) + Q \cdot \tau(\lambda_2) \qquad (6.10)$$

$$\Omega(\lambda_{desired}) = (1.0 - Q) \cdot \Omega(\lambda_1) + Q \cdot \Omega(\lambda_2) \qquad (6.11)$$

The Fresnel indices of refraction should probably not be linearly interpolated independently of each other. Once again, without explicit measurements at the desired wavelength, how do we choose them to both satisfy the reflectivity dependence and the polarization effects (e.g., the Brewster angle)?

We want the polarization effects at the desired wavelength to be somewhere between those at the bracketing wavelengths. There are two options: hunt for a new index pair that generates an intermediate Fresnel curve, or simply pre-calculate a weighted normalized Fresnel curve based on the two normalized Fresnel curves at the bracketing wavelengths. The second approach is easier and more direct.

$$R_{SS}(\lambda_{desired}) = (1.0 - Q) \cdot R_{SS}(\lambda_1) + Q \cdot R_{SS}(\lambda_2) \qquad (6.12)$$

$$R_{PP}(\lambda_{desired}) = (1.0 - Q) \cdot R_{PP}(\lambda_1) + Q \cdot R_{PP}(\lambda_2) \qquad (6.13)$$

and we can extend this to the normalized Fresnel reflectivity:

$$F_{SS}^{normalized}(\beta) = \frac{R_{SS}(\beta, \lambda)}{R(0, \lambda)} \qquad F_{PP}^{normalized}(\beta) = \frac{R_{PP}(\beta, \lambda)}{R(0, \lambda)} \qquad (6.14)$$

The resulting interpolated normalized Fresnel curve might not be physical, so we could again do a least-squares fit to find the closest physical index pair. However, this is unnecessary, since the error would be very small, and the normalized Fresnel curves are a bit suspect from the beginning.

6.2 Re-normalizing the BRDF to the DHR

Now that we have our new estimates of the BRDF model parameter set, we can *renormalize* the BRDF model to match the measured DHR. The measured DHR is usually done with unpolarized broadband light. In principle all the scattered light is captured and measured regardless of whether it is specular or diffuse, polarized or depolarized. Since the incident light is unpolarized,

we will therefore need to use the unpolarized normalized Fresnel reflectivity in the specular BRDF integral used for normalization.

The first-surface specular polarized total integrated reflectivity for normally incident light is given by:

$$R_{specular} = \int_{hemisphere} \rho'_{specular} \cdot \cos(\theta) \cdot d\Omega = \iint \frac{\rho'_{PP} + \rho'_{SS}}{2} \cdot \cos(\theta) \cdot \sin(\theta) \cdot d\theta \cdot d\phi \qquad (6.15)$$

We use the average of the two polarized BRDFs because we assume equal S and P incident light (i.e., unpolarized). We assume, of course, that the material properties are isotropic in azimuth, so the outer integral reduces to 2π. The integral becomes:

$$R_{specular} = 2\pi \cdot \int_0^{\pi/2} N_{unpolar}(\beta) \cdot \frac{bi\_factor(\theta_N)}{\cos(\theta_i = 0) \cdot \cos(\theta_r)} \cdot S_o(\theta_N, \beta) \cdot \cos(\theta) \cdot \sin(\theta) \cdot d\theta \qquad (6.16)$$

Clearly $\beta = \theta/2$, $\theta_N = \theta/2$, $\theta_i = 0$, and $\theta_r = \theta$. In code we integrate Equation 6.16 numerically with a fine angular step.

Next we integrate the diffuse unpolarized reflectivity:

$$R_{diffuse} = \int_{hemisphere} \rho'_{diffuse} \cdot \cos(\theta) \cdot d\Omega = \iint \left[R_x + 2 \cdot \frac{R_{hov}}{\cos(\theta_i) + \cos(\theta_r)} \right] \cdot \cos(\theta) \cdot d\Omega \qquad (6.17)$$

This integral is analytic:

$$R_{diffuse}(\theta_i) = \pi \cdot R_x + 4\pi \left[1 + \cos(\theta_i) \cdot \ln\left(\frac{\cos(\theta_i)}{1 + \cos(\theta_i)} \right) \right] \cdot R_{hov} \qquad (6.18)$$

When the laser is incident at $\theta_I = 0$, this simplifies to:

$$R_{diffuse}^{integrated}(0) = \pi \cdot R_x + 3.856026253 \cdot R_{hov} \qquad (6.19)$$

If the material is a dielectric, then generally we do not want to change the first-surface (polarized) hemispherical reflectivity (Equation 6.16). The depolarized diffuse contribution to the hemispherical reflectivity, then, is the difference between the total reflectivity and the (small) first-surface contribution:

$$R_{diffuse}^{new}(0) = DHR(0) - R_{specular}^{integrated}(0) \qquad (6.20)$$

Usually the first-surface specular reflectance is much less than the diffuse volumetric contribution for a dielectric. We rescale the two diffuse parameters equally to achieve the measured hemispherical reflectivity value:

$$rescale = \frac{R^{new}_{diffuse}(0)}{R^{int\,egrated}_{diffuse}(0)} \tag{6.21}$$

Thus:

$$R^{new}_x = rescale \cdot R^{old}_x \tag{6.22}$$

$$R^{new}_{hov} = rescale \cdot R^{old}_{hov} \tag{6.23}$$

When the measured hemispherical reflectivity DHR(0) is less than the first-surface integrated value alone (i.e., when the right hand-side of Equation 6.20 is negative), we rescale both the specular and the diffuse equally to meet the new DHR(0) (see below in Equation 6.24). Notice that in Equation 6.20, the diffuse reflectivity pretty much follows the total reflectivity as the wavelength changes.

If the material is a clear dielectric (i.e., not a paint or pigmented plastic), then we should rescale both the specular and the diffuse equally to meet the new DHR(0) (see below in Equation 6.24).

If the material is a metal, then we rescale both the specular and diffuse BRDFs equally. The reasoning here is that fundamentally the Fresnel reflectivity drives the energy balance. There is no independent *volumetric* reflection process. So, if the total reflectivity at a different wavelength is higher, say, then both the specular and diffuse contributions must go up proportionally, since both are controlled at the microscopic level by Fresnel effects.

We rescale by the ratio of new to old total reflectivities as:

$$rescale = \frac{DHR(0)}{R^{int\,egrated}_{specular} + R^{int\,egrated}_{diffuse}} \tag{6.24}$$

We then apply this rescaling factor first to the bi_factor we interpolated in Equation 6.7:

$$\text{bi\_factor}_{new}(\theta_N) = \text{bi\_factor}_{old}(\theta_N) \cdot rescale \tag{6.25}$$

Equation 6.25 implies that every tabulated value for the bi_factor must be rescaled. Finally, we rescale the diffuse parameters identically as they were in Equations 6.22 and 6.23 above.

Note that if we are working a problem at a single wavelength (e.g., active laser illumination) where we have measured data, then whatever method we use to rescale (and therefore renormalize the BRDF) should return exactly the measured parameters, unless the measured DHR(0) is slightly different from the extracted BRDF parameters. This is usually the case. Since the independently measured DHR(0) is inherently more accurate, because it collects all the energy from the hemisphere (and for reasons of consistency), we always renormalize the BRDF model to the DHR(0).

In terms of the MATTER.DAT material properties database, the DHR(0) comes from an interpolation of the color curves for each material. For example, a typical surface property entry in the database would appear as:

```
# ---------------
SURF 0001 Aluminum Alloy, 2024-T3, Polished
CAT Finishes
SUBCAT1 Aluminum Alloy, 2024-T3
SUBCAT2 Polished
Solar Abs 0.210
Broad Em  0.030
Surf Type 2
BRDFS
PH
MB
END
1-Refl
 0.250 0.461 0.080
 . . .
 10.600 0.030 0.007
END
REFLECTANCE
 0.20 0.3817
 . . .
 14.00 0.9700
END
END SURF
# ---------------
```

The important entries are highlighted in red. It is the surface code that uniquely identifies this material, not its name, which follows the code. The surface type is 2, which is a metal. Type 1 is a dielectric paint. Type 3 is a clear dielectric such as glass. The two columns of data between the key words REFLECTANCE and END are the radiometric hemispherical reflectivities. The first column is the wavelength in micrometers; the second column is the reflectance value (0 to 1.0). These are measured values that are not a function of the BRDF or the surface roughness state.

We always renormalize the BRDF to these values to ensure proper energy balance in our radiometric equations. The color table need not be fully populated. Intermediate values are interpolated linearly, and not fit to a spline:

$$\text{DHR } (\lambda_{desired}) = (1.0 - Q) \cdot \text{DHR } (\lambda_1) + Q \cdot \text{DHR } (\lambda_2) \qquad (6.26)$$

The BRDF parameters come from the BRDF section of the database. There are three formats for the three kinds of BRDF models. The one we are primarily interested in is the Maxwell-Beard BRDF data:

```
# ---------------
BRDF_DEF_TASAT 0001 Aluminum Alloy, 2024-T3, Polished
MODEL MaxBeard
# The following Maxwell Beard data were added to support the
multispectral study
# This was copied from Aluminum, NEFDS
# This was copied from Kapton, Aluminized, 1 Mil, Kapton side out
WL 0.6328
Ndx      0.01
Kap      0.49
RX1      8.948E-03
RX2      8.948E-03
RHOV     0.000E+00
TAU      1.000E+03
OMEGA    1.000E+03
BISTATIC
 0.00 6.350E+01
 0.10 5.870E+01
    .   .   .
 90.00 0.000E+00
END
END WL
WL 1.0600
Ndx      0.09
 .  .  .
END WL
END BRDF_DEF_TASAT
```

In blue have we highlighted the BRDF code and name, and the model type. All three format types are intermixed with sequential material code numbers. In green are the model parameters starting with the wavelength. After wavelength are the complex indices of refraction (Ndx, Kap). There are two redundant Lambertian diffuse parameters, RX1 and RX2; the second is ignored. RHOV is the non-Lambertian diffuse parameter. The last two are the shadow/masking parameters (τ, Ω). In red is the bi_factor tabular data: the first column is the bi-section angle θ_N in degrees. The second column is the bi_factor (Equation 5.7). Because the BRDF for any material might be measured at several wavelengths, each measurement set ends with the keyword END WL.

The Phong BRDF parameters follow next:

```
# ---------------
BRDF_DEF_TASAT 0002 Aluminum Alloy, 2024-T3, Mill Finish
MODEL Phong
PHONG
 0.63 5.00 0.50
 1.06 5.00 0.50
 3.39 5.00 0.50
 10.60 5.00 0.50
```

```
END
END BRDF_DEF_TASAT
# ---------------
```

Again in blue we have the material code, name, and model type keyword. In red are the BRDF parameters. The first column is the wavelength (in micrometers). The second column is the cosine exponent. Valid exponent values range from zero to large positive values. A zero means the BRDF is strictly diffuse and depolarized. The third column is the Lambertian fraction for first-surface scatter. Values at wavelengths between those tabulated are linearly interpolated.

Relative to the MB BRDF data sets, there are missing or unknown parameters. First, there are no complex indices of refraction. The code defaults these according to the type of surface material. If it is paint, then the real index n is set to 1.5, and κ to 0.0. These are very typical and useful values that give a first-surface reflectance of 4%. If it is a metal, then the real index is set to 1.5, the normal incidence reflectance is assumed the same as the surface reflectance, and the code solves for κ using Equation 3.15. The Phong model does not model shadow/masking effects, so these parameters are not necessary.

Because the Phong model also does not have diffuse parameters like the MB BRDF data set, we have to normalize the BRDF a little differently. First we need to construct and then normalize the bi_factor. The tilt distribution function is:

$$\Xi(\theta_N) = \cos^N(\theta_N) \tag{6.27}$$

Then we assume that the first-surface reflectivity R_o is that of a dielectric (which we default to 4%). The rescale factor is 1 minus the Lambertian fraction times the default reflectance:

$$rescale = \frac{(1-L)\cdot R_o}{\int \Xi(\theta_N)\cdot \cos(\theta)\cdot d\Omega} \tag{6.28}$$

We then apply this rescaling factor to the bi_factor:

$$bi\_factor_{new}(\theta_N) = rescale \cdot \Xi(\theta_N) \tag{6.29}$$

Then a diffuse R_x term is constructed:

$$R_x = \frac{L\cdot R_o}{\pi} \tag{6.30}$$

Next we take into account the material type. We use the same normalization procedures as those above in Equations 6.15 through 6.25. If the material is a paint, then we already have approximately the correct first-surface normalization for the specular component. The volumetric diffuse term R_x is rescaled to provide the overall reflectivity according to Equations 6.20 through 6.22. If the material is a metal, then both the bi_factor and R_x are equally rescaled according to Equations 6.22 through 6.25.

The Gaussian BRDF parameters follow next:

```
# ----------------
BRDF_USER_DEF 9001 Shiney Surface (1 deg. specular lobe)
MODEL Gaussian
GAUSS
0.63 0.0175 0.0 1.5 0.0 0.0
1.06 0.0175 0.0 1.5 0.0 0.0
3.39 0.0175 0.0 1.5 0.0 0.0
10.6 0.0175 0.0 1.5 0.0 0.0
END
END BRDF_USER_DEF
# ----------------
```

Again in blue we have the material code, name, and model type keyword. In red are the BRDF parameters. The first column is the wavelength (in micrometers). The second column is the Gaussian specular lobe angular size (sigma for the e^{-2} point). Valid sigma values range from 1.745×10^{-3} radians (0.1 degrees) to large positive values. Smaller sigma values are considered unphysical, and lead to a defaulted totally diffuse BRDF. The third column is the Lambertian fraction for first-surface scatter. The fourth column is the real index n. The fifth column is the complex index κ. The last column is not used. Values at wavelengths between those tabulated are linearly interpolated.

The unknown parameters are for the shadow/masking. But this model also does not model shadow/masking. Since the complex indices are specified, they are used in the same way as for the MB BRDF. However, we do need to normalize the specular bi_factor the same way we did for the Phong model in Equations 6.27 through 6.30.
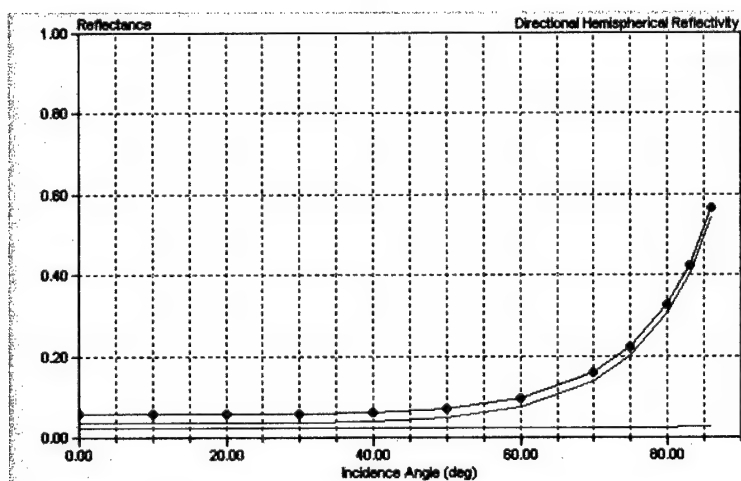

Figure 6.1. Integrated Hemispherical Reflectance for Black Chemglaze

At normal incidence, our synthesized BRDF must have an integrated reflectivity equal to the interpolated color value assigned to this surface material. What about angle-of-incidence effects? The DHR is only quoted for normal incidence, and never quoted for other angles. How does the DHR of our modeled materials behave? This is an important topic. Figure 6.1 shows a plot of the integrated hemispherical reflectivity as a function of the incident laser angle. The green curve is the diffuse component, the red is the specular, and the blue is the total. Notice that the turn-up at larger angles is driven entirely by the specular component. Figure 6.2 plots the
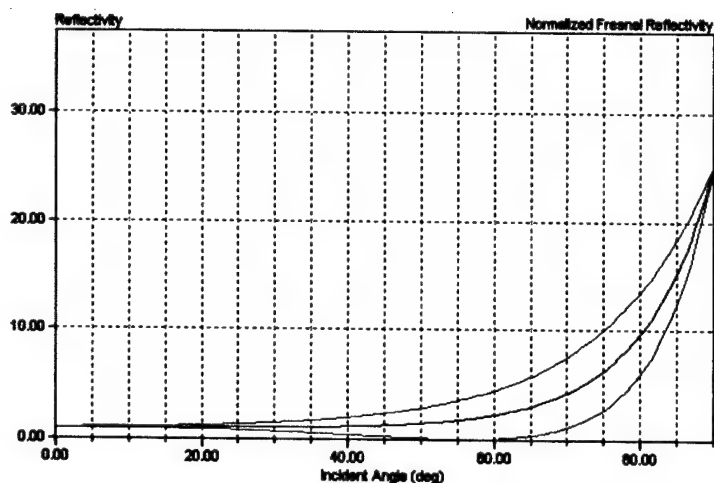
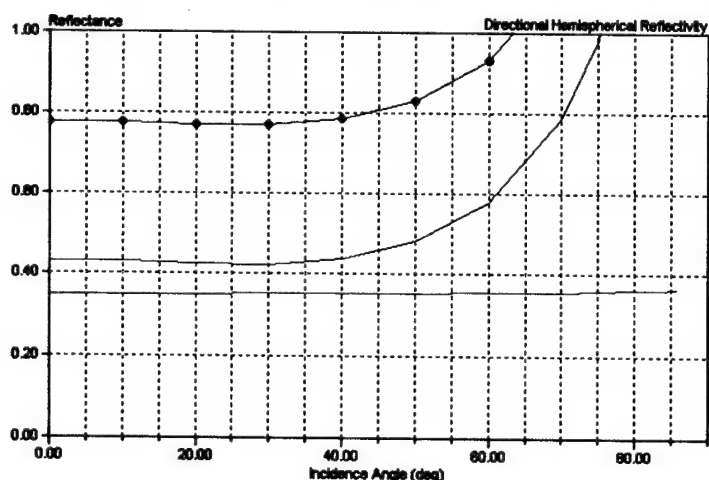**Figure 6.2. Companion Normalized Fresnel Curves for Black Chemglaz**

Figure 6.3. Integrated Hemispherical Reflectance for the Aluminum Alloy

normalized Fresnel curve for this material. Notice that it too turns up at the same angles, and grows by a factor of about 15 at 86 degrees, which is how much the specular reflectivity grows. The assigned complex indices are ($n = 1.5$, $\kappa = 0$), which are reasonable for a dielectric paint.

However, consider material 0048, Aluminum Alloy, 5456-H116, Clear Anodized. This is a metal where the indices are ($n = 1.52$, $\kappa = 0.55$), which are frankly unreasonable. The normal incidence reflectance is about 9% for these values, whereas the material is about 77% reflective at 1μm wavelength. Clearly these indices were fitted against some data. The problem comes with the DHR at the larger angles. Figure 6.3 shows the integrated hemispherical reflectivity. Notice that it goes above a reflectivity of 1 at 63 degrees. This is clearly unphysical. The final reflectivity is over 3.

Because of the choice of indices, the reflectance *should* climb by more than 10 at grazing incidence, which in turn drives the specular reflectivity to over 1! This is the fallacy in choosing just any index pair that seems to fit measured directional intensity data. Errors in the measurements lead to bogus indices, which in turn model unphysical total reflectivities. This is why we propose choosing the indices by first matching the normal incidence reflectivity and then the apparent Brewster angle.

Another subtle problem with these reflectivity curves is in the diffuse component for paint (Figure 6.1) and for metal (Figure 6-3). They are both constant in angle. This might be reasonable for metal, but not for paint. When the first-surface Fresnel reflection begins to dominate, less energy can penetrate into the volumetric region to rescatter into large diffuse angles. This means that the diffuse component should go down at the larger angles. This is a minor problem that is rooted in the basic MB BRDF model.

7.0 Estimating the Angular Width of the Specular Lobe

Knowing the specular BRDF lobe angular width is important for certain rendering and radiometric operations. In LRST, for example, we paint the BRDF for a flat plate onto the Golden Sphere, pixel by pixel. The code needs to have an estimate of the size of the BRDF in order to know when to stop painting insignificant pixels that are at angles too far away from the specular direction. There are two useful methods that, oddly enough, give different answers. The first is to find the angle at which the specular BRDF drops to some fraction of its peak on-axis value. This is the obvious method, but it is insensitive to the particular shape of the BRDF. The second technique builds a radial energy distribution (RED) and sets a threshold at a certain fraction of the integrated power. This would be a more useful measure for LRST because it will guarantee that, within a given angular radius, that fraction of the total specular energy has been painted, and therefore accounted for. Since diffuse energy is accounted for separately, it is not part of the determination for the lobe width.

The intensity threshold searches for the angle at which the intensity drops below a percent of peak BRDF threshold:

$$\vartheta_{lobe} = \left\{ \rho'\left(\vartheta\right) \right\} < \text{threshold} * \rho'_{peak} \tag{7.1}$$

We start the search for the percent-integrated energy by creating the radial energy distribution RED(θ):

$$\text{RED}(\theta) = \frac{2\pi}{\text{DHR}} \cdot \int_0^\vartheta \rho'\left(\theta\right) \cdot \cos(\theta) \cdot \sin(\theta) \cdot d\theta \tag{7.2}$$

which is a relative running normalization integral. When the RED exceeds the desired percent captured energy, that angle is used:

$$\vartheta_{lobe} = \left\{ RED(\vartheta) > threshold \right\} \tag{7.3}$$

Figure 7.1 shows a RED for a moderately shiny material. The 50% power occurs at about 9.5 degrees (radius), whereas the 50% intensity threshold occurs at about 9.7 degrees.
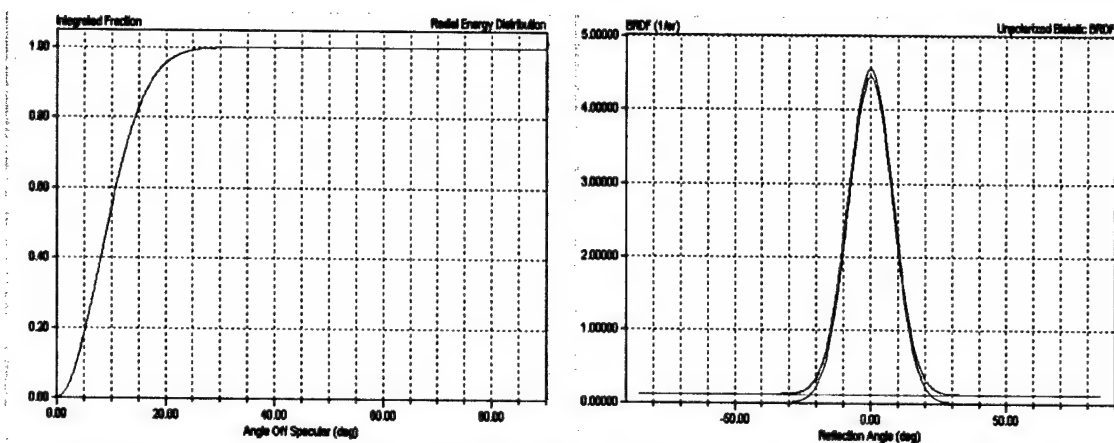
Figure 7.1. Left: Radial Energy Distribution for a Shiny Metal; Right: BRDF

While Figure 7.1 shows the kind of behavior one would expect, this is not always the behavior one sees for some BRDFs. For example, consider the very shiny metal in Figure 7.2. The intensity width is determined to be about 0.7 degrees, but the RED angular width is about 11.3 degrees! The BRDF shape is apparently very important to consider if we want to make sure we capture the majority of the scattered energy.
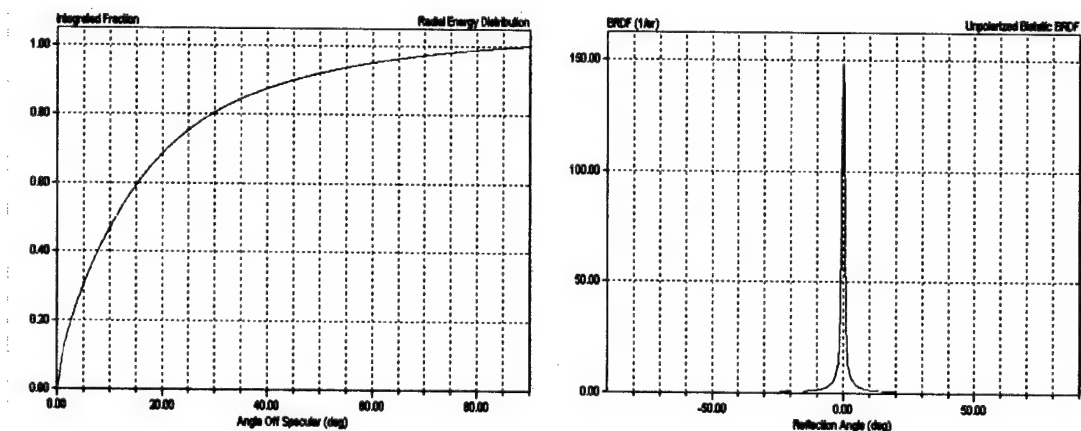

Figure 7.2. RED and BRDF for Very Shiny Metal

8.0   Using the BRDF

The usual objective of radiometric signature calculations is to predict the amount of power entering a receiver aperture, having scattered off a target body. The equations are rather simple, and they all stem from rearranging Equation 2.1. The equations that follow relate to small incremental surface areas that are flat and uniform. Sometimes when large areas are relatively flat, the smallness restriction can be lifted. We will also be interested in the definition and usage of the optical cross-section (defined differently from radar cross-section).

The lowest denominator in Equation 2.1 is defined as the incident irradiance. Consider a collimated beam with irradiance I_o (Watts/m^2) that is incident on a flat surface element δA (m) at an angle θ_i. The total power intercepted by the surface element is:

$$\delta P_i = I_o \cdot \delta A \cdot \cos(\theta_i) \qquad \text{(Watts)} \qquad (8.1)$$

The denominator can be better expressed by:

$$\delta P_i / \delta A = I_o \cdot \cos(\theta_i) \qquad \text{(Watts/m}^2\text{)} \qquad (8.2)$$

We now solve Equation 2.1 for the power collected by the receiving aperture δP_r:

$$\delta P_r = I_o \cdot \cos(\theta_i) \cdot \rho' \cdot \delta A \cdot \cos(\theta_r) \cdot \delta \Omega_{rec} \qquad \text{(Watts)} \qquad (8.3)$$

We recognize the rightmost three terms as an Etendue' - the configuration factor:

$$\delta \xi = \delta A \cdot \cos(\theta_r) \cdot \delta \Omega_{rec} \qquad \text{(m}^2\text{-sr)} \qquad (8.4)$$

where the receiver aperture solid angle is:

$$\delta \Omega_{rec} = \frac{\delta A_{aperture} \cdot \cos(\theta_{LOS})}{Z^2} \qquad \text{(sr)} \qquad (8.5)$$

and $\delta A_{aperture}$ is the aperture collecting area, θ_{LOS} is the angle between the aperture pointing line of sight (LOS) and the line to the target (θ_{LOS} is always assumed zero), and Z is the range to the target. We can also introduce the concept of radiance, $J = I_o \cdot \cos(\theta_l) \cdot \rho'$ (Watts/m^2-sr) and express the received power very compactly as:

$$\delta P_r = J \cdot \delta \xi \qquad \text{(W)} \qquad (8.6)$$

Since the BRDF is directionally dependent, we sometimes refer to J as the directional radiance. Equations 8.3 or 8.6 are the fundamental radiometric relations we need to make radiometric predictions. Because targets are so complex, we must code these equations and use ray-tracing techniques to sample the target shapes, and must do the target geometry incrementally.

We need to define another important radiometric quantity, the optical cross-section χ, as the ratio:

$$\chi = \frac{\delta P_{rec}}{I_o \cdot \delta \Omega_{rec}} = \rho' (\theta_i, \theta_r, \phi_r) \cdot \delta A \cdot \cos(\theta_i) \cdot \cos(\theta_r) \qquad \text{(m}^2\text{/sr)} \qquad (8.7)$$

where we have rearranged Equation 8.3 to separate the target-specific attributes. The cross-section is strictly a function of the target shape, its material properties, the illumination geometry, and the viewing geometry, and nothing else. Figure 3.1 shows the basic geometry assumed for Equation 8.7.

For complex target scattering geometries, in practice we can calculate the total cross-section by integrating (summing) over many small differential surface area elements:

$$\chi = \frac{\sum \delta P_r}{I_o \cdot \Omega_{rec}} = \sum \rho' \cdot \delta A \cdot \cos(\theta_i) \cdot \cos(\theta_r) \qquad (\text{m}^2/\text{sr}) \qquad (8.8)$$

or, put into integral form:

$$\chi = \int \rho' \cdot \cos(\theta_i) \cdot \cos(\theta_r) \cdot dA \qquad (\text{m}^2/\text{sr}) \qquad (8.9)$$

When the irradiance is not uniform over the entire target, then the measured or apparent cross-section will become a function of the irradiance profile. In this case we would need to include the unit-irradiance beam profile into the calculation of the incremental cross-section contributions.

If we know the cross-section, we can always invert Equation 8.7 to predict the power at the receiver:

$$\delta P_{rec} = \chi \cdot I_o \cdot \delta \Omega_{rec} \qquad (\text{Watts}) \qquad (8.10)$$

where I_o now represents the peak on-axis irradiance. The scattered intensity at the receiver aperture is:

$$I_{rec} = \frac{\delta P_{rec}}{\delta A_{rec}} = \chi \cdot \frac{I_o}{Z^2} = \rho' \left(\theta_i, \theta_r, \phi_r\right) \cdot \delta A \cdot \cos\left(\theta_i\right) \cdot \cos\left(\theta_r\right) \cdot \frac{I_o}{Z^2} \quad (\text{Watts}) \qquad (8.11)$$

In Figure 8.1 we render a typical BRDF and scattered intensity in 3D as an iso-intensity surface. Notice the spread of the BRDF near the plane of the material. This is the usual turn-up of the BRDF at grazing angles where the denominator of the specular BRDF explodes because of the $\cos(\theta_r)$ term. On the right we rendered the intensity profile. The cosine in the numerator now cancels this turn-up, as expected.
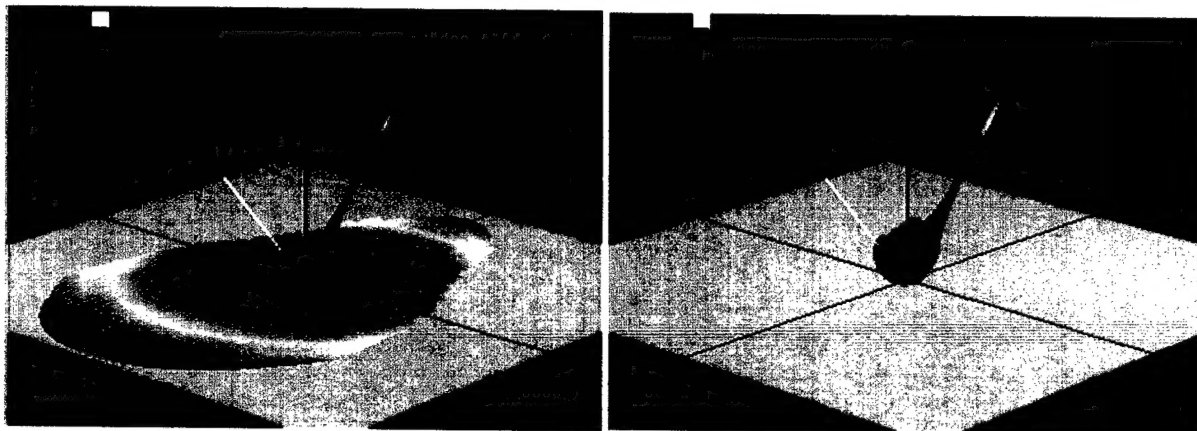

Figure 8.1. Rendered 3D BRDF; the image on the left is the BRDF; the yellow box is the laser Source; the image on the right is the cross-section (intensity)

The lower intensity (blue) colors are due to the diffuse BRDF contribution. The yellow and red colors show the specular BRDF contribution. Figure 8.2 shows the same BRDF but with the functional values displayed on a hemispheric dome.
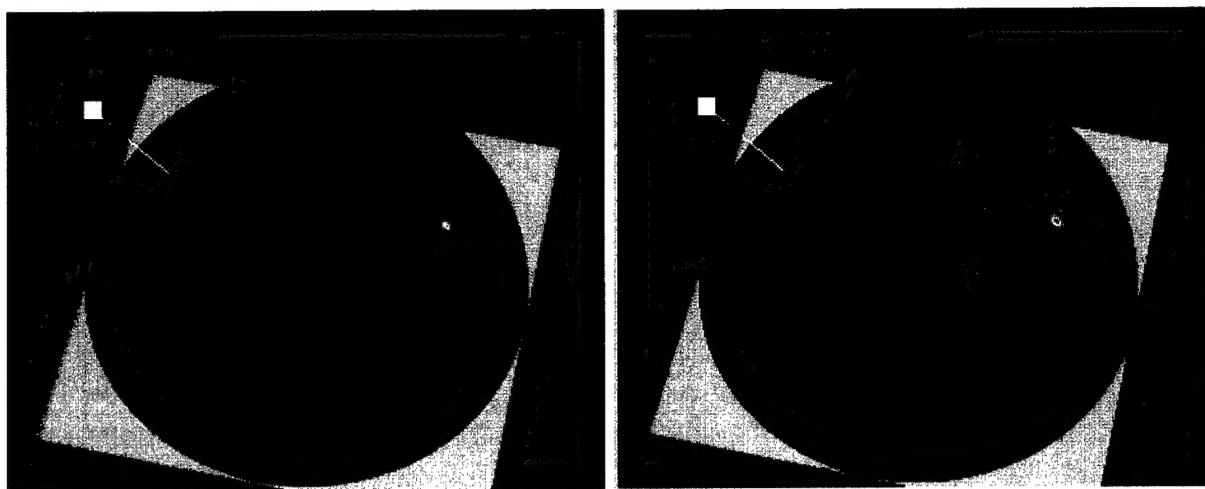

Figure 8.2. Same BRDF and Cross-sections Displayed on a Hemisphere

One of the interesting effects of scattering at grazing incidence is how the BRDF will become narrower along the cross-plane direction. The narrowing of the BRDF is caused by the rapid increase in the bi-section angle (θ_N) motion due to the optical gain $\delta\theta_N = \dfrac{\delta\theta_{LOS}}{2 \cdot \cos(\beta)}$. Since β is near 90 degrees, the change in the bi-section angle is large for even small observer motions cross-plane. At the same time the BRDF is getting narrower, there is a cosine in the specular BRDF denominator that is also increasing its magnitude. The combined effect when integrating the total power is to keep it constant.
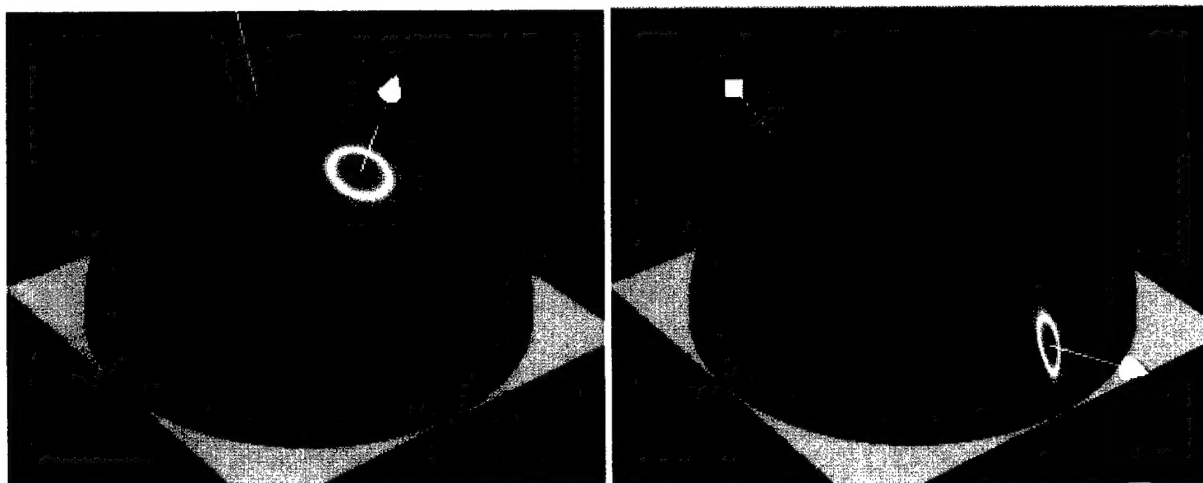

Figure 8.3. Typical BRDF at Near Normal Incidence on Left, and Grazing at Right

Figure 8.4 shows calculated BRDF slices at 75-degree incidence. The red curve is the in-plane BRDF, and the green curve is the cross-plane scan (a scan perpendicular to the in-plane scan).

Figure 8.5 demonstrates the growth of the BRDF with increasing angle of incidence. In this case, the normalized Fresnel curves do not change very much, so the growth is caused primarily by the cosine in the denominator.
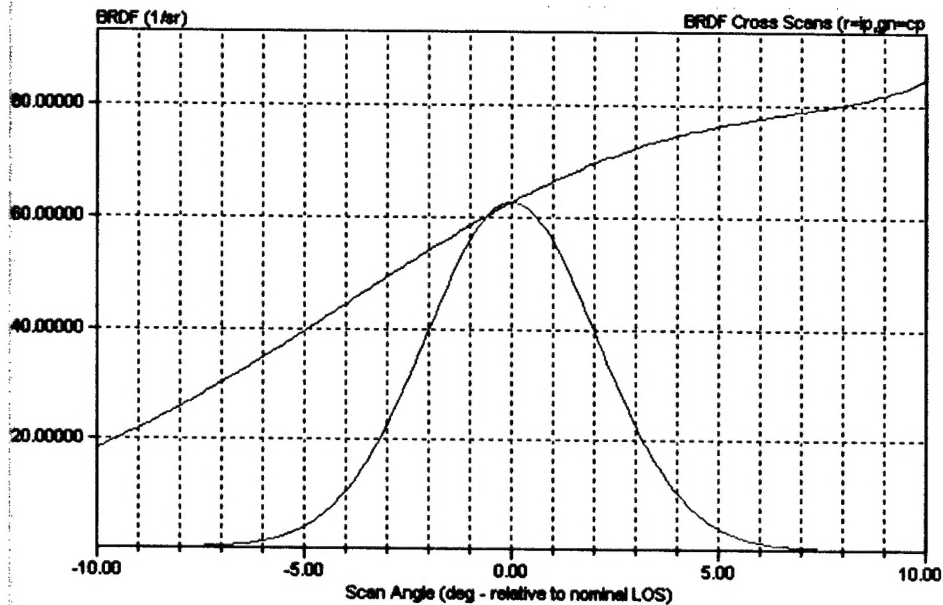

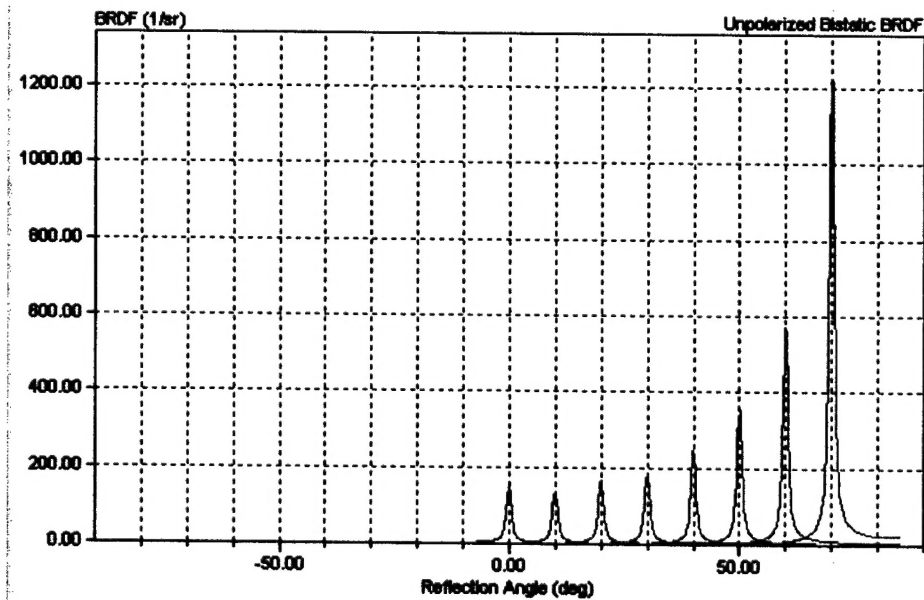***Figure 8.4. In-plane BRDF (Red) and Cross-plane BRDF (Green) at 75-Degree Incidence***

Figure 8.5. Growth of the BRDF Peak with Increasing Angle of Incidence

9 References

1. F. E. Nicodemus, J. C. Richmond, J. J. Hsia, I. W. Ginsberg, and T. Limperis, *Geometrical Considerations and Nomenclature for Reflectance*, NBS Monograph 160, U.S. Government Printing Office, October 1977.

2. J. R. Maxwell, J. Beard, et al, *Bidirectional Reflectance Model Validation and Utilization*, ERIM Technical Report AFAL-TR-73-303, October 1973.

3. B. T. Phong, "Illumination for Computer-Generated Pictures," *Comm. ACM*, 18(6), 1975.

4. K. E. Torrance and E. M. Sparrow, "Theory for Off-Specular Reflection from Roughened Surfaces," *J. Opt. Soc. Amer.*, Vol. 57, No. 9.

5. *Non-conventional Exploitation Factors (NEF) Modeling*, ORD-257-96, 22 August 1996.

6. G. Crockett, "The Derivation of Analytic Optical Cross-Sections for a Sphere, Cylinder, Cone, and a Flat Plate," Contract F29601-95-C-0197, CDRL A005.

7. H. B. Holl, "Specular Reflection and Characteristics of Reflected Light," *J. Opt. Soc. Amer.*, May 1967, Volume 57, No. 5, p. 683.